National Technical University of Athens
School of Mechanical Engineering
Lab. of Thermal Turbomachines
Parallel CFD & Optimization Unit

NASA Rotor 37 Endwall Profiling Using the GPU-Enabled CFD Solver PUMA

Diploma Thesis

Konstantinos Kotsarinis

Supervisor: Kyriakos C. Giannakoglou, Professor NTUA
Industrial Supervisor: Anastasios P. Kovanis, Aerodynamicist RR

September 2021, Athens

National Technical University of Athens
School of Mechanical Engineering
Lab. of Thermal Turbomachines
Parallel CFD & Optimization Unit

NASA Rotor 37 Endwall Contouring Using the GPU-Enabled CFD Solver PUMA

Diploma Thesis

Konstantinos Kotsarinis

Supervisor: Kyriakos C. Giannakoglou, Professor NTUA

Industrial Supervisor: Anastasios P. Kovanis, Aerodynamicist RR

Athens, 2021

Abstract

In this diploma thesis, turbomachinery endwall shape design methods are applied in the open case of NASA Rotor 37, aiming to a performance and operability benefit. The purpose of this diploma thesis is to present solutions of the endwall shape produced by a manual iterative design process, after cross validating results computed by the PUMA CFD flow solver, developed by PCOpt/NTUA, against computational results and experimental data available from NASA literature.

For compressors, the endwall regions are associated with losses, being critical regions of low momentum fluid, that lead to operational restrictions. Endwall contouring was used in order to control the overturned boundary layer of the highly loaded compressor blade, reduce the flow separation which is generated in the flow at the root of the blade and mitigate the total pressure losses over the design speed. Specifically, the endwall surfaces were perturbed near the region of the blade to create convex and concave shapes with the use of B-Splines. The endwall contours were investigated for the hub and the casing of the rotor and provided satisfying improvements to both the performance and the operability of the NASA Rotor 37 case.

For the design of the endwall geometries and the discretisation of the domain, the CFD mesh generation tool PADRAM (Parametric Design and Rapid Meshing – developed by Rolls-Royce plc.) was used to mesh the different geometries of NASA Rotor 37, while the the GPU-enabled CFD flow solver PUMA was used for simulating the flow in the rotor blade row. A part of the work was carried out at the Rolls-Royce Plc premises in Derby.

Abbreviations

NTUA	National Technical University of Athens
PCopt	Parallel CFD & Optimization Unit
CFD	Computational Fluid Dynamics
ODE	Ordinary Differential Equations
PDE	Partial Differential Equations
RANS	Reynolds Averaged Navier-Stokes
PADRAM	Parametric Design and Rapid Meshing
LP	Low Pressure
LPC	Low Pressure Compressor
HP	High Pressure
HPC	High Pressure Compressor

Contents

Chapter 1

Introduction

1.1 Thermal Turbomachines

Aircraft propulsion was radically changed since the introduction of the air breathing jet engine in the 30's with the parallel ideas of English and German pioneers Frank Whittle and Hans von Ohain to build a reaction engine of very high power to mass ratio combining a gas turbine with a nozzle. Since then, significant improvements have been made to arrive to modern aircraft engines,such as the introduction of the double-flow turbofan concept, but a truly new technological breakdown is still future. Some of the irreplaceable features of the jet engines are their capability to deliver large amounts of thrust compared to their mass flowrates, to be compact and reliable and to guarantee the aircraft propulsion in a wide range of different operating conditions.

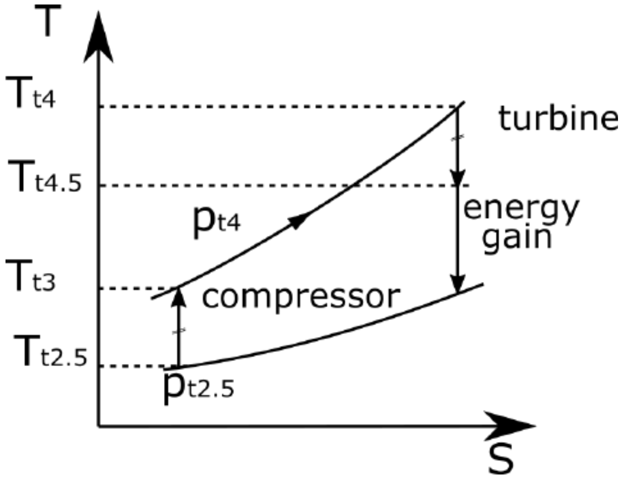

Figure 1.1: *Gas turbine Brayton cycle [1].*

In order to generate the required thrust for the propulsion of aircraft, energy has to be provided to the working fluid at first, which is subsequently exploited following the thermodynamic cycle of Brayton, shown in Figure 1.1. The energy surplus is provided by the ignition at constant pressure of air-fuel mix in the combustion chamber. The pressure rise of the breathed air is needed to increase the efficiency of the cycle, so a compressor module is installed before the combustion chamber and a turbine is placed after the combustion chamber to extract from the exhaust gas the energy necessary to power the compressor. The remaining energy of the fluid is then converted into thrust by acceleration and ejection from a nozzle, or the energy is again transformed in shaft power by a second turbine to accelerate the fluid with a propeller or fan. The modern turbofan design integrate both concepts, generating roughly 20% of the thrust by the accelerating the fluid in the core nozzle and the other 80% in the external duct, provided also of a nozzle, by the front fan. A typical layout of the systems of a turbofan engine, a type of engine widely used for civil aircraft propulsion, is shown in 1.2.

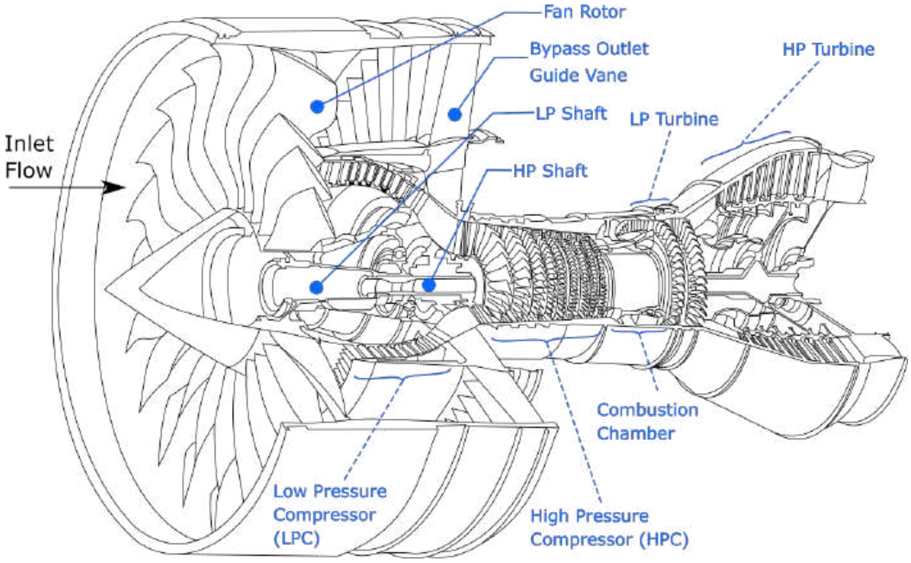

Figure 1.2: *Schematic diagram of the compression system for various types of jet engines [1]*

1.2 Axial Flow Compressors

Axial compressors are essential parts of the turbomachinery of many gas turbine engines. However, their design can impose particularly difficult challenges, which may not only result in low efficiency but also stall and surge that may render an engine inoperable. The alternative is the centrifugal compressor that can produce large pressure rise in a single stage due to the use of centrifugal effect. When the frontal area is important, the axial flow compressor provides advantages, as is the case for a jet engine where drag needs to be kept down. Unfortunately, these advantages are gained at the expense of the need to decelerate the flow through multiple rows of blades. Application of axial flow compressors can be found also in industrial gas turbines where the large flow rates would require very large diameter centrifugal compressors.

Every element of the compressor system, fan (low-pressure), booster, intermediate pressure and high pressure compressors provide their own design challenges. At the rear of high pressure compressors Mach numbers are rarely above unity and the annulus wall flows are crucial. This chapter will focus on the issues more associated with intermediate and high pressure compressors. The fundamental aerodynamic problem is that the air is travelling uphill against the pressure gradient, which can lead to reverse flows. In such an occurrence, the engine loses thrust and ceases to operate as required until the control system can recover the situation at a less arduous operating condition. In severe cases, mechanical damage can be sustained that may put the engine out of operation completely.

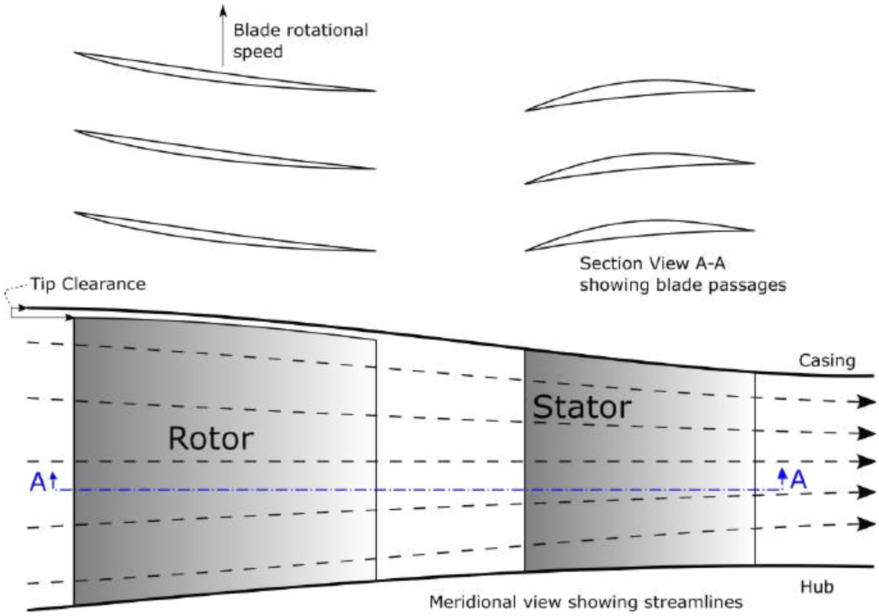

Figure 1.3: *Schematic view of a compressor stage [2]*

The generic geometry of an axial compressor stage is established in Figure 1.3. A schematic representation of a compressor stage is depicted, comprising a row of rotor blades followed by a row of stator blades. Each blade row consists of a series of aerofoil sections along the streamlines that are turning the flow towards the axial direction and, hence, are diffusing passages. A multistage compressor consists of a series of stages placed one behind the other. This representation of the flow assumes a simplification in that the streamlines have been drawn on the meridional view, which implies that the air flows along these in an axisymmetric fashion.This will be useful as a notation for later, but is a far from accurate description of the flowfield.

A typical stage characteristic is plotted in Fig. 1.4. In the bottom part of the figure the stage pressure rise is plotted against the axial velocity. In the ideal case the linear variation of stage work with velocity would result in the straight line on the graph. Towards the top of the characteristic the blade exit air angles tend to increase, so here the stage pressure rise is reduced below the ideal level. In addition the efficiency of the stage varies as shown in the top part of the figure which means that the pressure rise tends to be less than expected at flows other than the datum flow.

Once the characteristics have been calculated for every stage they can be combined together to give the predicted overall characteristics of the whole compressor. Such a map can be obtained from a rig test of a compressor and is shown in Figure 1.5. The performance is represented by the overall pressure ratio and efficiency is plotted against the inlet flow. These characteristics are plotted at a range of rotational speeds for the compressor. As the inlet flow is reduced at some point on the characteristic the flow in the compressor becomes unstable, experiencing surge or stall [2].

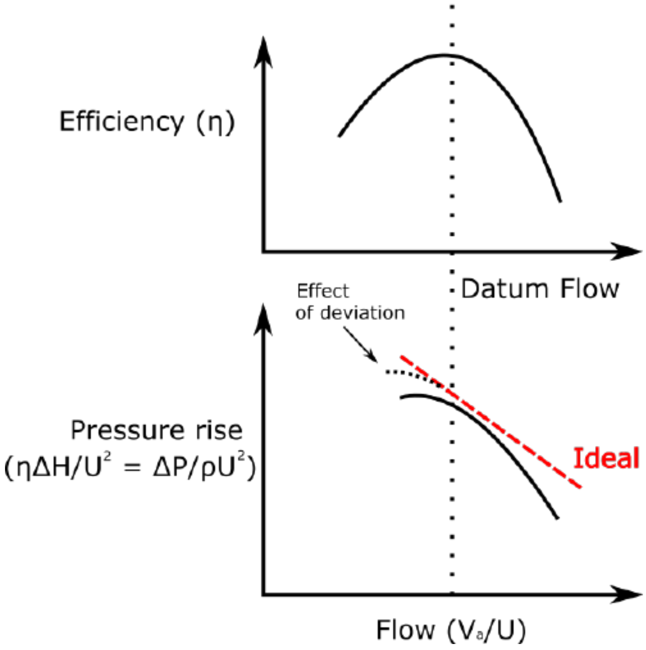

Figure 1.4: *Stage characteristics [2]*

It is not possible to operate the compressor beyond the surge or stall line that determines the limits of stability for the characteristics at each iso-speed line. Efficiency also increases with reduced flow at each speed until a peak is reached and after that it reduces as the pressure ratio increases further. Some additional information, that represents the steady state operating points of the compressor in the engine, is plotted on the pressure ratio/flow characteristics. These are the working lines, one at high speed and one at lower speed which shows the effect of taking bleed. The gap between the surge and working lines represents the surge margin, which is required to allow the compressor to operate successfully in the engine.

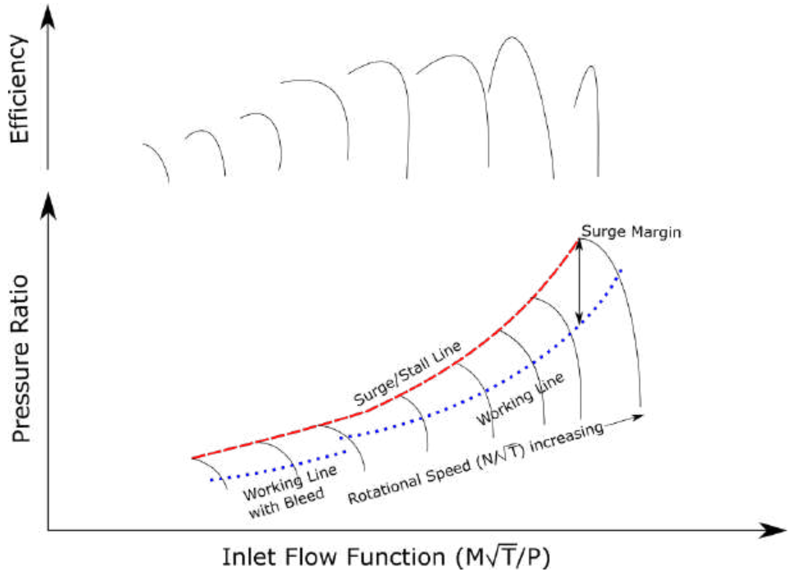

Figure 1.5: *Typical overall multi-stage compressors characteristics* [2]

The process of aerodynamic design of an axial flow compressor is very complex and includes interactions with several different disciplines. Initially the targets of flow, efficiency and pressure ratio are set in way such that the overall engine performance will meet its goals. The dimensions of the compressor need to be established to meet weight and cost targets, while the shaft speed needs to be aligned with turbine requirements. Mechanical design and stress considerations need to be included. This chapter focuses on the aerodynamic aspects of the compressor but it is important to recognise that the design process in interactive and iterative throughout.

These interactions will not be covered in detail but it must not be forgotten that they can exert influence on the design, with crucial areas being mechanical integrity, including blade vibration and flutter. The tolerance of the compressor to water ingestion, icing and bird strikes also needs to be included in design decisions.

1.3 Transonic Compressor Aerodynamics

The fundamental purpose of the compressor is to employ shaft work in order to increase the total or stagnation pressure of the working fluid. This is achieved by creating high relative velocities at entry to the blade row and subsequently diffusing (decelerating) the flow in the blade passage to recover its relative kinetic energy. This energy in turn leads to increases in total temperature and total pressure of the air departing from the rotor. Accompanying this process, are increases in static pressure and absolute whirl of the air. A part or all of the rotation imparted to the flow is then removed in the following stator with a further recovery of static pressure, while simultaneously setting up the flow for the next rotor. As the air travels consecutively through rotors and stators, it is compressed and its density is increased. The annulus area is gradually decreased to correspond with the decreasing volume in order to maintain an acceptable axial throughflow velocity.

The design requirements of a compressor in general include high efficiency, high air flow capacity per unit frontal area and high pressure ratio per stage. Because of operational requirements, high levels of performance must be ensured over a series of speed and flows without any instability. The flow field that develops inside a transonic compressor rotor is extremely complex and presents many challenges to the compressor designers who have to deal with several and concurring flow features such as shock waves, shock/boundary layer interaction, intense secondary flows, etc. including energy losses and efficiency reduction. [3]

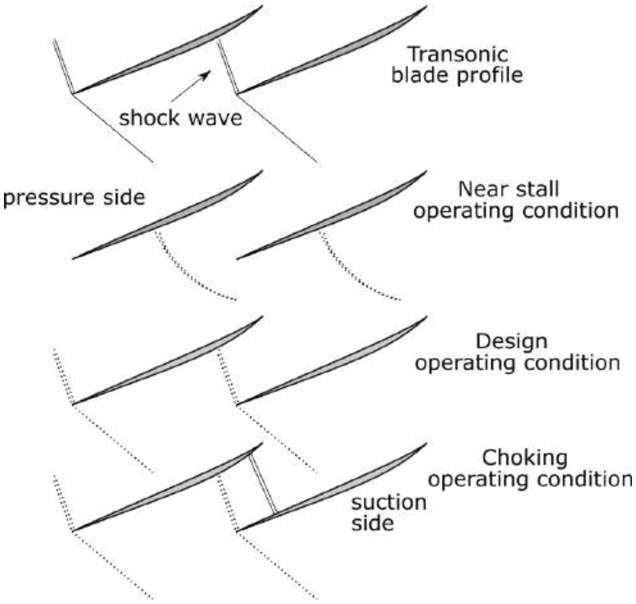

Figure 1.6: *Shock wave configuration inside a transonic compressor rotor (a) Shock configuration-sketch and (b) Impact of operating condition [4].*

Figure 1.6 (a) shows a schematic blade-to-blade shock configuration that can be found in a transonic compressors rotor in consequence of the deflection imposed by the blade pressure side wall to the relative flow. The shock starts from the blade leading edge and propagates into the blade passage. Depending on rotor geometry and operating condition, the shock can develop in different ways. It can be more or less inclined to the incoming flow, while it can also bifurcate. Further shock waves can also develop downstream inside the blade passage. Figure 1.6 (b) shows the shock configuration inside a generic transonic compressor rotor, moving from the chocking condition to the near stall condition and maintaining a constant wheel speed. Generally, the shock shifts upstream and becomes normal to the incoming flow as the operating point moves towards lower mass flow operating conditions, as a consequence of the higher flow incidence due to the lower mass flow rate.

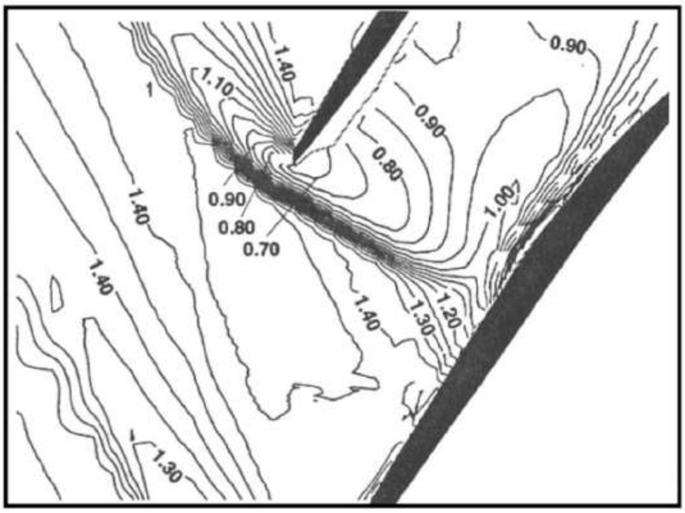

Figure 1.7: *Measured blade-to-blade relative Mach number in a transonic compressor rotor [5].*

At the outer half span region, the shock impacts strongly on the blade suction side and interacts negatively with the local boundary layer. Due to the adverse pressure gradient across the shock, a significant increment of boundary layer thickness is induced (Figure 1.7) and a separation bubble can occur. In case of separation, the boundary layer may reattach before the trailing edge or not. If not, larger and deeper blade wakes develop, leading to a considerable increment of aerodynamic losses. A strong outward radial fluid migration is also observed inside the suction side boundary layer after the interaction with the shock. This characteristic flow phenomenon is sketched in Figure 1.8. It induces an accumulation of low momentum fluid at the outer span region which is considered to be detrimental for rotor stability, and causes a boundary layer thickening with a further negative impact on blade wake development. [4]

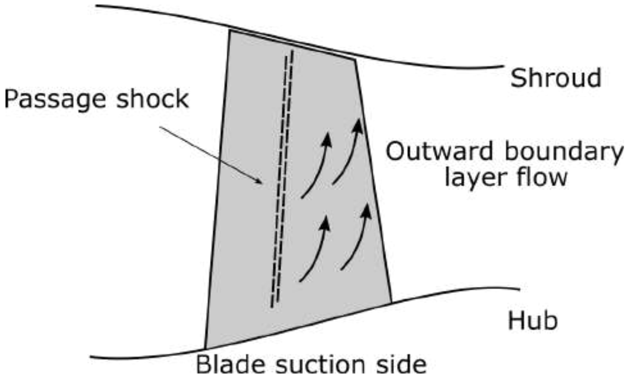

Figure 1.8: *Blade suction side boundary layer radial fluid flow [4].*

Shock waves result in many other negative flow phenomena, such as blockage, corner stall separation, upstream wakes destabilization etc. Particularly detrimental is the interaction with the tip clearance flow at the outer span of the rotor, where the compressor generally shows the higher entropy production. At blade ends with a wall clearance (rotors at the outer casing and cantilevered stators at the hub) the flow is heavily influenced by the flow across the clearance region. The main causes of this flow are the viscous drag of the endwall passing over the blade tip and also the pressure difference across the blade. The tip leakage flow interacts with the flow already on the endwall to create a complicated flow pattern that is often characterised by a vortical structure as the tip clearance flow rolls up and passes downstream (Figure 1.9). This a vortex is known as "tip clearance vortex" or "tip leakage vortex" which generally starts at the leading edge and develops into the passage. The complex flow structures arising from the interaction between the vortex, the casing boundary layer and the passage shock have detrimental effects on the overall rotor performance. As the compressor moves from peak to near stall operating points, the blade loading increases and flow structures become stronger and unsteady. The tip leakage vortex can breakdown interacting with the passage shock wave, leading to not only a large blockage effect near the tip but also a self-sustained flow oscillation in the rotor passage. [4]

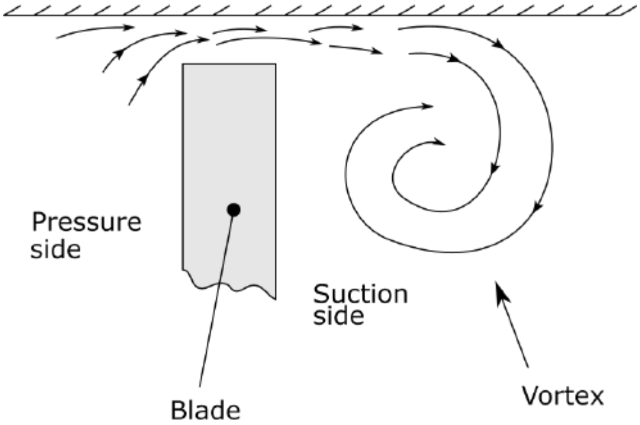

Figure 1.9: *Schematic representation of tip clearance flow [6].*

Figure 1.10 summarises the main types of flow that are usually found in a multistage compressor rotor blade row as previously mentioned, when transient effects are not taken into account. In practice, due to the relative motion between successive blade rows, the flow is unsteady. The wakes of the upstream blade will pass periodically through the downstream row and the alternating back pressure from the downstream blade row will alter the flow in the row upstream. The wakes from blade rows even further upstream also persist through the compressor and can be detected in the blade under consideration.

Moreover, the flow into the blade passage is varying radially and can be considered to be divided in two regions, one as a freestream region and one including the endwall boundary layers where the flow velocities vary towards the endwall values. Due to the difference in rotation between successive blade rows, decreases in axial velocity near region of the annulus walls impose a change of inlet angle in the frame of reference of the blade row under consideration. Generally the relative air inlet angles increase towards the walls. The freestream is turned toward the axial direction and diffused through the blade row. This sets up a tangential pressure gradient which then acts on the endwall boundary layer fluid. This fluid is subject to the effect of shear on the endwalls and at the same time has a deficit in momentum at inlet to the blade. This leads to different turning than the freestream flow in the pressure gradient resulting in flow under or over turning and radially non-uniform exit flow angles from the blade row. [3]

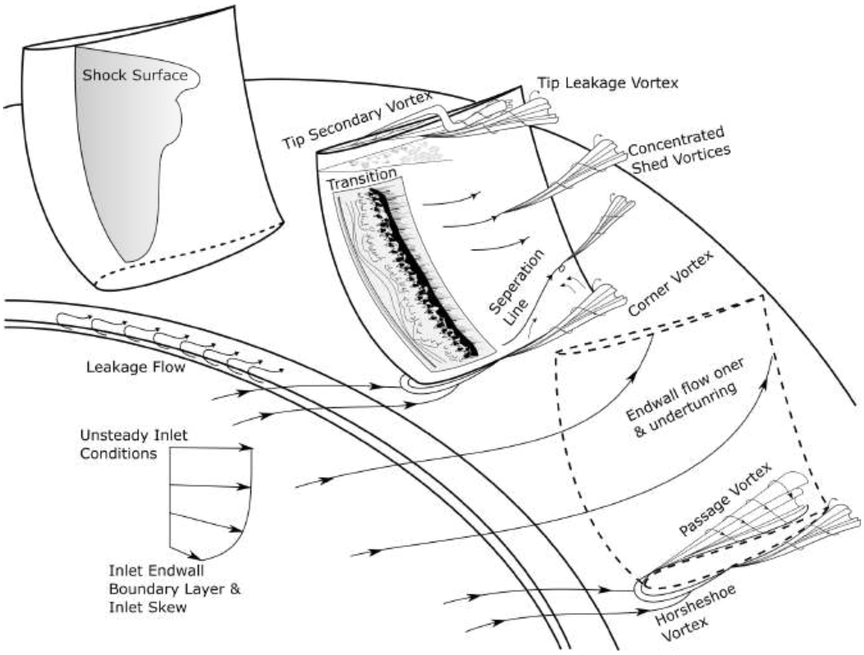

Figure 1.10: *Schematic of compressor typical flow structures. Inspired by [6], [7] & [3].*

At finite blade ends, the endwall boundary layer cannot withstand the amount of diffusion required in the suction surface endwall corner and becomes prone to separation. This separation region is fed by endwall fluid that is overturned by the mechanism previously described leading to reduced turning in this region. On the surface of the blades, the boundary layers behave in a three dimensional way. They are inclined to be centrifuged radially outwards on rotors because they are travelling slower than the flow in the freestream region. On the other hand, in stator blade rows, radial equilibrium imposes a pressure gradient in the radial direction that tends to force the blade boundary layers radially inward.

Boundary layer development on aerofoil surfaces in multistage axial flow compressors is complicated and has been the subject of many extensive studies [8]. The findings of these studies suggest that the process of transition from laminar to fully turbulent is unsteady and heavily impacted by the incoming wakes from the upstream blade row. The process of transition is time-dependent as the wakes pass over the blade convecting disturbances and forming turbulent spots. As a result, the position of the start of the fully turbulent boundary layer is moving along the blade chord with time. Because of wake effects the boundary layer flows in compressors have an inclination to behave more like turbulent ones rather than laminar ones. As a result, roughly all blades with Reynolds numbers above about $2 * 10^5$ will have similar boundary layer characteristics and will not be prone to laminar boundary layer separations. Except for the very small compressors at high altitudes, this accounts for most engine compressors. Generally, increasing the Reynolds number of a compressor will decrease losses as the boundary layers thin until no further improvement is possible.

The flow patterns just described are well known and are generally categorised as secondary flows (apart from the transition). This is a slight misnomer since it may appear that they are insignificant. In fact, secondary flows tend to determine the behaviour of multistage compressor blade rows, specifically when the aspect ratios approach unity in the latter stages of a machine. They dictate the stall behaviour of the blade row and are accountable for at least half the losses. Another category of flows that influence compressor behaviour, includes flows associated with the mechanical design and real geometry of the machine such as shroud leakage flows and bleeds. These flows enter and exit the main annulus through axial gaps between rotating and stationary parts of the hub and bleed holes in the outer casing. This kind of flow disruption also influences the main flowfield and can alter the characteristics and magnitude of the secondary flows as well as creating losses. The various forms of flow mentioned above combine to create a highly complicated flowfield in a compressor blade that can be classified as unsteady, three-dimensional, and governed by viscous effects. [3]

So far, in this description, one of the most critical phenomena in compressors, stall or surge, has not been addressed. When the flow breaks down under rising adverse pressure gradients it is deemed that stall occurs in compressors . There are two forms of breakdown, one related with a short lengthscale disturbance known as a ‘spike’, and the second one is related with a longer lengthscale known as a ‘modal oscillation’. The ‘modal oscillations’ are associated with an overall instability across the compression system, while the ‘spike’ type of instability is associated with a disturbance in the flow happening locally, which is usually caused by high incidence at a rotor tip [9]. The most important mechanism for practical purposes is the ‘spike’ type. This breakdown take place near rotor tips in discrete patches, which have a rotational speed with the same direction as the rotor but at between 30 and 70% of the magnitude, as illustrated in figure 1.11.

This is known as part span rotating stall and may have several stall cells at first but as the stall develops they tend to coalesce into one cell. The instability in one blade row can influence the flow in the whole compressor, resulting in a complete breakdown of the structure of the flow through the whole machine, which is called surge. Nevertheless, in a multistage compressor, one or more blade rows may stall

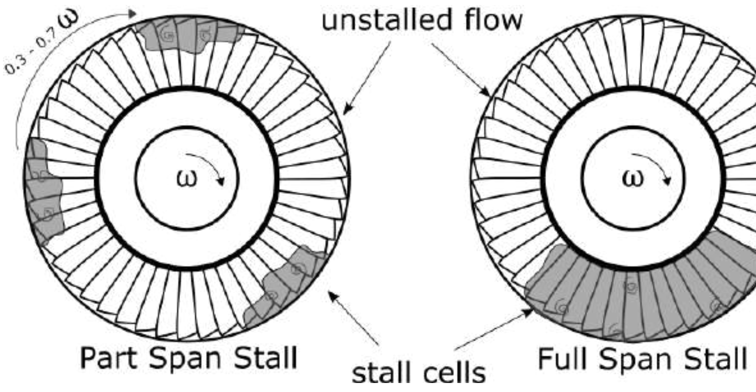

Figure 1.11: *Schematic diagram of rotating stall [6].*

without leading to a surge of the entire compressor. This mostly happens at low speeds, with the first stages of the compressor stalled but the rest of the machine still functioning normally. It is important for the designer to be able to anticipate the onset of stall because it is not permissible to operate a compressor in stall for any substantial portion of engine operation. However, it is clear from the foregoing explanation of the phenomenon that forecasting stall onset is a challenging task in compressor aerodynamics. [2]

1.4 The NASA 37 Case

In this thesis the open geometry of the NASA Rotor 37 will be studied. NASA Rotor 37 test case, designed and tested by Reid and Moore (Refs. [10] & [11]) at NASA Lewis Research Center, presently Glenn Research Center, is the isolated rotor of a low aspect ratio inlet stage for an eight-stage core compressor with a 20:1 pressure ratio. It was retested at NASA Glenn in isolation to avoid the interaction effects. As such the test case is ideal for code verification. Much data representing performance and flow field variables can be found in Ref. [12] which has been used for several CFD code assessment projects. In chapter 3 numerical results of the isolated Rotor 37 flow field computed by the PUMA GPU-enabled solver (see Appendix A) developed by PCOpt/NTUA ([13], [14], [15]) and the H3D multiblock Navier-Stokes analysis code developed by Hah (Refs. [16] & [17]) will be compared with available experimental data from NASA & AGARD (Refs. [11], [12] & [18]). Both H3D and PUMA codes have been widely applied to multiple applications and their numerical results have been cross-validated with test data for many different cases.

A picture of the experimental rotor geometry is given in Figure 1.12. Radial distributions of static and total pressure, total temperature, and flow angle were measured at two axial stations located 4.19 cm upstream and 10.67 cm downstream of the blade hub leading edge, labeled stations 1 and 4 in Figure 1.13. Detailed laser anemometry measurements were made of the velocity field within the rotor and wake at several axial stations and on five spanwise planes also shown in Figure 1.13.

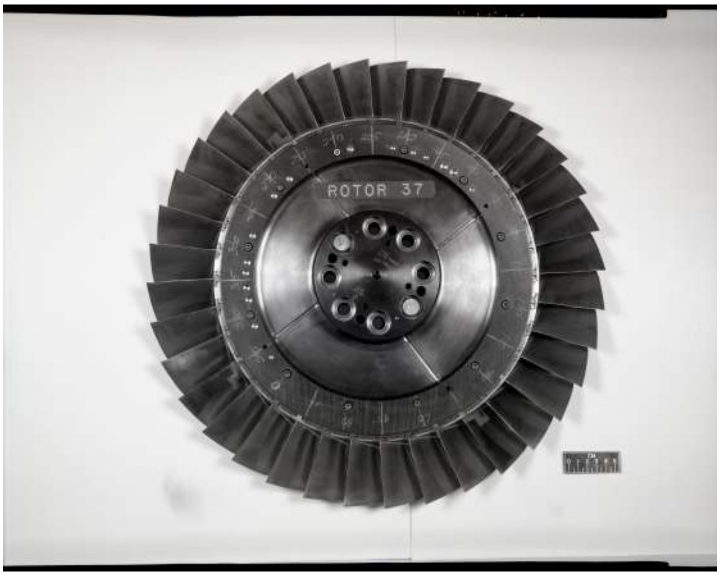

Figure 1.12: *Picture of NASA rotor 37*[19]

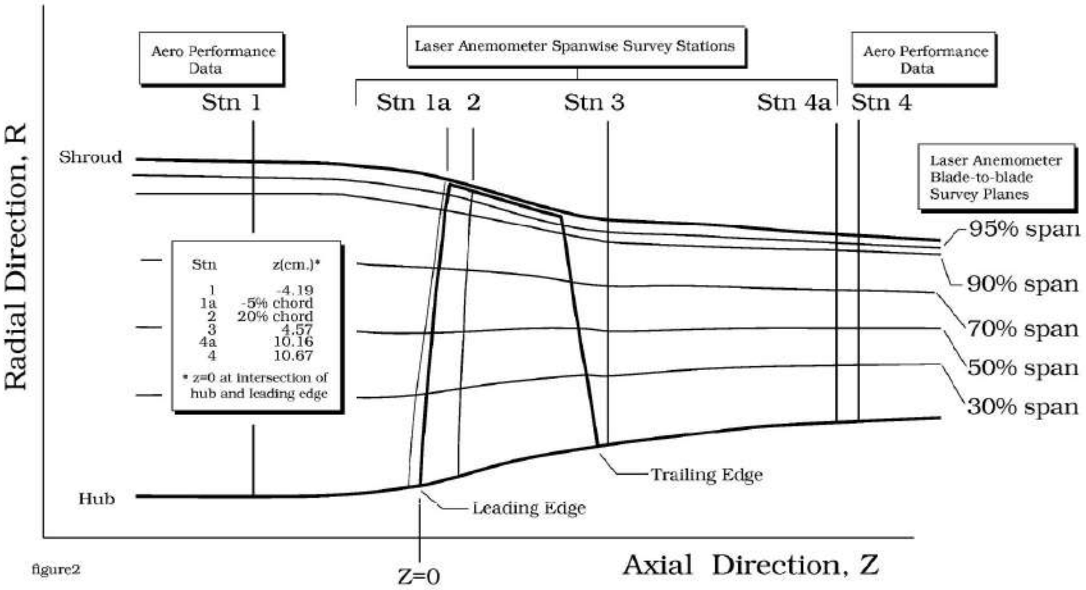

Figure 1.13: *Rotor 37 cross section and measurement stations [16]*

The IGTI of ASME sponsored a blind test exercise for turbomachinery CFD codes with this flow field at the 39th International Gas Turbine Conference held in The Hague, Netherlands (unpublished) in 1994. The same test case was later used by the AGARD Propulsion and Energetics Panel Working Group 26 as a CFD test case for examining the effects of grid and turbulence modeling on solution accuracy. Flow field at design speed was examined in detail. During these examinations most codes over predicted the overall pressure and temperature ratios and under predicted the efficiency. Predicted pressure ratios varied by nearly 10% and predicted efficiencies varied by about 6 points. At the same time the total pressure distribution downstream of the rotor below 40% span was also proven to be an area difficult to predict accurately. The data shows a region of low total pressure that has been called a "pressure deficit." This terminology implies that there is something wrong with the flow in that region and has prompted much discussion in the literature. Hah, et al. (Ref. [20]) suggested that the deficit is due to a corner stall on the rotor suction surface, while Chima, et al. (Ref. [21]) suggested that the low total pressure is an intrinsic feature of the rotor that tends to be smeared out by the central-difference schemes used by many CFD codes. The numerical results also over predicted the total temperature downstream of the rotor above 90% span by as much as $17C°$. The discrepancy was generally worse with algebraic turbulence models than with turbulent transport models.

1.5 The GPU-enabled CFD Solver PUMA

In order to predict the flow field in a turbomachinery blade passage, the compressible GPU enabled flow solver PUMA, developed by the PCOpt/NTUA ([13], [14], [15]), will be used in this thesis. This software numerically solves the Navier-Stokes equations along with the turbulence model equations in a computational domain, using the vertex-centered, finite volume method on unstructured grids consisting of tetrahedra, pyramids, prisms and hexahedra. Structured or matching block structured grids like the ones presented in this diploma thesis, are treated by PUMA as unstructured.

In the system of PDEs used to calculate the flow, the hyperbolic character of the terms dominates over the elliptic. Consequently, these equations are solved using a time-marching technique. Hence, the pseudo-time step is defined. At each pseudo-time step the system of equations is linearised, discretised and solved for the correction of the field variables for the next pseudo-time step. In case of time dependent problems, the time derivative remains in the initial equations and the pseudo-time derivative is artificially added. The system of equations is marched in time, with intermediate pseudo-time steps. In case of the incompressible flow equations, time marching techniques are not directly applicable. Consequently, methods such as the artificial compressibility method can be used. In order to solve the aforementioned system of Equations, discretization is applied. A finite volume is formed around each mesh node by connecting the edge midpoints, face centres and element barycentres of the edges, faces and elements attached to this node, respectively. The discretisation of the inviscid terms is made using Roe's approximate Riemann solver [22] while the viscous terms are discretised using a 2nd order central difference scheme involving all neighbours. After discretising all terms of Eqs. A.1, A.2 and A.3, a new system of equations is created which is solved using the explicit multi-stage Runge-Kutta method with residual smoothing using the point-implicit Jacobi method which does not require synchronizations in each iteration when the solution of the system is parallelized on GPUs.

The implementation of PUMA on GPUs provides a remarkable speed-up in comparison with CPU implemented software, reducing the turnaround time of a CFD analysis. Specifically, the implementation on GPUs is approximately times faster than the CPUs, comparing one card against one core. The GPUs that were used are NVIDIA Tesla K40. For further details on the topic, the reader is referred to ??.

1.5.1 Literature Review

In conventional aero-engine compressors, the flow field within flow passage becomes more and more complicated as the stage loading increases. In such cases the low aspect ratio is a significant feature for high-performance blades that have the requirement to maintain a wide operating range. With high blade loading, the streamwise adverse pressure gradient is exacerbated and the intensity of the secondary flow is extremely enhanced due to the increased circumferential pressure gradient. Low aspect ratio can contribute to reducing the adverse pressure gradient. Nonetheless, the decrease in blade height inevitably enhances secondary loss induced by thicker endwall boundary layer and increasing three-dimensional effects. Denton [6] pointed out that in a typical axial compressor, the endwall loss approximately accounted for 2/3 of the total loss. Therefore, it is essential to reduce endwall loss as much as possible to improve overall efficiency of the compressor and that can be achieved through some active or passive control measures.

For compressor stators, a variety of active and passive flow control measures can be applied to lower endwall loss, such as boundary layer suction, vortex generators, synthetic jet, bowed blading or casing treatment. However, for the rotors, considering the complexity of active flow control system installation, layout and the effect of some control methods on the blade strength, passive flow control technology-endwall contouring can offer significant advantages.The endwall contouring methodology includes axisymmetric profiling along axial direction and non-axisymmetric profiling along circumferential direction.

Most researches on endwall contouring start from application in the turbines. In the past decades, turbine axisymmetric contouring, namely two-dimensional endwall contouring shown in Figure 1.14, has been studied both computationally and experimentally, yielding improvements by reducing the intensity and size of the secondary vortices by contracting the flow area locally [23] - [24]. An experimental study of a nozzle guide vane axisymmetric/2D endwall contouring with low aspect ratio carried out by Burd and Simon [25] demonstrated that in contrast to the case with flat wall, the size and strength of the secondary flow with contoured endwall were greatly suppressed. As for the compressor, LeJambre et al.[26] showed that the hub profile within the rotor blade flow path had a significant influence on the performance. Based on the study of LeJambre et al., Stringhan et al. [27] carried

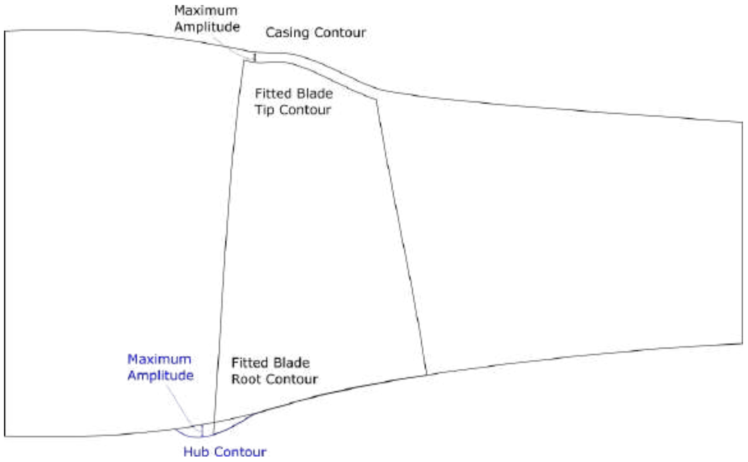

Figure 1.14: *Axisymmetric Endwall Contouring.*

out an application of axisymmetric contouring on all of rotor hubs from a nine stage compressor to reduce losses. Hoeger et al. [28] performed a series of experimental comparisons in transonic compressor rotor flow characteristics between a linear and a concave endwall contour and revealed that the concave endwall shape can unload the profile boundary layer while changing the original shock system from an oblique shock to a normal shock. Ito et al. [29, 30] investigated the effect of casing contouring on rotor flow instabilities and found that contoured endwall above the leading edge had notable improvement in stall margin and a slight decrease in efficiency and pressure ratio. Kroger et al. [31, 32, 33] conducted a series of casing contouring optimization researches for a subsonic/transonic rotor in order to decrease clearance flow losses effectively.

In order to reduce secondary loss, 3D non-axisymmetric endwall contouring can be proposed based on the flow physics that 3D contoured endwall interferes with the secondary flows and may lead to a drop in endwall losses through weakening the intensity and scale of the secondary vortex and changing the shock system near the endwall. There are many studies including numerical simulations and experiments on the application of endwall contouring on the turbines [34] - [35]. The favorable effect of non-axisymmetric endwall contouring was confirmed by Atkins [36], Harvey et al. [37], and Hartland et al. [38] Praisner et al. [39] and Knezevici et al. [40] investigated a series of blade airfoil and non-axisymmetric endwall contouring designs and proposed that non-axisymmetric endwall contouring is an effective method to reduce secondary loss.

As a matter of fact, the flow field is highly complex with respect to interactions between shock system and different vortices in a high-load cascade passage with a large flow turning. Therefore, the optimal axisymmetric endwall shape highly depends on the specific flow features. However, unlike the turbines, flow separation in a compressor is mainly dominated by streamwise adverse pressure gradient achieved by shock wave and change in flow area instead of secondary flow. As a consequence, the non-axisymmetric endwall contouring in the compressor may be not as effective as that in the turbine. Therefore, the main goal of this thesis is to investigate the effect of axisymmetric endwall contouring on the hub and the shroud of a high-load transonic compressor rotor.

1.6 Thesis Objectives, Motivation and Scope

This section is going to present the objectives, the motivation and the scope of this thesis. The main research questions of this thesis are the following:

- How does the axial location of the maximum depth of the endwall profile influence the performance of the NASA Rotor 37?
- Which fluid dynamics phenomena are different compared to the baseline geometry?

The objective of this thesis is to conduct a thorough analysis of the performance and operability impact of the endwall contouring of the NASA Rotor 37 using Design, Meshing and Computational Fluid Dynamics (CFD) tools (e.g PADRAM & PUMA). In order to achieve this objective a number of preliminary goals had to be accomplished:

- To parametrize and reconstruct the rotor blade.
- To create a set of hub surfaces that have convex valleys near the geometry of the blade.
- To create a set of casing surfaces that have concave peaks near the geometry of the blade.
- To create a combined case that has both its hub and casing surfaces perturbed near the geometry of the blade.
- To validate the modelled flow conditions at the NTUA in-house GPU-enabled CFD solver PUMA.
- To analyse the performance and operability of the rotor and the flow physics for both the baseline and the contoured rotor geometries.

In order to achieve the aforementioned goals the following methodology was followed:

- The original blade geometry was reconstructed from blade manufacturing coordinates provided in the NASA Technical Paper 1337 [10].
- 3D meshes of the isolated rotor blade were constructed using PADRAM.
- CFD simulations were performed using PUMA and were validated with available experimental data from literature.
- The hub and casing pertubations were defined using B-Splines

- The endwall geometry of the rotor was perturbed using PADRAM to produce the axi-symmetric endwall contoured geometry.
- The performance, operability and flow physics of the rotor were analysed under both the baseline and the perturbed rotor geometries using PUMA.

In addition to the above, CFD related issues such as the required size and shape of the domain, optimal solver settings as well as mesh quality were addressed.

Consequently, the aim of this thesis is to study the impact of the axial location of the minimum radial height of the hub line and the axial location of the maximum radial height of the casing line on rotor performance. As a result, 5 hub surfaces with a convex valey and 5 casing surfaces with a concave peak were simulated for a range of massflows. B-Splines were used to perturb the surfaces of the baseline hub and casing of NASA Rotor 37. These functions were selected in order for the resulting endwall contouring to have a maximum depth that is equal to 5% span of the blade. This value for the maximum depth was selected as it was deemed to be of sufficient size so as to influence the rotor endwall flow without creating immense acceleration of the flow over the contoured hub and casing curves, that could lead to possible local separations.

A CFD model, that was validated through comparison with experimental data, is used to simulate the flow characteristics of the transonic rotor with different axisymmetric endwall configurations. Firstly, the impact of different axisymmetric endwall shapes on the compressor rotor performance and operability is discussed and secondly the impact of endwall shapes on the flow field is investigated. Finally, the flow field detail of the optimal endwall shape is analysed and evaluated and some first design rules for the construction of axisymmetric end walls in a compressor could be derived.

Chapter 2

Blading Parametrisation, Meshing & Endwall Contouring

In this chapter, the actual reconstruction process of the NASA Rotor 37 that took place at Rolls-Royce plc. premices will be demonstrated, starting from the process of geometry extraction to obtaining the final 3D blade mesh. After the extraction of the baseline blade's aerofoil shaped sections from NASA, PADRAM was used for the generation of the computational mesh (Parametric Design and Rapid Meshing). PADRAM is a CFD mesh generation tool developed by Rolls-Royce plc. for turbomachinery component design that is also able to provide a set of parametrised design space to alter a given configuration. The baseline NASA Rotor 37 mesh configuration will serve two purposes; first to provide the ability of simulating the airflow inside the rotor blade passage accurately without the need of wall functions, and secondly to serve as a baseline geometry that will be perturbed with PADRAM to produce the different configurations with axisymmetric endwall contouring.

2.1 Blade Geometry Extraction

In this section, the extraction of the rotor blade geometry from the blade manufacturing coordinates provided in the NASA Technical Paper 1337 [10] is illustrated. In total 13 blade sections were extracted along with information that is utilised to create a computational domain that is fitted smoothly around the blade. In particular, a number of streamline sections, the inlet and exit air and metal angles and the radii of the leading and trailing edge were combined by PADRAM for this purpose. An illustration of the original NASA Rotor 37 shape along with various blade sections that were recreated is provided in Figure 2.1.

In Fig. 2.2 a schematic diagram of the three-dimensional geometry of the blade is depicted, while Figure 2.3 shows a 2D sketch of the investigated compressor rotor passage. It is worth noting that during this thesis the blade sections remained the

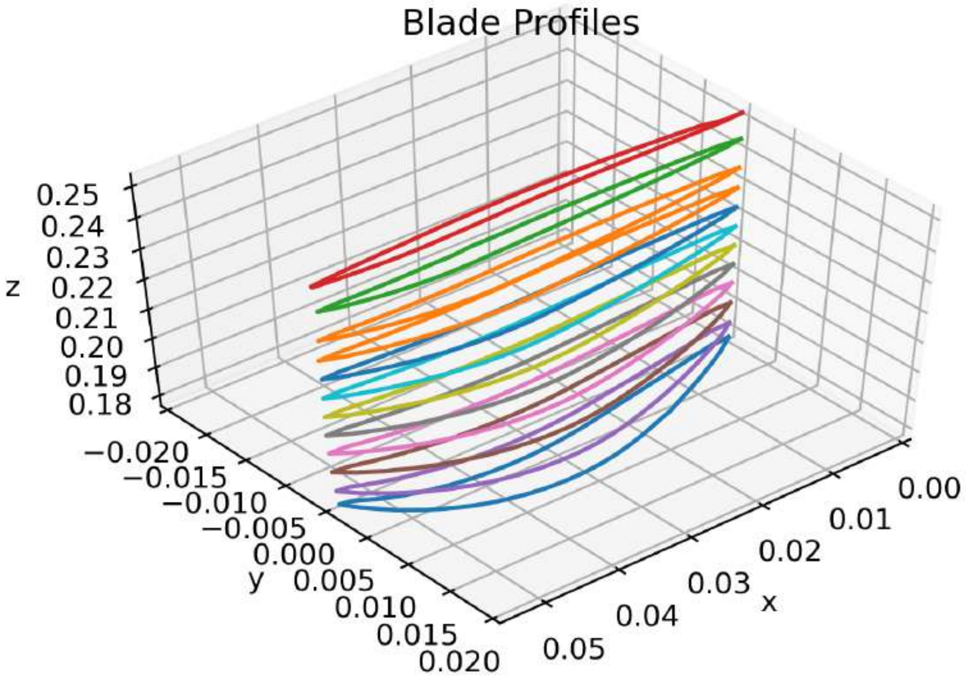

Figure 2.1: *Sliced 2D Profiles of the NASA Rotor 37.*

same. Some key design parameters of the rotor at design point are listed in Table 2.1. In the table the rotor total pressure ratio, the total temperature ratio and the adiabatic efficiency are defined as :

$$PR = (\overline{\frac{P_2}{P_1}}) = \frac{\int_{r_h}^{r_t} (\frac{P_2}{P_1})^{\frac{\gamma-1}{\gamma}} \rho v_z r \, dr}{\int_{r_h}^{r_t} \rho v_z r \, dr} \tag{2.1}$$

$$TR = (\overline{\frac{T_2}{T_1}}) = \frac{\int_{r_h}^{r_t} \frac{T_2}{T_1} \rho v_z r \, dr}{\int_{r_h}^{r_t} \rho v_z r \, dr} \tag{2.2}$$

$$\eta_{ad} = \frac{(\overline{\frac{P_2}{P_1}})^{\frac{\gamma-1}{\gamma}} - 1}{(\overline{\frac{T_2}{T_1}}) - 1} \tag{2.3}$$

where the subscript 1 corresponds to the instrumentation plane upstream of the rotor and position 2 to the instrumentation plane downstream of the rotor as shown in 1.13. Also, r_h and r_t are the hub and tip radius and v_z is the axial velocity.

The transonic compressor rotor enables a high blade loading coefficient without any flow control measures.

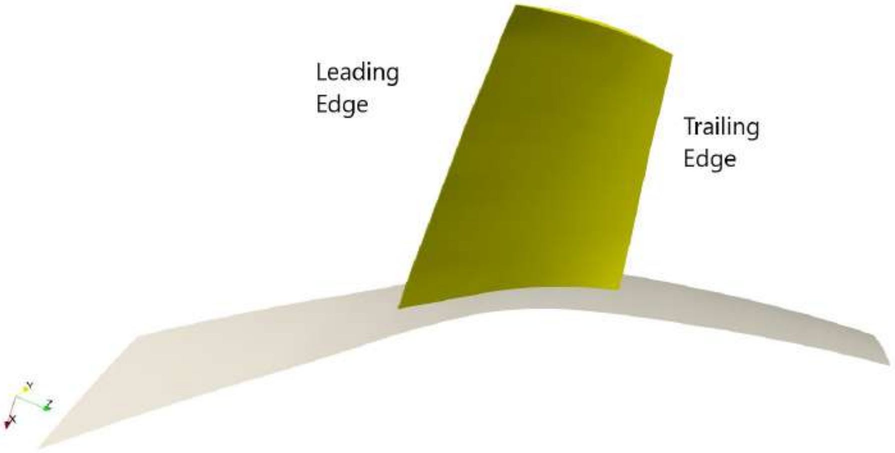

Figure 2.2: *3D View of the NASA Rotor 37.*

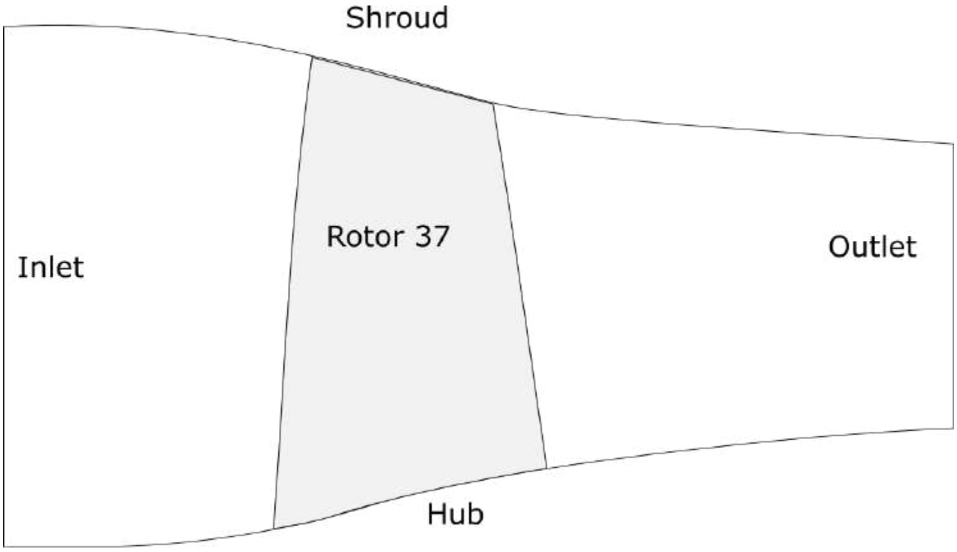

Figure 2.3: *Schematic diagram of the NASA Rotor 37.*

2.2 Mesh Generation

Grid generation for turbomachinery is well evolved for generating simple blade-to-blade mesh sections that are then stacked radially to create a 3D mesh. The typical types of meshes used in the field of turbomachinery CFD are block structured [41, 42], unstructured [43, 44], overset or the so-called Chimera [45, 46], hybrid

Parameter	**Value**
Rotor Total Pressure Ratio	2.106
Rotor Total Temperature Ratio	1.270
Rotor Adiabatic Efficiency	0.877
Mass Flow, kg/s	20.188
Rotor Wheel Speed, rpm	17188.7
Rotor Tip Speed, m/s	454.14
Hub / Tip Radius Ratio	0.70
Rotor Aspect Ratio	1.19
Number of Rotor Blades	36
Blading Type	Multiple Circular Arc (MCA)

Table 2.1: *Nasa Rotor 37 specifications.*

[47, 48, 49] and Cartesian grids [50]. Among the grid generation techniques, the block-structured is the most powerful and is the most established, in particular for turbomachinery aerothermodynamics. Complex geometries can either by meshed by unstructured grids or by structured multi-block grids. Unstructured grids typically have memory and CPU overheads due to the need to store mesh connectivity data, but offer the greatest geometrical flexibility. On-the-other-hand multi-block structured grids are very efficient and can fill-up topologically complex domain by decomposing the geometry into simple blocks.

A design cycle or an investigation study usually begins with a CFD solution for the base or reference geometry. After extracting the blade sections that define the blade geometry, the mesh generation parameters for the baseline geometry (without pertubed hub and casing surfaces) of the NASA Rotor 37 were defined and a mesh of a single passage was generated. This mesh was used in the validation process of the CFD solver PUMA that will be discussed in the next section. After validating the CFD results against experimental results, the mesh parameters and size were fixed throughout the computational evaluation process of the rotor with the contoured endwalls.

In this thesis, PADRAM was used for the generation of structured single passage meshes of the NASA Rotor 37, suitable for viscous CFD calculations. PADRAM makes simultaneous use of both transfinite interpolation and elliptic grid generators to generate meshes. An orthogonal body-fitted O-mesh is used to capture the viscous region in the vicinity of the aerofoil whilst an H-mesh is used near the periodic boundaries and where stretched cells are required, for example in the wake. The mesh is independently generated for every stream section, hence three-dimensional meshes are produced easily from stacked two-dimensional blade section meshes with no mapping required to transfer the meshes radially. This ensures that good quality meshes are created at every height even if the geometry is changing considerably from hub to tip.

The meshes were based on H-O-H multi-blocks. The O-mesh, that is used for the blade, is extended to capture the region of the aerofoil where the viscous phenomena of the flow are important. The H-mesh is used in the passages to link the O-mesh to the periodic boundaries and is used for the upstream and the downstream blocks. For the NASA Rotor 37 blading, PADRAM generated a mesh on the unwrapped-plane ($\theta - m'$ plane) of each stream-section that was extracted as mentioned in the previous section 2.3 and then each stream section was stacked-up in the radial direction to produce an intermediate stage mesh. The stream sections also define the extent of the inlet and exit planes. The final CFD mesh is then interpolated from the stream-section intermediate mesh to achieve a particular number of radial planes.

The blade geometry is defined at a number of radial stream sections. These radial sections lie on three dimensional surfaces defined in polar coordinates as $S_i(r, \theta, z)$, where i is the section index. Using non-dimensional parametric coordinates, m' and θ, a typical surface can be defined as [51]:

$$r_s = r(m, \theta) \tag{2.4}$$

$$\theta_s = \theta(m, \theta) \tag{2.5}$$

$$z_s = z(m, \theta) \tag{2.6}$$

where,

$$m' = \int_{z_0}^{z} \frac{\sqrt{dr^2 + dz^2}}{r(z)} \tag{2.7}$$

$$r = r(z) \tag{2.8}$$

where z_0 is an arbitrary reference and m' is a non-dimensional distance along a stream section which will be zero at z_0.

The starting point for PADRAM is to transform the radial stream sections into parametric two-dimensional planes, using the co-ordinates θ and m'. As r is greater than zero for any z coordinates, m' is a monotonic function of z, hence a unique inverse function exists to map the computational coordinates back to the physical, three-dimensional polar coordinates. The advantage of the above transformation is that the angles are preserved and the mesh-generation procedure deals with plane sections only [51].

PADRAM grid generation starts by dividing the computational blocks into sub-blocks for the purpose of generation of the algebraic grid and the control functions. Figure 2.5 shows the O-type grid around the blade and H-type grid near the periodic

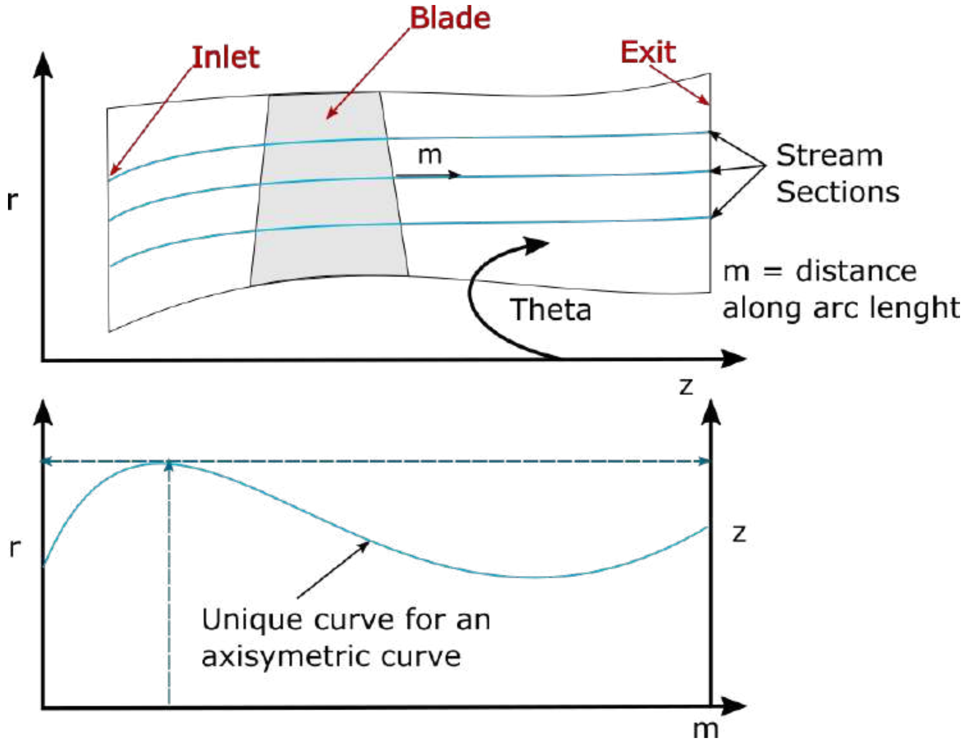

Figure 2.4: *r, θ, z cylindrical coordinates(top); m, r, z mapping diagram(bottom).*

boundary, upstream and downstream blocks, as previously mentioned. Transfinite interpolation (TFI) [52] is then used to generate the initial grid based on a linear interpolation of the specified boundaries.

The transfinite interpolation transforms a rectangular computational domain to a physical domain with irregular boundaries. With the transformation, the discrete points in the computational domain map into irregular spaced points in the physical domain creating a physical grid. The spacing between points in the physical domain is controlled by the blending functions. Blending functions that produce the desired shape of a grid (i.e., relative orientation between points) may not produce the desired spacing between points. In order to create grids with desired grid refinement, the blending functions can be designed or modified to exactly produce the desired streching. Also, for this purpose control functions that manipulate the grid point spacing can be applied. PADRAM uses the following double clustering functions [51]:

$$y = \frac{(2\alpha+\beta)[\frac{\beta+1}{\beta-1}]+2\alpha-\beta}{(2\alpha+1)[1+(\frac{\beta+1}{\beta-1})^{(\frac{\eta-\alpha}{1-\alpha})}]} \tag{2.9}$$

$$1 < \beta < \infty \tag{2.10}$$

$$0 \leq \alpha \leq 1 \tag{2.11}$$

where η is the non-dimensional grid point distribution in the computational plane, β is the clustering function, more clustering is achieved by letting β to approach 1 and α is a non-dimensional quantity that indicates which grid location the clustering should be attracted to, e.g. a value of 0.5 ensures clustering is uniformly done at both ends.

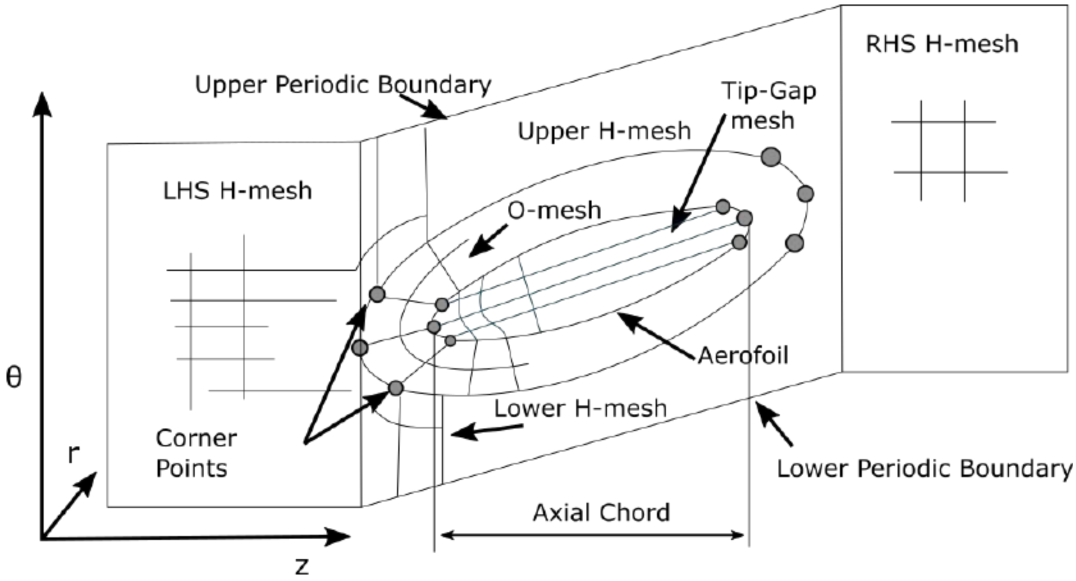

Figure 2.5: *Single Passage mesh*

To smooth the grids that were generated by the transfinite interpolation in each block PADRAM solves a system of elliptic partial differential equations (PDEs) too. For each radial height, the following equations are solved :

$$\alpha m_{\xi\xi} - \beta m_{\xi\xi} + c m_{\eta\eta} = P(\xi, \eta) \tag{2.12}$$

$$\alpha \theta_{\xi\eta} - 2\beta\theta_{\xi\xi} + c\theta_{\eta\eta} = Q(\xi, \eta) \tag{2.13}$$

where,

$$\alpha = m_\eta^2 + \theta_\eta^2 \tag{2.14}$$

$$\beta = m_\xi m_\eta + \theta_\xi \theta_\eta \tag{2.15}$$

$$c = m_\xi^2 + \theta_\xi^2 \tag{2.16}$$

P and Q are the forcing functions to ensure orthogonality and grid clustering at the surfaces. However, in this thesis these functions were switced off and the grid orthogonality near the surfaces was ensured by using a hyperbolic-type grid generation to generate the O-grids, that is using a marching procedure to grow the grid normal to the boundaries. Equations 2.14 - 2.16 can be solved by an iterative solver such as the Gauss-Siedel scheme or a point successive over relaxation scheme (PSO). PADRAM makes use of the latter scheme to elliptically smooth the transfinite interpolation generated grids [51]. Figure 2.6 shows the PADRAM mesh topology for a single vane mesh. The upstream and downstream H-mesh can also be rotated to align the mesh with the blade inlet and exit metal angles.

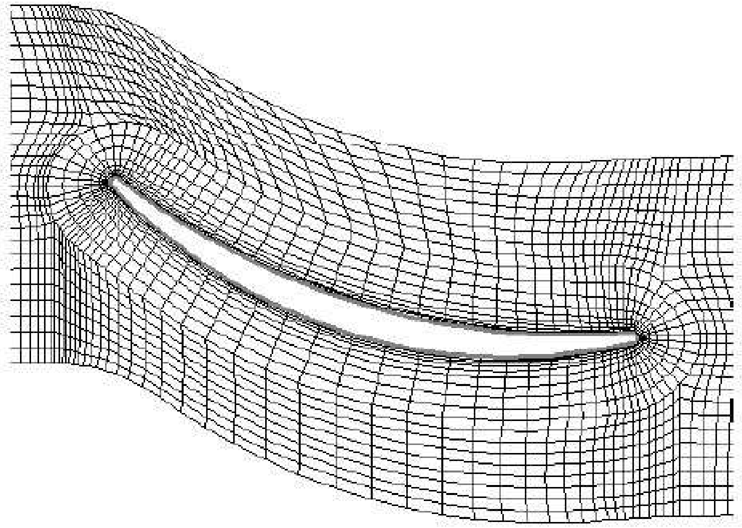

Figure 2.6: *PADRAM mesh for a compressor blade H-O-H topology [51].*

Tip clearance is often required for shroudless rotor compressor blades and a good quality mesh is required for the tip leakage flows not to be poorly resolved. If the number of points in the tip clearance is too low, then the complex physical phenomena that occur there cannot be accurately modelled. In PADRAM once the O-grid is generated with the outer domain of the blade, the grid corresponding to the solid part of the domain is constructed using the same boundary node distribution. It is important to keep the mesh spacing in the inner and outer part of the wall as close as possible to each other. Figure 2.7 shows a typical tip gap mesh for a compressor rotor generated in PADRAM (the tip gap has been increased to 5% span for demonstration). This was achieved using specified clustering parameters.

Some of the details of the base mesh used for the initial geometry of NASA Rotor 37 can be seen in Figures 2.5 and 2.9. In this mesh, 24 O-mesh layers were generated while the thickness of the O-mesh and the placement of the O-mesh corner nodes at the leading and trailing edge respectively was adjusted in order to keep the skewness of the mesh at a minimal level.

Moreover 80 nodes were used for the across the passage region, while 35 and 40 nodes were used for the downstream and upstream areas of the H-mesh respectively. For the middle block of the H-mesh 120 axial nodes were generated. In the tip region 20 layers at the internal O-mesh and 40 grid points across the span of the tip clearance

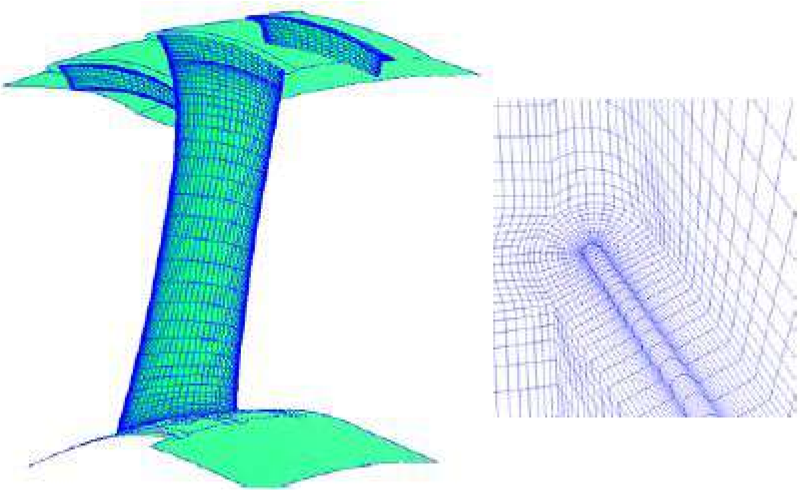

Figure 2.7: *PADRAM's multi-passage tip clearance model (5% gap for demonstration) [51].*

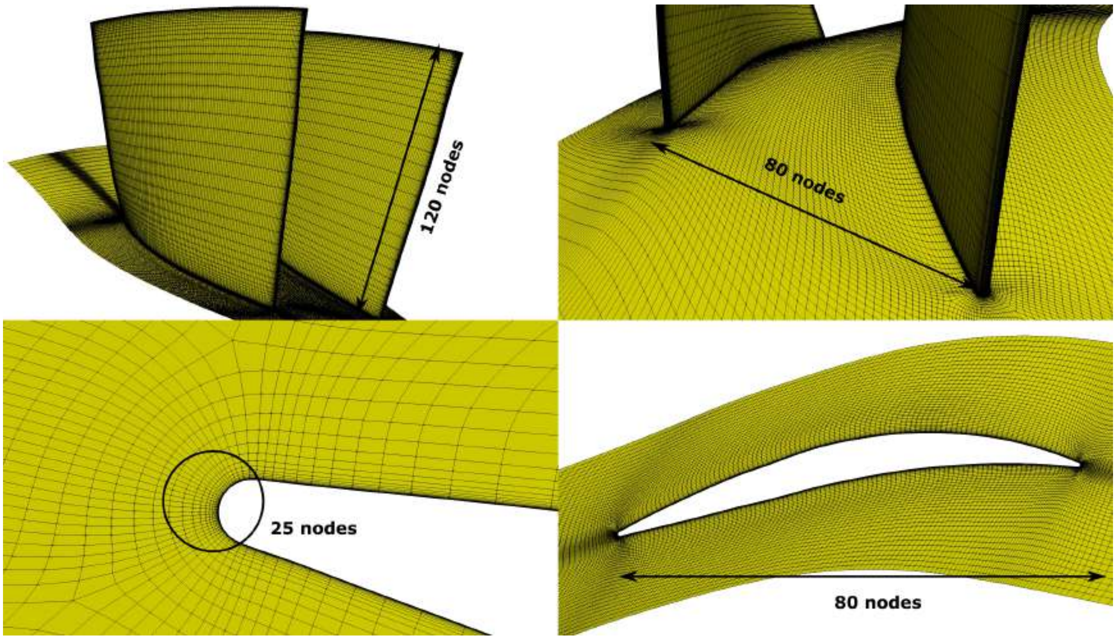

Figure 2.8: *Details of the NASA Rotor 37 baseline mesh.*

were used,while the gap was set equal to $0.400mm$ according to the reports of Suder [5]. Finally, 120 nodes were created for this mesh in the radial direction leading to a mesh approximately containing a total of 2.8 million cells. The entire grid has a high quality with the minimal skewness angle of 29 deg. The first cell width near the wall is set to be $1x10^{-6}mm$ in order to ensure that the average value of $y+$ is below 1.

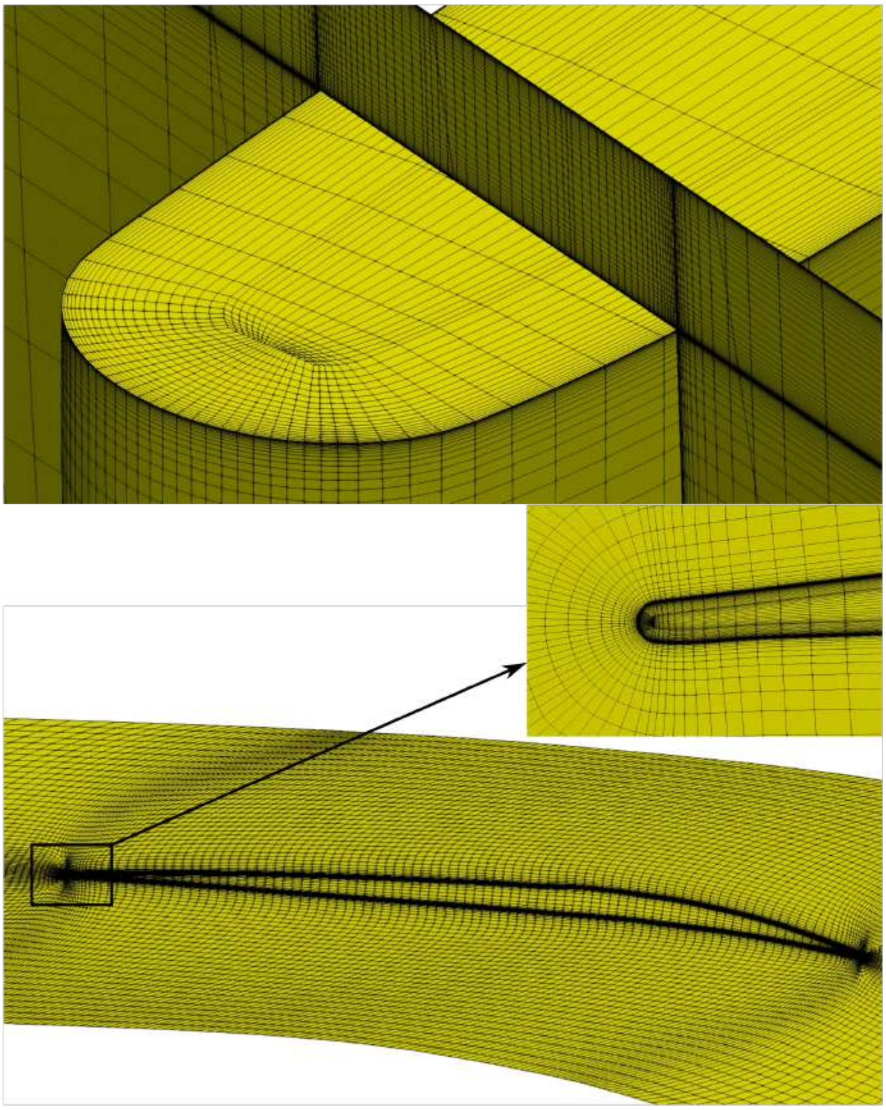

Figure 2.9: *Details of the NASA Rotor 37 baseline mesh.*

2.3 Axisymmetric Endwall Contouring

This section presents the tools and methods that were used to create the axisymmetrically contoured endwalls used for the investigation study carried out in this thesis.

In particular, PADRAM was used to parametrically change the axisymmetric endwall geometry. The lower and upper endwalls were defined and parametrised by B-Spline control points with (x,r) coordinates. The first coordinate represents the axial position of the control point, while the second its radial location. The geometry of the endwalls is assumed to be axisymmetric, hence avoiding the need for the third spatial coordinate. The B-Spline control points defining the endwalls geometry are obtained with a custom Python script developed for this thesis. This script extracts the initial geometry of the annulus line, applies a user specified perturbation, fits a B-Spline to the final curve with a specified accuracy and writes the control points coordinates into a PADRAM input file. This method provides the ability to generate any possible shape giving complete freedom in the choice of the endwall perturbation. It also allows the user to calculate the shape of the curve prior to the mesh generation to check its quality. Figure 2.10 shows an example of this endwall design modification.

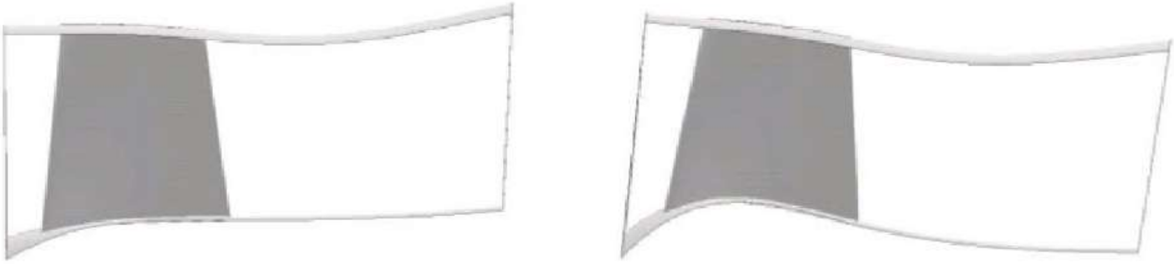

Figure 2.10: *Lower Endwall change (in the aerofoil passage) obtained by the radial displacement of one control point: Base geometry (Left); Modified geometry (Right).*

As mentioned the present investigation study focuses on the impact of axisymmetric endwall contouring on the performance of the rotor, including the overall characteristic lines at design speed and the flow behaviour near peak efficiency and near stall. Figures **??** & **??** show a schematic diagram of all the axisymmetric contoured endwall shapes constructed by virtue of the aforementioned B-spline and Table 2.2 lists the details for all the configurations studied in this thesis. In particular, the perturbation functions shown in Fig. 2.11 were overlaid on the annulus curve of the rotor to generate the axisymmetric endwall contouring.

The aim of this thesis is to study the influence of the endwall contouring and specifically the impact of the axial location of the minimum radial height of the hub line and the axial location of the maximum radial height of the casing line on rotor performance. As a result, the perturbation functions, that were constructed for this investigation study, differ only at the axial location of their peak. These functions are radially subtracted from the hub line in order to produce a concave shape, whereas they are radially added to the casing line in order to produce a convex shape as shown in Figure 2.12. The axial positioning of the peak was investigated through 5 different configurations both on the hub and shroud of the blade. All the perturbation functions were selected in order for the resulting endwall contouring to have a maximum depth that is equal to 5% span of the blade. This value for the maximum depth was selected as it was deemed to be of sufficient size so as to influence the rotor endwall flow without creating immense acceleration of the flow over the contoured hub and casing curves, that could lead to possible local separations.

The naming convention followed in this investigation regarding the axial positioning

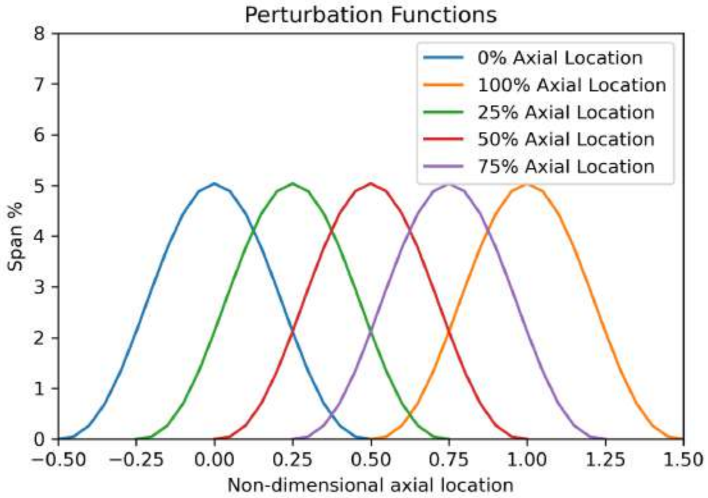

Figure 2.11: *Perturbation functions.*

Endwall Contouring Parameters	
Axial positioning of the maximum amplitude	Maximum perturbations magnitude
0% chord	5% span
25% chord	5% span
50% chord	5% span
75% chord	5% span
100% chord	5% span

Table 2.2: *Table with all the cases of the investigation study.*

of the peak of the perturbation, is given as a percentage of the blade's chord - 0% is at the leading edge of the blade and 100% at the trailing edge.

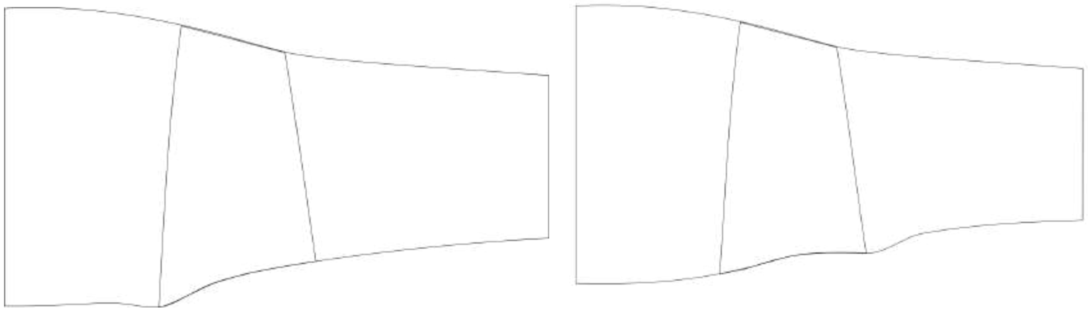

(a) *Meridional schematic diagram of hub endwall contour at 0% Axial Position.*

(b) *Meridional schematic diagram of hub endwall contour at 100% Axial Position.*

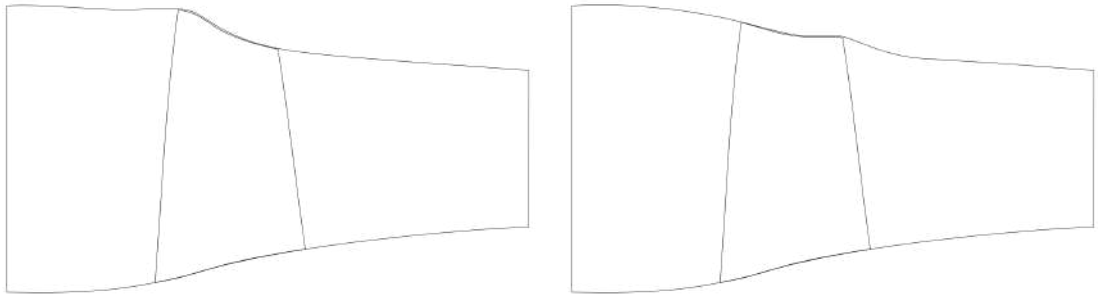

(c) *Meridional schematic diagram of casing endwall contour at 0% Axial Position.*

(d) *Meridional schematic diagram of casing endwall contour at 100% Axial Position.*

Figure 2.12: *Meridional schematic diagram of endwall contouring on rotor 37.*

Chapter 3

CFD Analysis of NASA Rotor 37 - Validation

NASA Rotor 37 is a low aspect ratio inlet rotor for a core compressor. It has 36 multiple circular-arc (MCA) blades and a design pressure ratio of 2.106 at a mass flow of 20.19 kg/sec and has been tested multiple times in different facilities as a single rotor and also with a stator. The specifications, given in Table 2.1, are the intended design parameters and are reproduced from Suder [12].

3.1 Comparison of PUMA results with experimental data

In Ref. [16] Reynolds-Averaged Navier-Stokes (RANS) calculations using a grid of 1.8 million cells generated with GridPro and the k-omega turbulence model, were performed first to obtain compressor characteristics at the design rotor speed with the H3D code. The calculated flow fields from H3D and the measured data from NASA & AGARD were compared with the results of PUMA, that were produced using the Spalart-Allmaras turbulence model and a grid of 2.8 million cells generated with PADRAM.

As far as the boundary conditions are concerned the outlet static pressure was specified at the hub radius and, then, the radial distribution of static pressure from hub to tip/casing is computed by solving the radial equilibrium equation. Moreover, distributions of total pressure and total temperature provided by Suder et al [5] were used at the inlet, while the flow direction was set to be perpendicular to the inlet plane. Each evaluation has a total duration of approximately 4 hours and the CFD solver runs on one NVIDIA Tesla K40 GPU. For more information about the CFD setup the reader is referred to the Appendix A. The comparison of total pressure, total temperature ratio and isentropic efficiency characteristics of the rotor at the design rotor speed are shown in Figures 3.1 - 3.3.

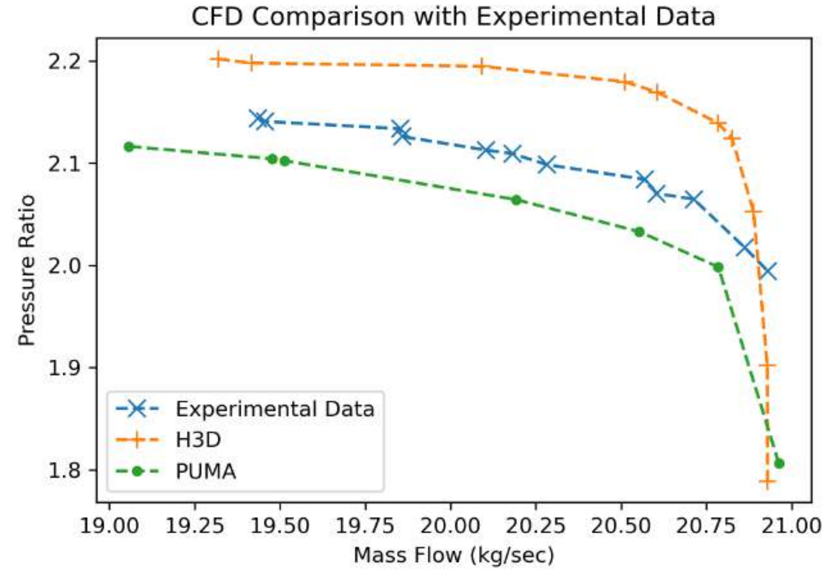

Figure 3.1: *Pressure ratio characteristics of the rotor at design rotor speed.*

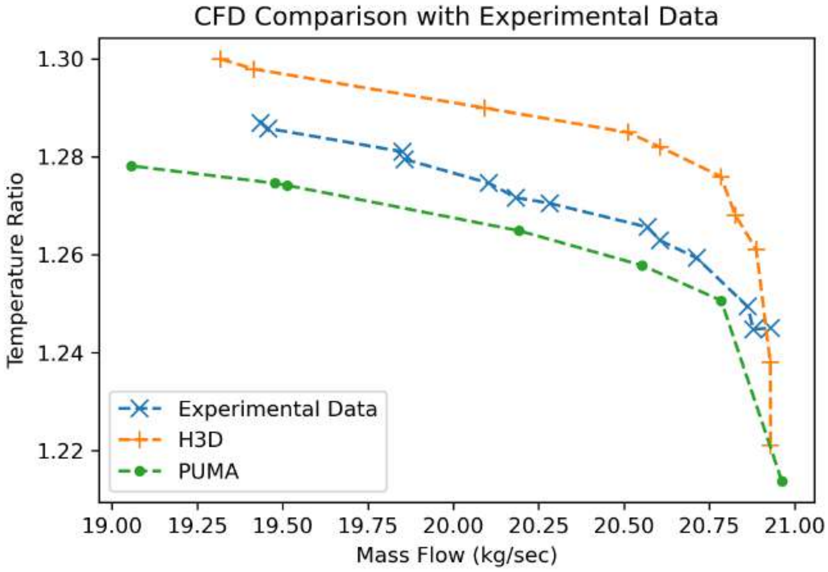

Figure 3.2: *Temperature ratio characteristics of the rotor at design rotor speed.*

The choke mass flow was calculated as $20.94kg/s$ with RANS and the measured choke flow rate is $20.93kg/s$. PUMA calculates the choke mass flow rate within the measurement error range. Suder and Celestina [5] reported uncertainty range of the measurements in Figures 3.1 - 3.3. Results shown in Figures 3.1 - 3.3 show that the H3D code calculates more optimistic performance of the compressor than the measurement, where as PUMA tends to under predict the performance of the

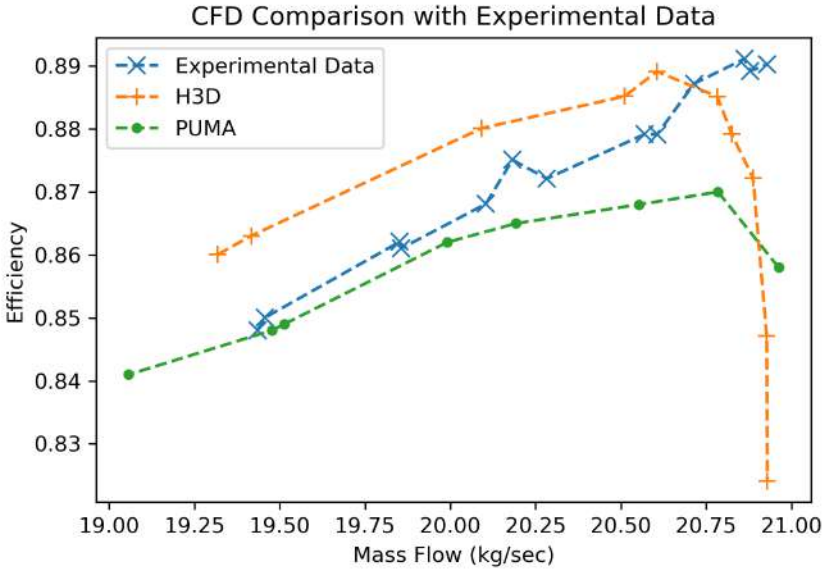

Figure 3.3: *Isentropic efficiency of the rotor at design rotor speed.*

rotor. Specifically, higher pressure and temperature ratios are calculated by H3D compared to the measurements, while PUMA calculates lower values. However, the overall trend is fairly well captured. The PUMA code calculates changes in isentropic efficiency at different operating conditions fairly well even though the computed values are lower than the measured values. PUMA tends to predict the choke conditions with satisfactory accuracy, with a negligible difference in mass flow, -3.5% difference in efficiency, 7.5% difference in pressure ratio and 2.5% difference in temperature ratio. The measurements show some unusual compressor performance near the choke condition, which can be contributed to some measurement uncertainty as already mentioned in [5]. At the same time, taking into account the fact that the difference between the calculated pressure ratio by H3D has a difference smaller than 1% with the pressure ratio calculated from PUMA, it was deemed that the accuracy of the simulation is sufficient near choke. Near peak efficiency conditions there is 1% difference in mass flow, 2.5% difference in efficiency, les than 0.5% difference in pressure ratio and 3% difference in temperature ratio. Finally, near stall conditions there is a 2% difference in mass flow, 1% difference in efficiency, 1% difference in pressure ratio and 1% difference in temperature ratio. Overall, PUMA computed the performance of the rotor accurately across the different flow conditions.

Detailed flow structures at the near peak performance and near stall are examined with the numerical solution and its comparison to the experimental data collected from the laser anemometry spanwise survey stations. In Figures 3.4 - 3.8 radial distributions of total pressure and temperature ratios, exit flow angle, isentropic efficiency and tangential velocity are shown. In order to derive the pitch-wise averaged radial distributions PUMA calculates 2D sections of constant span, where the first and last section radial width as well as the number of the sections are defined by the user. In every zone the mean values for the flow variables of interest are calculated using massflow averaging. Specifically a total of 21 zones were created and a hyperbolic tangent function was used for their distribution. The massflow-averaging was conducted by integrating the product of the flow rate with the flow variable of interest and the result was divided by the total mass flow through each zone.

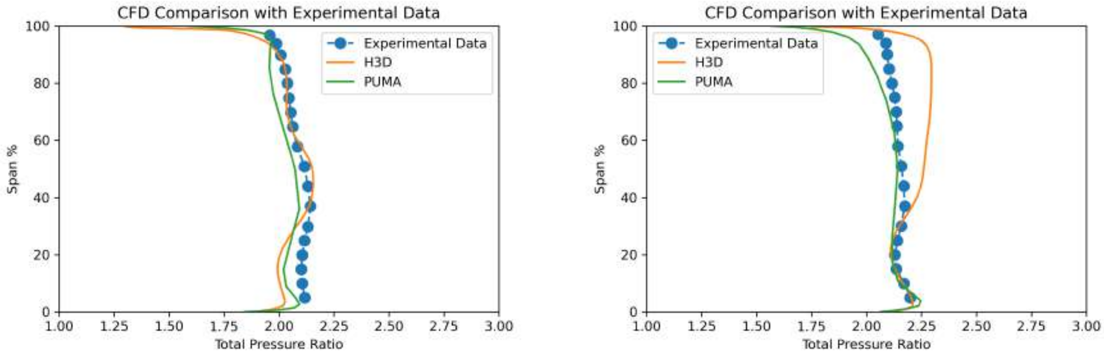

(a) *NASA Rotor 37 Total Pressure Ratio spanwise profiles near peak efficiency.*

(b) *NASA Rotor 37 Total Total Pressure Ratio spanwise profiles near stall.*

Figure 3.4: *NASA Rotor 37 Total Total Pressure Ratio spanwise profiles.*

Computed distributions of total pressure ratio from both H3D and PUMA are compared with measured values in Figure 3.4 at peak efficiency and near stall. Results in Figure 3.4 show a clear trend. The computed and experimental data are in qualitative agreement and the total pressure deficit near the hub is clearly calculated near peak efficiency and stall conditions. To study the origin of this pressure deficit near the hub,the calculated flow field will be further examined. The total pressure spanwise distribution computed from PUMA is slightly underestimated across the span near peak conditions efficiency whereas near stall conditions the profile is mainly underestimated near the tip region. On the other hand H3D underestimates lower span areas near peak efficiency and overestimates higher span areas near stall. The tip region deficit is more apparent near stall conditions for both solvers. This might suggest that the interaction between the passage shock and the tip leakage vortex is not captured completely. However, upon averaging the total pressure distributions the overall total pressures are in accordance with the experimental data, as shown in the rotor performance map in Fig. 3.1. The pressure distribution near the hub section is predicted fairly well.

The computed exit flow angle shown in Figure 3.5 is in good qualitative agreement. Near peak efficiency, the middle part of the spanwise distribution is constant about 42 degrees, while the tip and hub regions show an increase of exit flow angle, which is in accordance with the experimental data too. This pattern is similar near stall conditions too, with the middle span area having a constant exit flow angle about

40 degrees and the endwall regions being overturned.

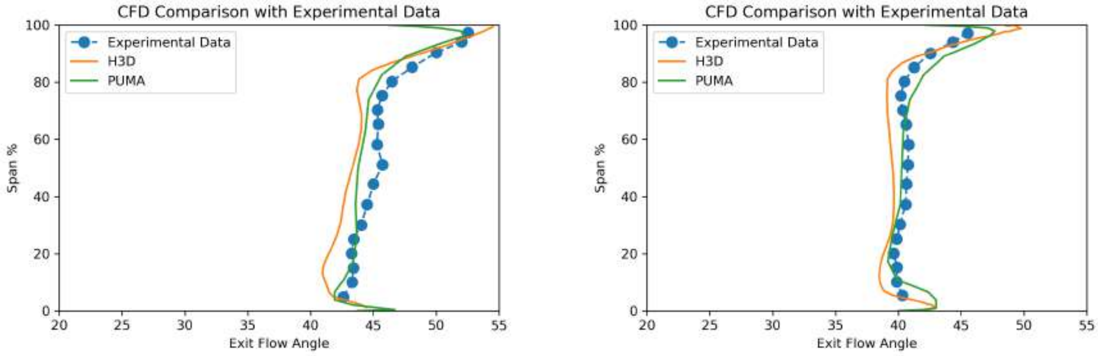

(a) *Rotor 37 Exit Flow Angle spanwise profiles near peak efficiency.*

(b) *Rotor 37 Exit Flow Angle spanwise profiles near stall.*

Figure 3.5: *Rotor 37 Exit Flow Angle spanwise profiles.*

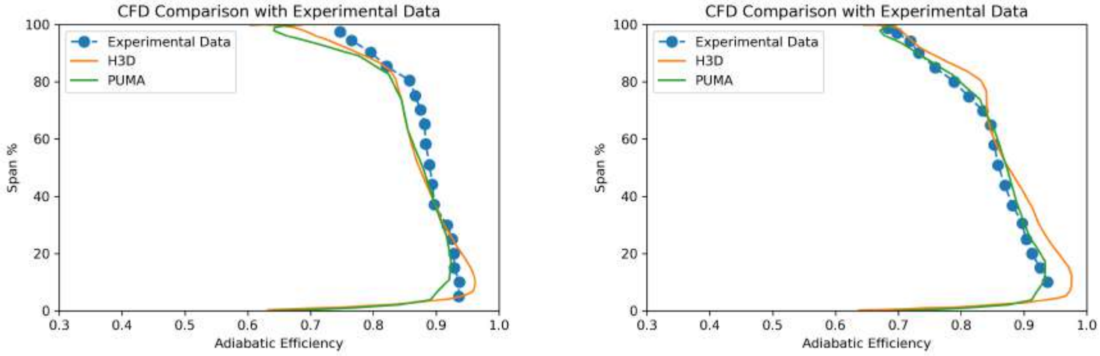

(a) *Rotor 37 Isentropic Efficiency spanwise profiles near peak efficiency.*

(b) *Rotor 37 Isentropic Efficiency spanwise profiles near stall.*

Figure 3.6: *NASA Rotor 37 Isentropic Efficiency spanwise profiles.*

Consistent with the rotor performance map, the isentropic efficiency spanwise distribution is generally under predicted by PUMA. The increase in exit flow angle indicates an overturned boundary layer and increased losses near the endwall regions. This observation is in accordance with the spanwise distributions of the isentropic efficiency shown in Figure 3.6a. Specifically, near peak efficiency compared to the experimental data PUMA tends to underpredict the profile near the hub from 0% to 20% span, near higher span from 55% to 65% and near the tip region. On the other hand, the distribution of efficiency near stall is in greater agreement with the experimental data, as expected from Fig.3.3. The lower span deficit in efficiency that appears in the results in Figure 3.6 suggests that there is a three-dimensional corner flow separation near the hub. Rotor 37 is a highly loaded transonic compressor rotor. Due to very high aerodynamic loading, the passage shock extends all the way to the hub. The three-dimensional corner separation is due the interaction of the passage shock with the hub boundary layer. The total pressure deficit near the hub shown in Figure 3.4 is the result of this corner flow separation. Near the tip region, the decrease in efficiency can be attributed to the tip leakage vortex and the increased mixing losses that the vortex induces due to increased shear rates inside the vortex, combined with the shock interaction and the endwall losses.

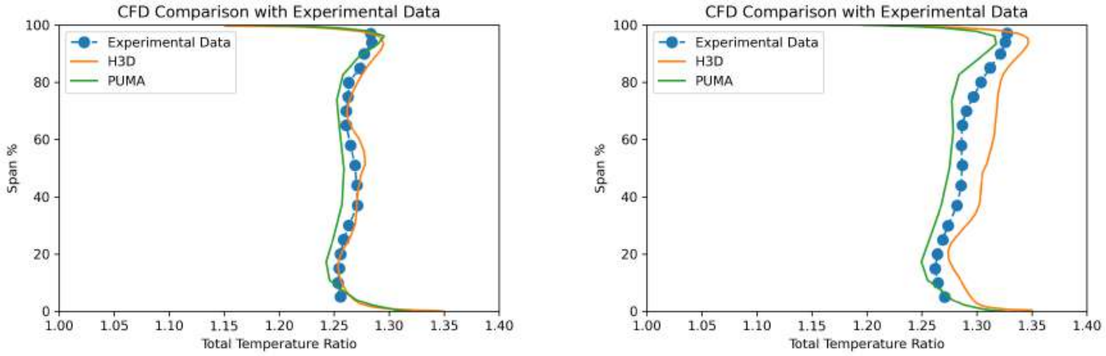

(a) *Rotor 37 Total Temperature Ratio spanwise profiles near peak efficiency.*

(b) *Rotor 37 Total Temperature Ratio spanwise profiles near stall.*

Figure 3.7: *NASA Rotor 37 Total Temperature Ratio spanwise profiles.*

Distributions of total temperature ratio near peak efficiency and stall conditions are compared with the measurement in Figure 3.7. The shapes of the temperature profile are very similar and overall, numerical results agree better near the middle span areas, whereas near the hub section there is an increase in the deviation between the CFD results and the experimental data for both solvers. Near the tip region the experimental data show an increase in the total temperature ratio both near peak efficiency and near stall. This trend is captured by PUMA despite the fact that near stall the total temperature ratio distribution is slightly underpredicted, again in accordance to the data shown in the rotor performance map . Unlike most previously reported CFD results, the PUMA code predicts lower temperature ratio toward the casing both near the peak efficiency and stall conditions. Compared to published results from different codes, the calculated temperature rise agrees fairly well with the measurement.

The distribution of tangential velocity at both ends of the rotor performance is shown in Figure 3.8. Despite the fact that there are some deviations that emerge for the tangential velocity in the endwall region, which leads to a discrepancy of the flow angle in this region, the computational results coincide well with the overall pattern of the experimental measurements. Because there is only one measuring pont arranged along the radial azimuthal direction for each spanwise location at the outlet plane, some discrepancies may be induced between experimental and numerical results.

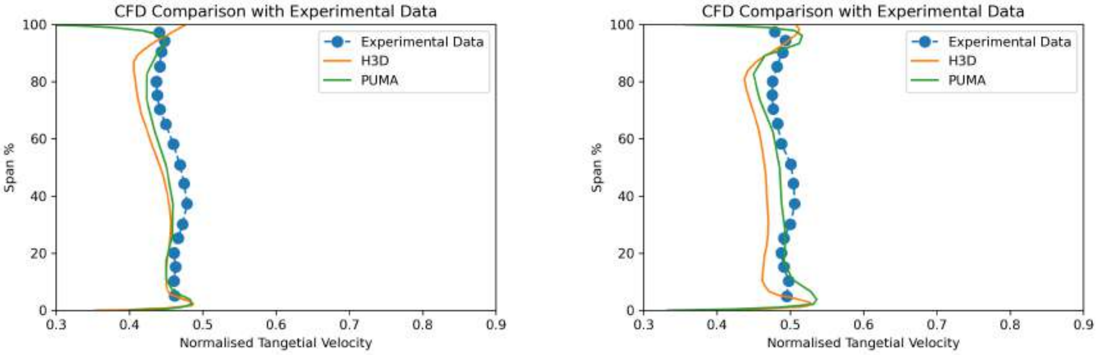

(a) *Rotor 37 Tangential Velocity spanwise profiles near peak efficiency.*

(b) *Rotor 37 Tangential Velocity spanwise profiles near stall.*

Figure 3.8: *NASA Rotor 37 Tangential Velocity spanwise profiles.*

The solution at 70 percent span section, in terms of Mach number for the near peak efficiency condition, is shown in Figure 3.9 and it is compared with the solution of H3D and the expriemental result gathered by Suder et al. [5]. The overall flow field is in good qualitative agreement with the measured data for the key flow structures of the rotor, such as the bow shock,the wake of the blade the shock position inside the passage and its interaction with boundary layer. In particular, the bow shock is attached to the leading edge of the blade and extends up to the suction side of the blade. The low-Mach number region observed near the suction side of the blade is a shock induced separation that increases the trailing edge diffusion driven separation. Although the computed wake profiles are sharper than the experimental profiles close to the trailing edge of the blade, they are similar to the measured ones.

Furthermore, a brief summary of the main flow features of Rotor 37 is presented.

- **Shock-wave system:** A strong shock-wave system is observed in the rotor geometry at the design speed. The shock-wave extends over the majority of the blade span. For the Rotor 37, an oblique shock is observed within the blade passage, at near choke conditions. This shock moves upstream when the compressor is near the peak efficiency. At this condition, a strong shock is observed attached near the leading edge of the blade. This shock ultimately transforms in to a single strong detached bow shock near the stalling conditions, resulting in an increase of the passage flow blockage.

- **Interaction tip leakage flow/shock wave:** A lot of studies have been performed in the past to analyse the effect of the tip leakage vortex on the rotor performance, and also its interaction with the shock wave system. The tip leakage vortex plays a vital role for the inception of the instabilities inside the blade passages. The interaction results in a certain spillage, and the mass-flow blockage. This mass-flow blockage moves upstream of the blade passage, as the rotor shifts from the near peak efficiency to the near stall operating

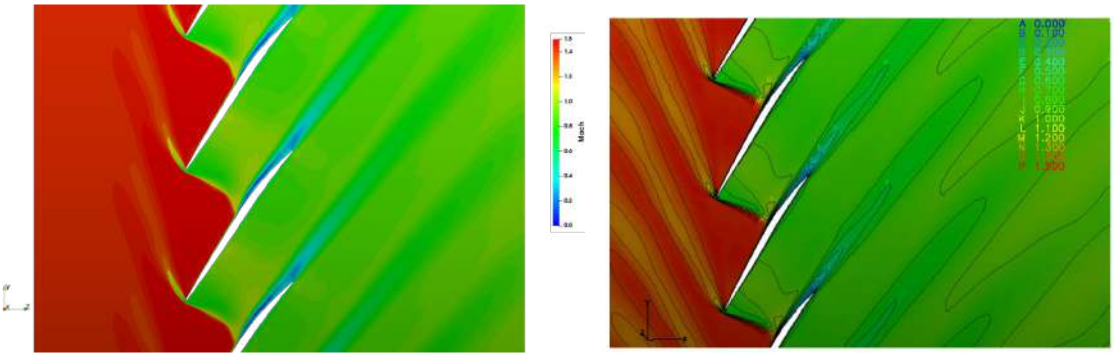

(a) *PUMA solution.* **(b)** *H3D solution.*

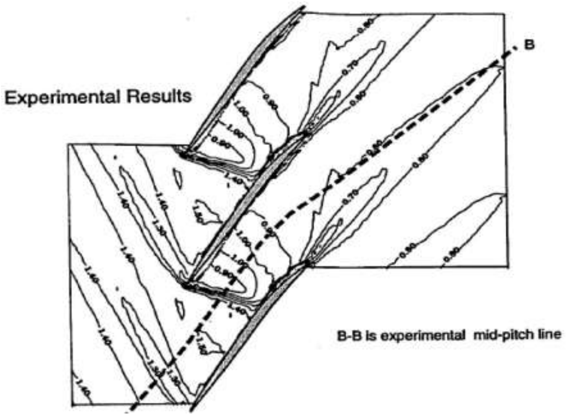

(c) *Experimental measurements.*

Figure 3.9: *Blade to blade Mach number contours of NASA Rotor 37 at 70% span near peak efficiency*

conditions. This ultimately causes the flow spillage to move to the adjacent blade passages, which may result in the part-span stall of the annulus.

- **Hub corner stall:** This flow-feature is observed at all the operating conditions near the suction surface of the blades. It grows in size as the compressor moves from choking to stalling operating conditions. However, it is reported that it is a common feature of transonic rotors, and the effects on the rotor performance diminishes at the higher rotor rotational speeds. Thus, this should not be the prime reason for the stall inception. Examples of the hub corner stall in the Rotor 37 near the trailing edge of the suction surface can be seen in Figure 3.10, where the Q-criterion is used for the visualisation of the three-dimensional flow structure of the horseshoe vortex near the hub of the rotor. In particular, it is defined in terms of the instantaneous velocity gradient tensor as:

$$Q = \frac{1}{2}((\nabla \cdot \boldsymbol{u})^2 - \nabla \boldsymbol{u} : \nabla \cdot \boldsymbol{u}^{\boldsymbol{T}}) \tag{3.1}$$

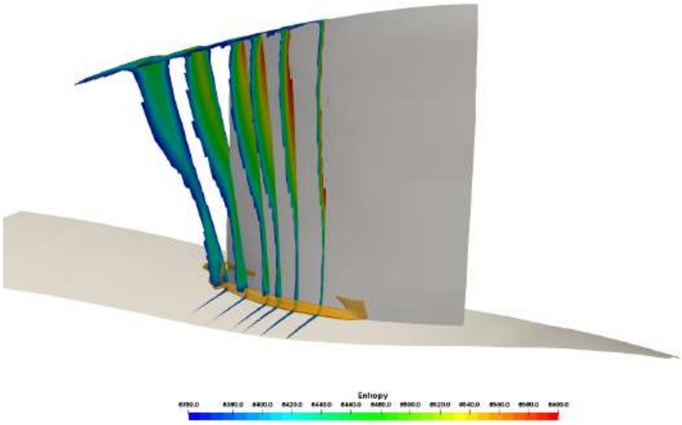

Figure 3.10: *Entropy contours visualising the rotor losses overlaid with an iso-surface of Q-criterion visualising the hub vortex.*

Chapter 4

NASA Rotor 37 with Endwall Contouring

In a conventional aero-engine compressor, with an increase in stage loading, the flow field within flow passage becomes more and more complicated. In order to maintain a wide operating range, the low aspect ratio gradually turns into a significant feature for the high-performance blade. With high blade loading, the streamwise adverse pressure gradient is exacerbated and the intensity of the secondary flow is extremely enhanced due to the increased circumferential pressure gradient. A geometry characteristic of low aspect ratio will contribute to reducing adverse pressure gradient. Nonetheless, the decrease in blade height inevitably enhances secondary loss induced by thicker endwall boundary layer and increasing three-dimensional effects.

The endwall contouring methodology includes axisymmetric profiling along axial direction and non-axisymmetric profiling along circumferential direction. In contrast to a case with flat walls, the size and strength of the secondary flow can be suppressed considerably with contoured endwalls. The concave endwall shape can unload the profile boundary layer while changing the original shock system from an oblique shock to a normal shock. Furthermore, the hub profile within the rotor blade flow path can have a significant influence on the performance while a contoured casing above the leading edge can have a notable impact in stall margin with slight decreases in efficiency and pressure ratio. Finally, endwall contouring can impact the flow not only near the endwall but also a considerable distance from the endwall along the span. As a matter of fact, the flow field is highly complex with respect to interactions between shock system and different vortexes in a high loaded cascade passage with a large flow turning. Therefore, the optimal axisymmetric endwall shape highly depends on the specific flow features.

In this chapter the results for the endwall contouring are presented in the form of two section,one for the hub cases and one the casing cases. For each section, the impact of different axisymmetric endwall shapes on the compressor rotor speed line including mass flow, pressure ratio and efficiency is discussed. Secondly, the impact of endwall shapes on the flow field is investigated both near stall and near peak efficiency conditions. Finally, the flow field detail of the endwall shape witht the best performance is analyzed and evaluated. All the modelled rotors, including the baseline NASA rotor 37 and the rotor with hub and casing perturbations identified in section 3 were simulated using the model shown in ??, which was successfully validated.

4.1 NASA Rotor 37 with Hub Contouring

In this section the hub contoured cases which are shown in Figure 4.1 will be analysed. In Figure 4.2 the efficiencies of all the investigated cases with a contoured hub line are presented. The case with the peak of the perturbation at 25% chord has greater peak efficiency than the baseline case but is less efficient near stall. The case with the peak of the perturbation at the 0% of the chord is the next best one, but overall has less efficiency. The hub perturbations improve the efficiency near the peak efficiency and choking conditions and decrease it near stall conditions. Specifically, 3.5% increase in choking massflow is achieved with the design that has its maximum depth at 25% chord. This behaviour is expected as the are of the passage is effectively increased. All the other cases are inferior to the baseline in terms of efficiency over the range of massflows from choke to stall at the design speed and is worthy to note that as the maximum depth is moved to the rear of the blade the deterioration in efficiency is increased.

(a) *0% Axial Positioning* **(b)** *25% Axial Positioning* **(c)** *50% Axial Positioning*

(d) *75% Axial Positioning* **(e)** *100% Axial Positioning*

Figure 4.1: *Investigated geometries with hub contouring.*

In Figure 4.3 the pressure ratios of all the investigated cases with a contoured hub line are presented. The case with the peak of the perturbation at 25% chord has also greater pressure ratio over the whole range of massflows at the design speed and as mentioned before higher peak efficiency. On the other hand the case with the peak

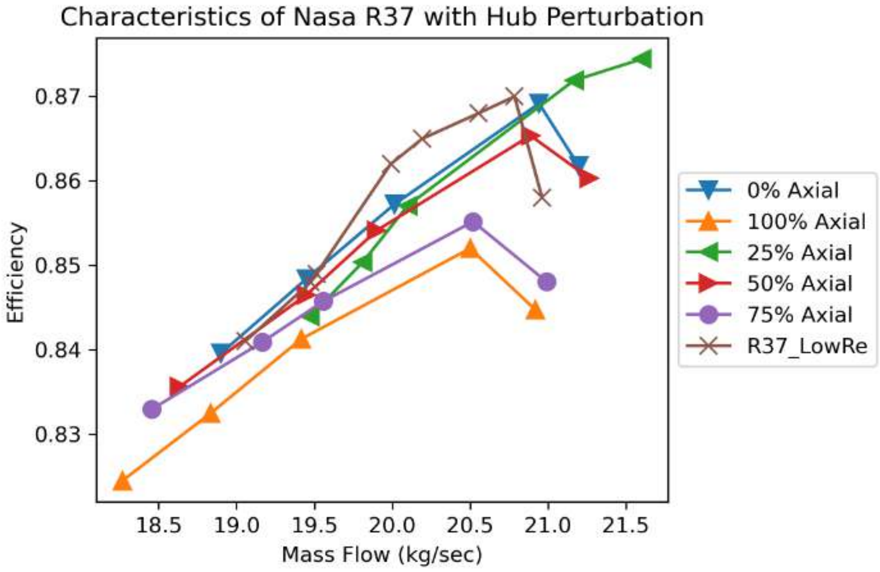

Figure 4.2: *Efficiency characteristics of the rotor 37 baseline and the hub contoured cases at design speed*

at 0% chord has similar pressure ratio with the baseline case. In particular, near peak efficiency its pressure ratio is higher than the baseline but near stall is lower, with a lower efficiency across these conditions. The case with the peak at 50% chord has the greatest pressure ratios overall, even when compared with the baseline and 25% chord, with the price of a lower efficiency though.

Overall the effectiveness on performance of the contouring on the hub line increases when the maximum depth is close to the passage shock location. In particular the cases with perturbations at 0%,25% and 50% chord are the most effective whereas the 75% and 100% have decreased the rotors performance both in terms of efficiency and pressure ratio. A possible explanation would be that the throat of the passage is effectively moved downstream, and at the same time the effective area of the throat is increased, that is to say that the choke mass flow is increased and at the same time the shock strength is increased. The shock is strengthened as more camber is acting on the flow until the throat, but the strength of the shock is not enough to severely separate the boundary layer, leading to a bigger pressure ratio and simultaneously an increased efficiency. This effect takes place mainly for the cases that have the perturbation upstream or near the passage shock location such as the 0%, 25% and 50% cases and not the 75% and 100% that have the perturbation downstream of the shock.

In order to deduct conclusion about the effect that axial location of the peak of the hub contouring perturbation has on the rotor's performance, the average and peak performance of each case are ploted in Figures 4.4a and 4.4b. In particular Figure 4.4a shows the efficiency and the pressure ratio of each case averaged across the

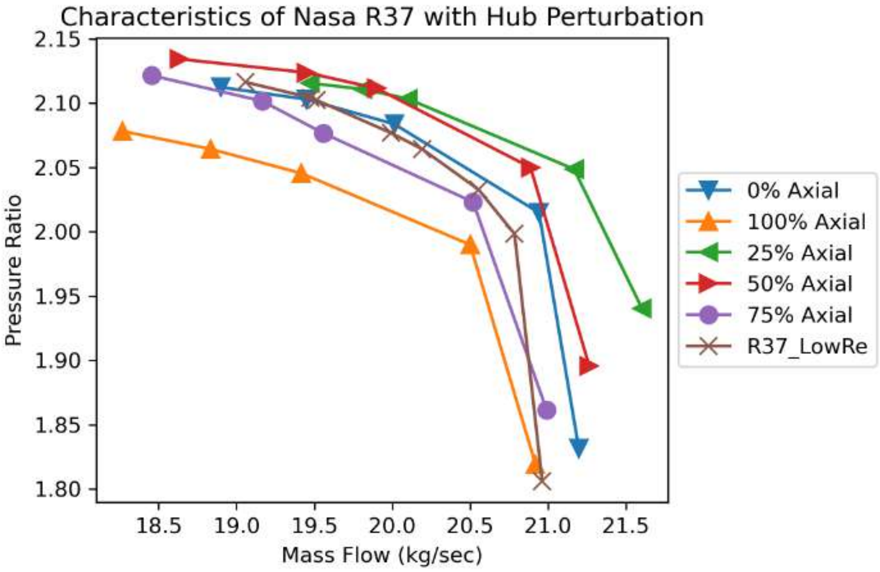

Figure 4.3: *Pressure ratio characteristics of the rotor 37 baseline and the hub contoured cases at design speed.*

range of massflow at the design speed, whereas as Figure 4.4b shows the maximum efficiency and pressure ratio that was produced by each case. As far as the average performance is concerned, the axial placement of the perturbation at 25% of the chord of the blade leads to both an increase in the average efficiency and the average pressure ratio, whereas the 50% case offers an equivalent improvement in pressure ratio but a reduction in efficiency. None of the other cases offers an improvement in both these metrics simultaneously. As far as peak performance is concerned, the 25% offers an improvement in peak efficiency, whereas the 50% and 75% cases offers an improvement in peak pressure ratio.

In terms of operability, Figure 4.5 shows the differences in stall and choke margin that the contoured cases have compared to the baseline rotor 37. For the 0% and 25% cases that are upstream the shock created a trade of choke and stall margin. Specifically the 0% case has an increased stall margin but a decreased choke margin, whereas for the 25% case the effect is the opposite with a significant decrease in stall margin. Moreover, the 50% case has an increase in both stall and choke margin, a trend which continues for the 75% and 100% case.

In Figures 4.6 and 4.7, a circumferential view of the wake of the rotor near peak efficiency and near stall at design speed for all the cases with hub contouring are presented. Specifically, the entropy distribution is shown at 4.5 cm and 10 cm downstream the rotor's leading edge, corresponding to station 3 and 4a accordingly in Figure 1.13. In an adiabatic flow, as modeled here, the entropy creation is due exclusively to the aerodynamic irreversibilities; therefore, Figures 4.6 and 4.7 can be used to identify the regions which are sources of aerodynamic losses. As shown in

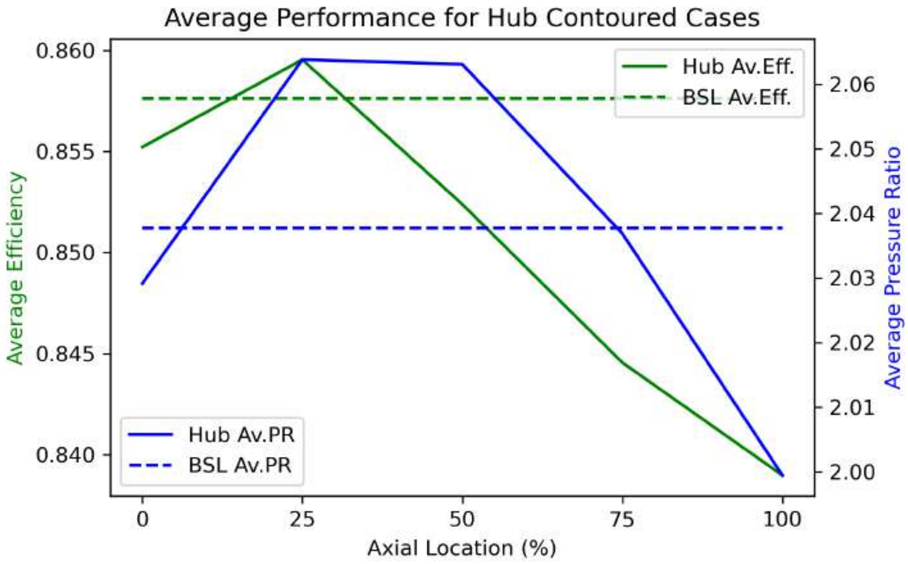

(a) *Average Performance*

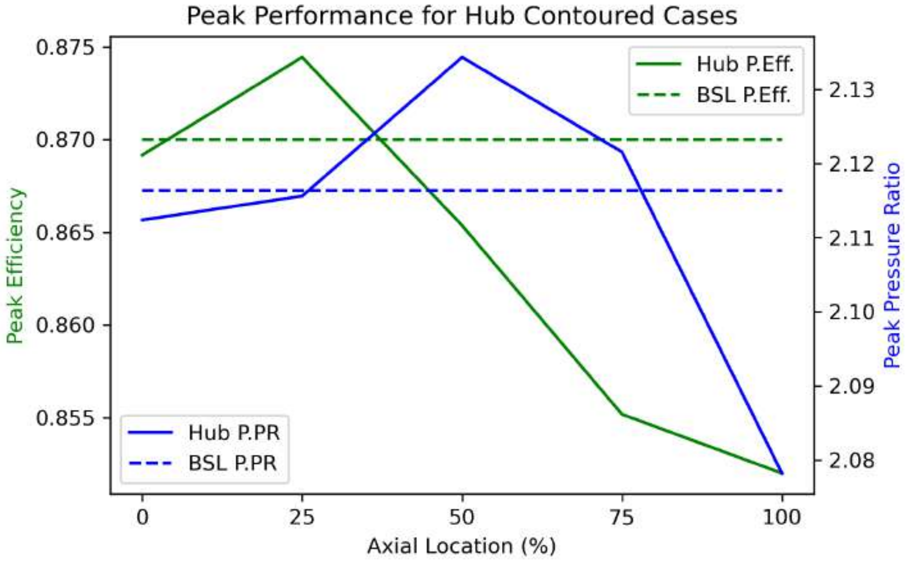

(b) *Peak Performance*

Figure 4.4: *Comparison of the average and peak performance (efficiency & pressure ratio) between the investigated hub contoured cases and the baseline rotor 37.*

Figure 4.6b just after the trailing edge of the rotor, compared to the baseline rotor in Figure 4.6a, the 0% case has reduced losses near the higher span areas creating a thinner wake at about 50% span but has increased the losses near the hub, near the peak efficiency conditions.

A similar effect can be detected when comparing Figures 4.7a and 4.7b, where the

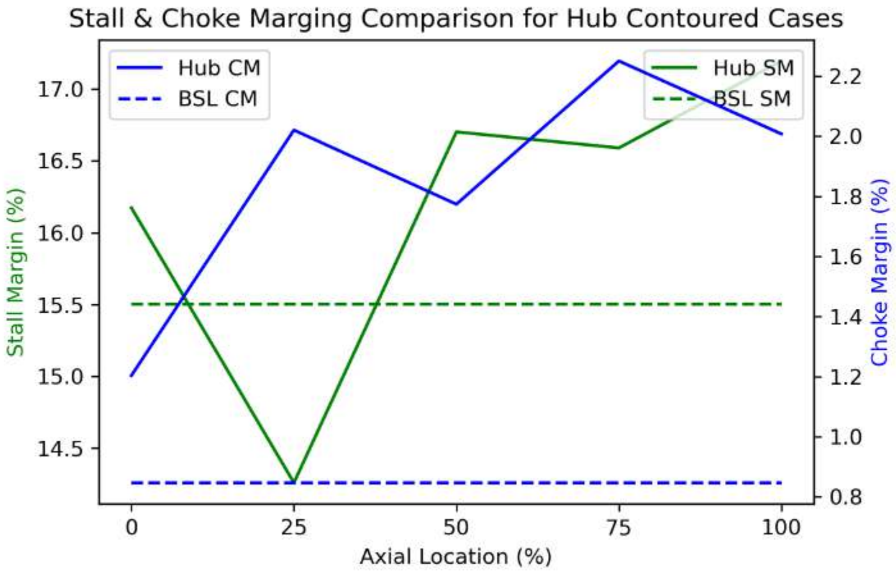

Figure 4.5: *Comparison of the stall and choke margins between the investigated hub contoured cases and the baseline rotor 37.*

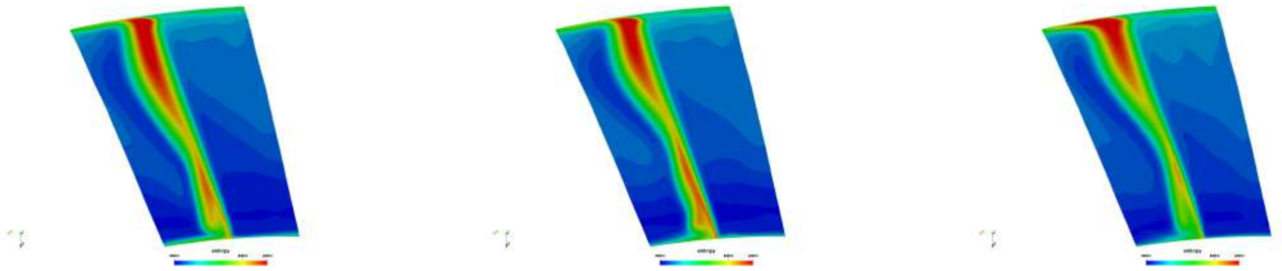

(a) *Baseline* **(b)** *0% Axial Positioning* **(c)** *25% Axial Positioning*

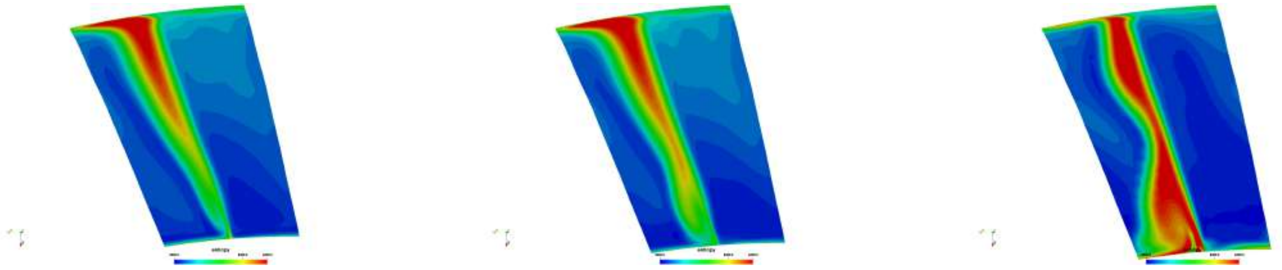

(d) *50% Axial Positioning* **(e)** *75% Axial Positioning* **(f)** *100% Axial Positioning*

Figure 4.6: *Comparison of entropy flow field at 4.5 cm downstream the rotor's leading edge between the baseline rotor 37 and the hub contoured cases near peak efficiency.*

loss core near the hub is thickened for the case with the hub perturbation and the higher span losses are slightly reduced. After averaging these changes the final result for the efficiency of the rotor with the peak of the perturbation at 0% chord, as

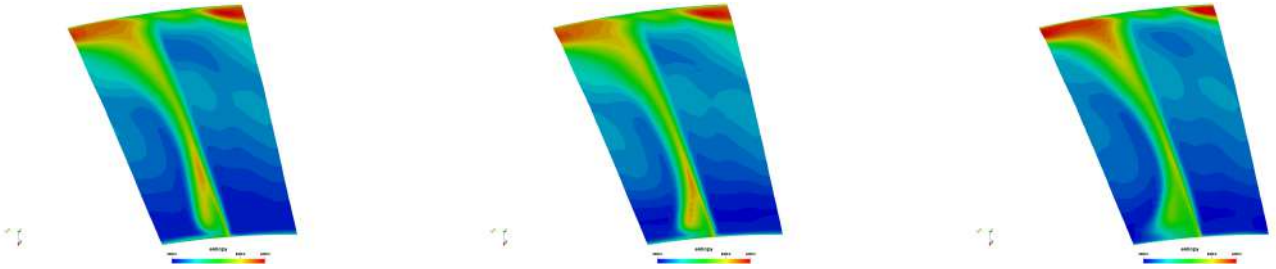

(a) *Baseline* **(b)** *0% Axial Positioning* **(c)** *25% Axial Positioning*

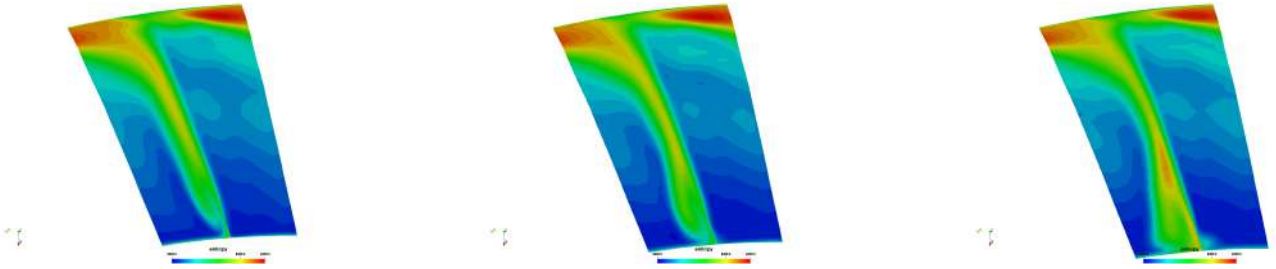

(d) *50% Axial Positioning* **(e)** *75% Axial Positioning* **(f)** *100% Axial Positioning*

Figure 4.7: *Comparison of entropy flow field at 7 cm downstream the rotor's leading edge between the baseline rotor 37 and the hub contoured cases near stall.*

previously discussed, is slightly worse for all the range of massflows at design speed. For the case with a the peak of the perturbation placed at 25% chord, as shown in Figures 4.6c and 4.7c the blade wake near the hub has a significant decrease in entropy and at the same time the entropy at the higher span area is reduced near peak efficiency. This effect is much less evident near the stall conditions, where the loss near the hub for the contoured case has decreased in magnitude but has become wider and the losses near the higher span areas are increased compared to the baseline rotor 37. This leads to the effect that was shown in the efficiency characteristics comparison, where the 25% case has greater peak efficiency but less efficiency near stall. Moreover, as shown in Figures 4.6d and 4.7d the 50% case has a redistribution of losses compared to the baseline, that is to say the loss near the hub is reduced but the losses near the higher span area are increased near peak efficiency. This is also evident near stall, where the high entropy region in the blade wake from 10% - 30% span migrates to 50% - 60% span. For the remaining cases with the peaks of the perturbation at 75% and 100% chord the wake of the blades are thicker with significantly increased losses near the peak efficiency conditions which is in accordance to the compressor maps shown previously. Near stall conditions they remain in a worse state but relatively closer to the efficiency of the baseline rotor.

In Figures 4.8 and 4.9 a view of the tip leakage vortex of the rotor near peak efficiency and near stall at design speed for all the cases with hub contouring is presented. Specifically, a contour of Q-criterion is shown, coloured by Mach number near the tip region. Comparing Figures 4.8a and 4.8b it is apparent that the effect of the hub contouring at 0% chord of the blade did not have any significant effect on the structure of the leakage vortex near peak efficiency. Near stall, the structure of the tip leakage vortex has changed compared to the near peak efficiency conditions. The primary vortex, which is shed from the leading edge of the blade, had merged with the secondary vortex, which is shed downstream the leading edge, for the baseline case as shown in The same is true for Figure4.9a. The same behaviour at peak efficiency of the 0% hub contour can be seen in Figure 4.9b where its effect on the tip vortex is negligible, which is in accordance with the wake entropy distribution shown previously. The 25% case is shown in Figure 4.8c near peak efficiency conditions, where it can be seen that the angle remains the same for both the primary and secondary tip leakage vortices, but the starting point of the secondary core has moved upstream. In Figure 4.9c there is greater differentiation between the baseline and the 25% case near stall. In particular, for the 25% case the primary and secondary vortex are not merged, due to the fact that the starting point of the secondary core has moved downstream. For the 50% case shown in Figure 4.8d near peak efficiency, the angle of the vortices remains the same, but the secondary vortex moves further upstream and comes closer to the primary core compared both to the baseline and 25% case. Near stall, as shown in Figure 4.9d, the vortex structure is similar to the baseline case with the two vortices merging even closer to the leading edge of the blade compared to the baseline rotor 37. For the 75% case the vortices move further upstream for both near peak efficiency and near stall conditions, where in the later they merge close to the leading edge of the blade. Finally, for the 100% case near the peak efficiency conditions, the secondary vortex breaks down, while near stall the vortex behaviour is similar to the 75% case.

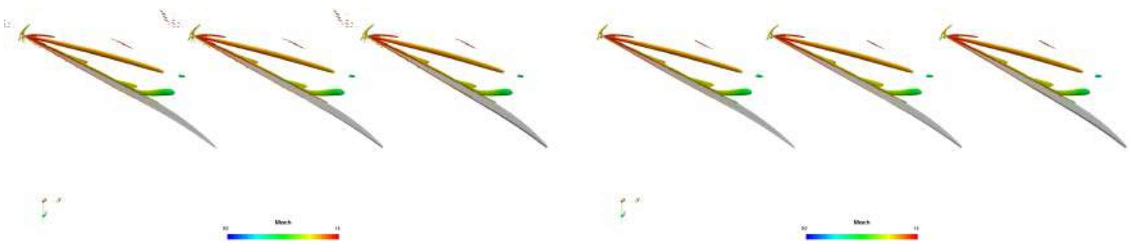

(a) *Baseline* **(b)** *0% Axial Positioning*

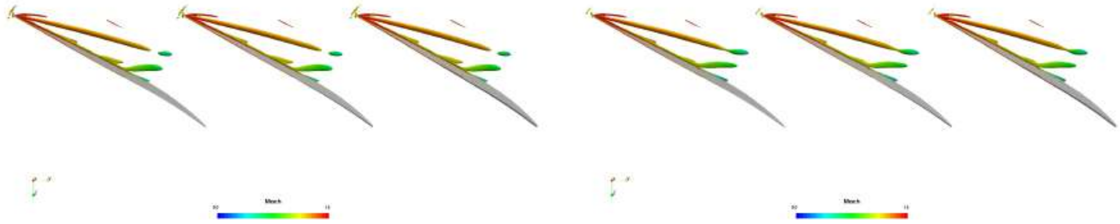

(c) *25% Axial Positioning* **(d)** *50% Axial Positioning*

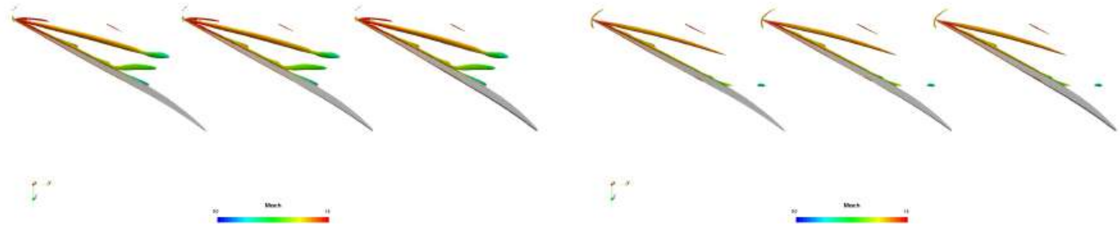

(e) *75% Axial Positioning* **(f)** *100% Axial Positioning*

Figure 4.8: *Comparison of Q criterion contours colored by mach number between the baseline rotor 37 and the hub contoured cases near peak efficiency.*

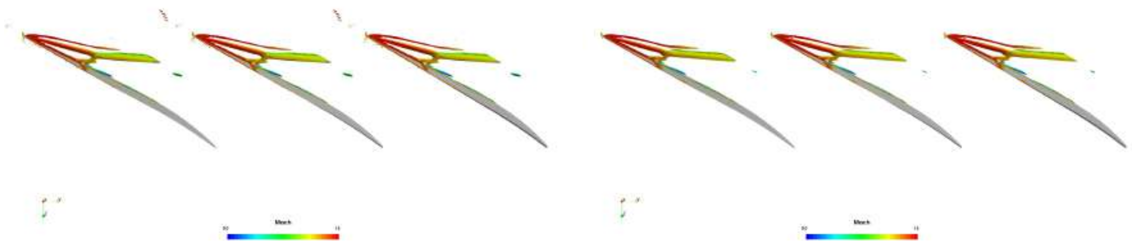

(a) *Baseline* **(b)** *0% Axial Positioning*

(c) *25% Axial Positioning* **(d)** *50% Axial Positioning*

(e) *75% Axial Positioning* **(f)** *100% Axial Positioning*

Figure 4.9: *Comparison of Q criterion contours colored by mach number between the baseline rotor 37 and the hub contoured cases near stall.*

Figures 4.10 and 4.11 show contours of the predicted static pressure of the blade suction surfaces, with the shaded regions indicating areas of zero axial velocity. The 0% case is shown in Figures 4.10b and 4.11b and the effect of the hub perturbation in the pressure distribution of the blade is evident for both plots. Specifically, the pressure distribution over the blade has changed for the root of the blade, with the leading edge near the hub being significantly more loaded and the shock being skewed compared to the baseline rotor as shown by the concentrated pressure contour lines and the rapid change in the pressure field. The pressure contours of the baseline case near the hub are skewed backwards due to the horseshoe vortex that is shed near the hub corner, instead in the 0% case this effect is reduced for the front part of the blade and is only apparent near the trailing edge. The zero axial velocity bubble is reduced mainly by the new position of the shock indicating a reduction in the separation of the blade. The 25% case shown in Figures 4.10c and 4.11c has similar effects on the flow, but the front part of the blade is less loaded than the 0% case and the zero axial velocity bubble is reduced. At the same time the horseshoe vortex effect is more evident in the pressure contours for both conditions and specifically near stall conditions the vortex is redirected upwards. The 50% case shown in Figures 4.10d and 4.11d has increased suction near the hub compared to the baseline case, but less than both the 0% and 25%. At the same time the zero axial velocity bubble behind the shock extends all across the whole passage unlike the previous cases where it was covering a part of the blade's span, but has decreased near the lower span region of the trailing edge. The 75% and 100% cases do not have a significant effect on the pressure field upstream of the shock and as a result the pressure distribution in the front part of the blade is similar to that of the baseline. Moreover, the zero axial velocity shade also extends across the full span near peak efficiency and at the same time there the hub corner separation near the trailing edge is increased for both conditions.

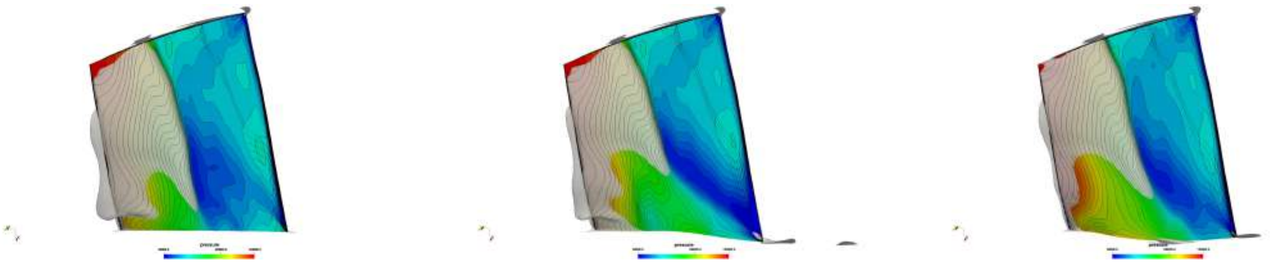

(a) *Baseline* **(b)** *0% Axial Positioning* **(c)** *25% Axial Positioning*

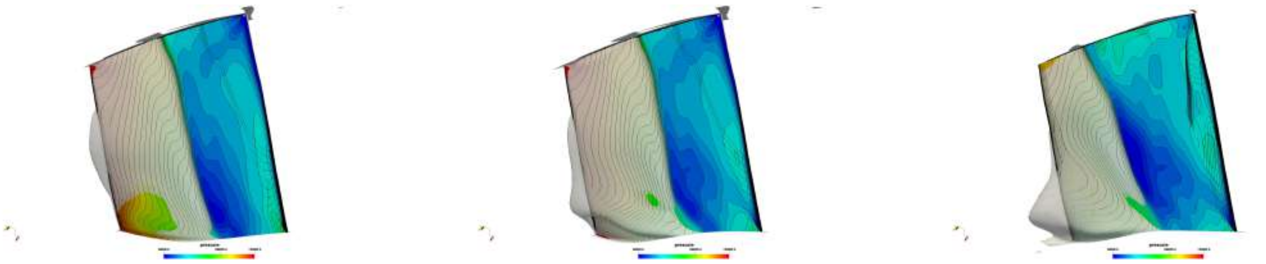

(d) *50% Axial Positioning* **(e)** *75% Axial Positioning* **(f)** *100% Axial Positioning*

Figure 4.10: *Comparison of static pressure contours overlayed with 0 axial velocity contour between the baseline rotor 37 and the hub contoured cases near peak efficiency.*

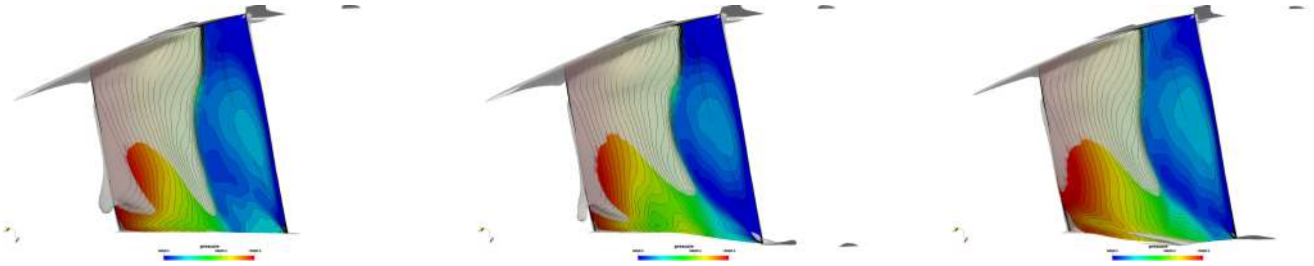

(a) *Baseline* **(b)** *0% Axial Positioning* **(c)** *25% Axial Positioning*

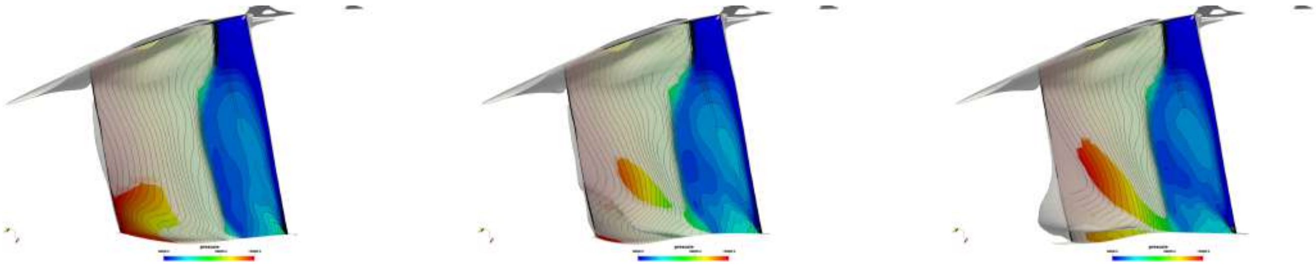

(d) *50% Axial Positioning* **(e)** *75% Axial Positioning* **(f)** *100% Axial Positioning*

Figure 4.11: *Comparison of static pressure contours overlayed with 0 axial velocity contour between the baseline rotor 37 and the hub contoured cases near stall.*

4.2 NASA Rotor 37 with Casing Contouring

In this section the casing contoured which are shown in Figure 4.12 will be analysed. In Figure 4.13 the efficiency of all the investigated cases with a contoured hub line is presented. The casing contouring did not improve the rotor performance in terms of efficiency. The best of the contoured cases in terms of peak efficiency are the case with the peak of the perturbation at 100% , 75% and 50%, but all of these cases have reduced efficiency both at peak, choke and stall conditions compared to the baseline geometry. The 25% case has less peak efficiency than the baseline rotor, but near stall this difference is reduced. Finally, the 0% case has also reduced efficiency over the whole range of investigated flow conditions.

(a) *0% Axial Positioning* **(b)** *25% Axial Positioning* **(c)** *50% Axial Positioning*

(d) *75% Axial Positioning* **(e)** *100% Axial Positioning*

Figure 4.12: *Investigated geometries with casing contouring.*

In Figure 4.14 the pressure ratios of all the investigated cases with a contoured casing line are presented. The case with the peak of the perturbation at 100% chord has greater pressure ratio over the whole range of massflows at design speed. The 75% case has also improved pressure ratio compared to the baseline case at all the investigated points except near stall conditions. The 50% and 25% cases have reduced pressure ratios near stall conditions but similar to the baseline near their peak efficiencies.

Overall the effectiveness on performance of the contouring on the casing line increases when the maximum depth is close to the trailing edge of the blade. In particular the cases with perturbations at 75% and 100% chord are the most effective whereas the 0%, 25% and 50% have decreased the rotors performance both in terms of efficiency and pressure ratio. A possible explanation for the increased pressure ratio of the cases that have an increased area near the trailing edge is the fact that the diffusion ratio increases, but this comes with the cost of extra losses.

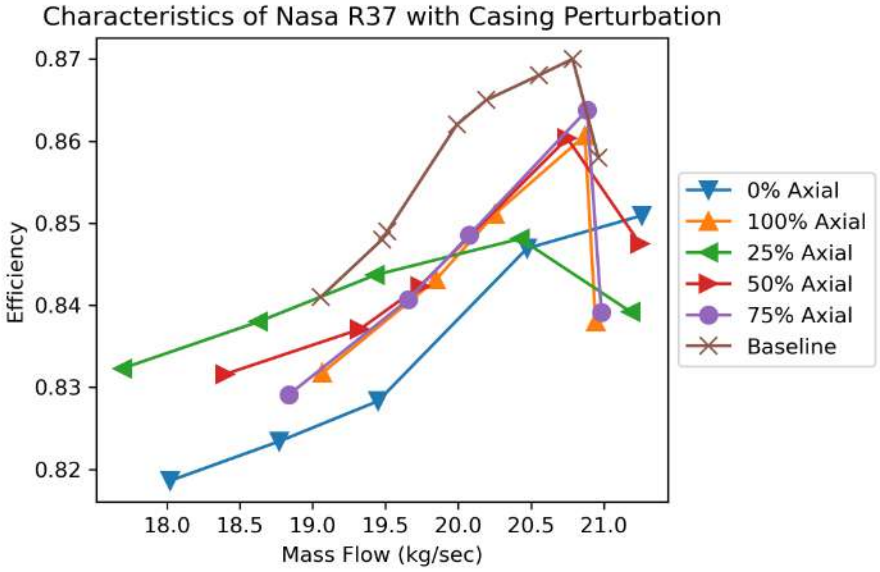

Figure 4.13: *Efficiency characteristics of the rotor 37 baseline and the casing contoured cases at design speed*

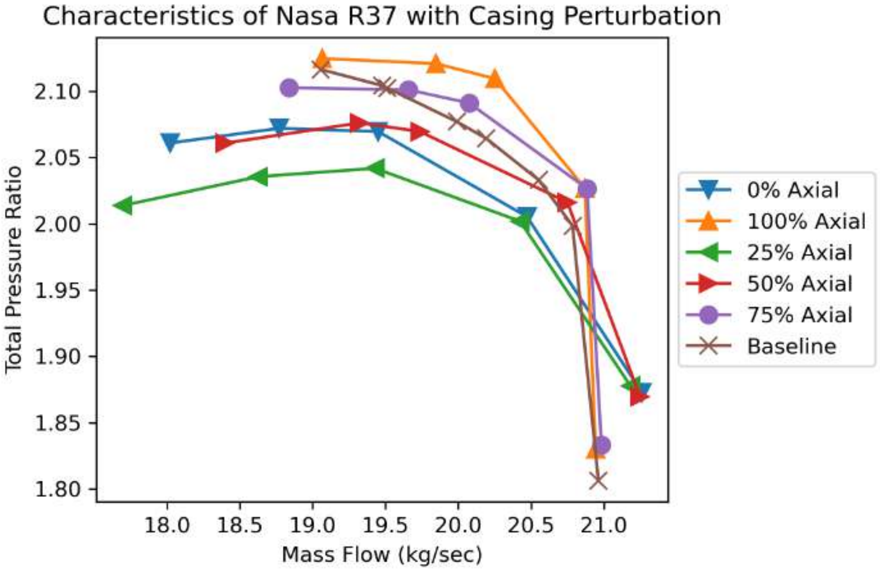

Figure 4.14: *Pressure ratio characteristics of the rotor 37 baseline and the casing contoured cases at design speed.*

In order to deduct conclusion about the effect that axial location of the peak of the casing contouring perturbation has on the rotor's performance, the average and peak performance of each case are ploted in Figures 4.15a and 4.15b, similarly to the previous section. In particular Figure 4.15a shows the efficiency and the pressure ratio of each case averaged across the range of massflow at the design speed, whereas as Figure 4.15b shows the maximum efficiency and pressure ratio that was produced by each case. As far as the average performance is concerned, none of the casing perturbed cases produces an simultaneous improvement in both the average efficiency and pressure ratio. In particular, the 100% case produces an improvement in average pressure ratio but with the cost of efficiency, while the 75% case has the highest average efficiency of all the casing perturbations, but lower than the baseline rotor. In terms of the peak performance again the only improvement is found in the peak pressure ratio of the 100% case, while the 75% case has the highest peak efficiency for the perturbed cases, but again lower than the baseline.

As far as the operability is concerned, Figure 4.16 shows the differences in stall and choke margin that the contoured cases have compared to the baseline rotor 37. The 0% and 25% cases that are upstream the shock and near the leading edge at the tip of the blade had increased both the stall and choke margins. Specifically the 0% case has the highest margins compared to the baseline and the other cases with the contoured casing. The 25% has also increased margins both for stall and choke, whereas from the 50% case and on, all the contoured cases have a stall margin deficit compared to the baseline case. Also a similar effect takes place for the choke margin on the 75% case and on, having a deficit.

In Figures 4.17 and 4.18 a circumferential view of the wake of the rotor near peak efficiency and near stall at design speed for all the cases with casing contouring are presented. Similarly to the previous section, the entropy distribution is shown at 4.5 cm and 10 cm downstream the rotor's leading edge, corresponding to station 3 and 4a accordingly in Figure 1.13. As shown in Figure 4.17b just after the trailing edge of the rotor, compared to the baseline rotor in Figure 4.17a, the 0% case has increased losses near the higher span areas both in the main flow and at the wake of the blade, which is also thicker for the perturbed case, but has similar losses near the hub region, near the peak efficiency conditions. When comparing Figures 4.7a and 4.18b, it is evident that the loss core originating from the tip leakage near the casing is thickened for the case with the casing perturbation and the higher span losses are significantly increased. After averaging these changes the final result for the efficiency of the rotor with the peak of the perturbation at 0% chord, as previously discussed, is worse for all the range of massflows at design speed. For the case with a the peak of the perturbation placed at 25% chord, as shown in Figures 4.17b and 4.18b the blade wake near the casing has a significant increase in entropy in the main flow and at the same time the blade wake is thickened and skewed, near peak efficiency. This effect is less evident near the stall conditions, where the loss of the main flow near the casing for the contoured case has decreased in magnitude but its wake has become wider compared to the baseline rotor 37. This leads to the effect that was shown in the efficiency characteristics comparison, where the 25% case has reduced peak efficiency but near stall its efficiency is similar to the baseline rotor 37. Moreover, as shown in Figures 4.17d and 4.18d the 50% case has increased entropy in the blade wake at high span regions near peak efficiency. Near stall, the same is true but except for the blade wake, the main part of the flow has increased entropy too.

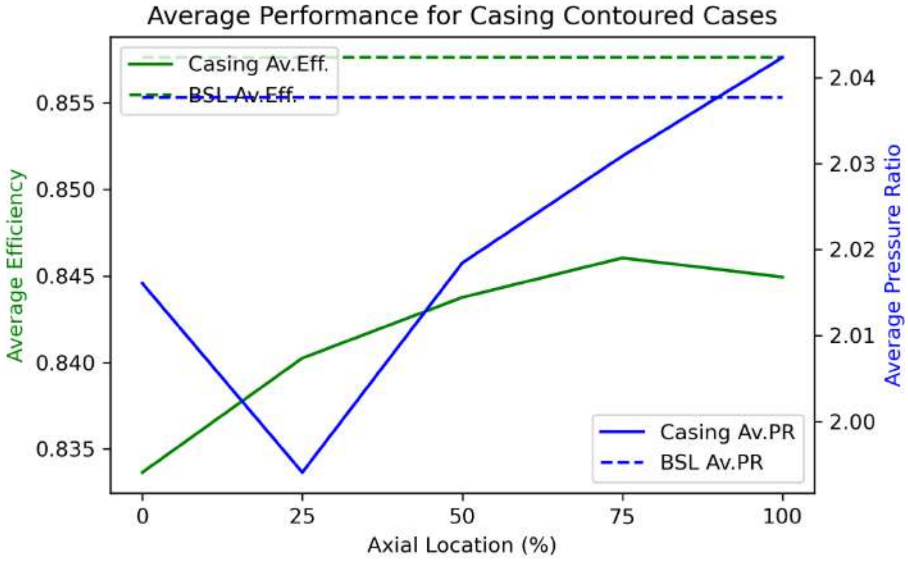

(a) *Average Performance*

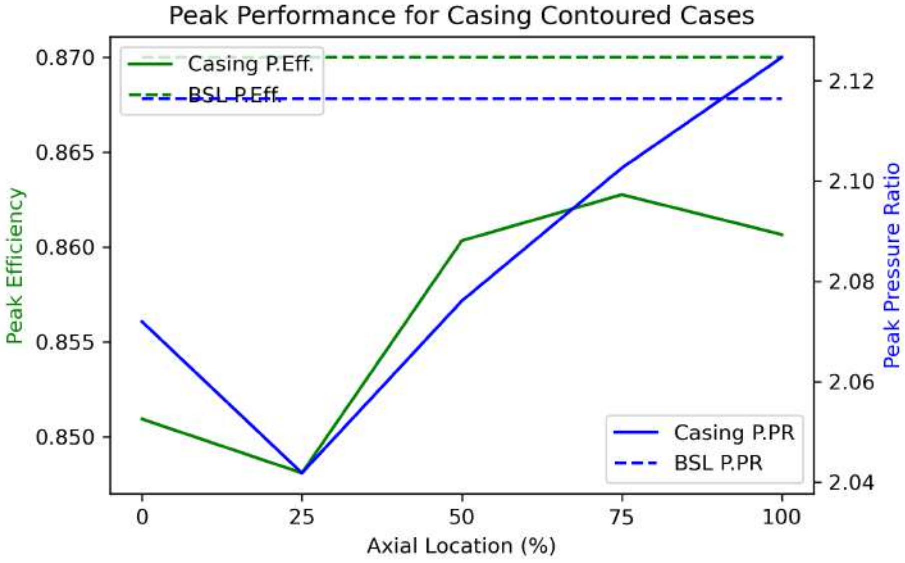

(b) *Peak Performance*

Figure 4.15: *Comparison of the average performance (efficiency & pressure ratio) between the investigated hub contoured cases and the baseline rotor 37.*

For the remaining cases with the peaks of the perturbation at 75% and 100% chord the wake of the blades are thicker with significantly increased losses both near the peak efficiency and stall conditions which is in accordance to the compressor maps shown previously. It is worthy of noting, that the majority of the cases have skewed the wake of the blade in the high span regions in a counter-clockwise direction.

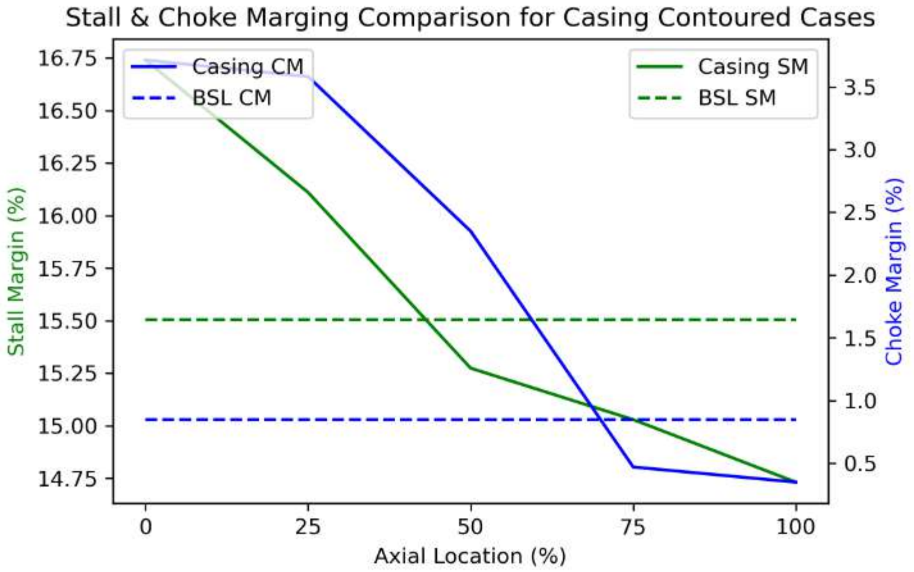

Figure 4.16: *Comparison of the stall and choke margins between the investigated casing contoured cases and the baseline rotor 37.*

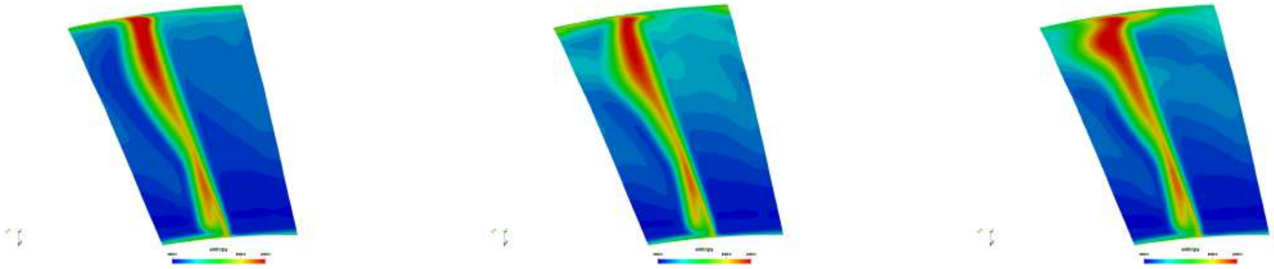

(a) *Baseline* **(b)** *0% Axial Positioning* **(c)** *25% Axial Positioning*

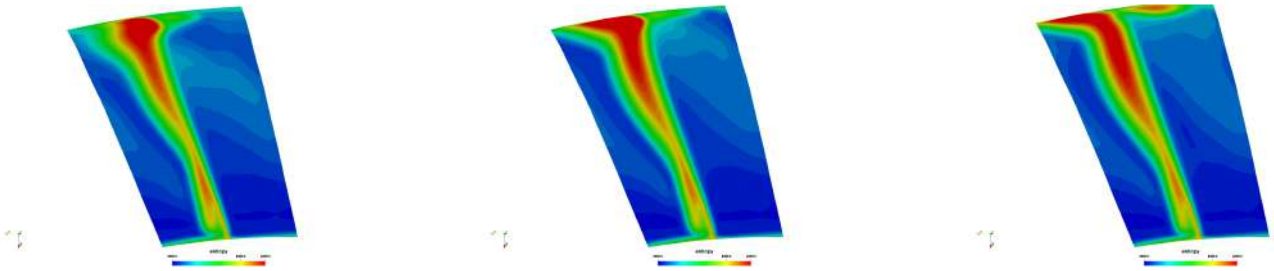

(d) *50% Axial Positioning* **(e)** *75% Axial Positioning* **(f)** *100% Axial Positioning*

Figure 4.17: *Comparison of entropy flow field at 4.5 cm downstream the rotor's leading edge between the baseline rotor 37 and the casing contoured cases near peak efficiency.*

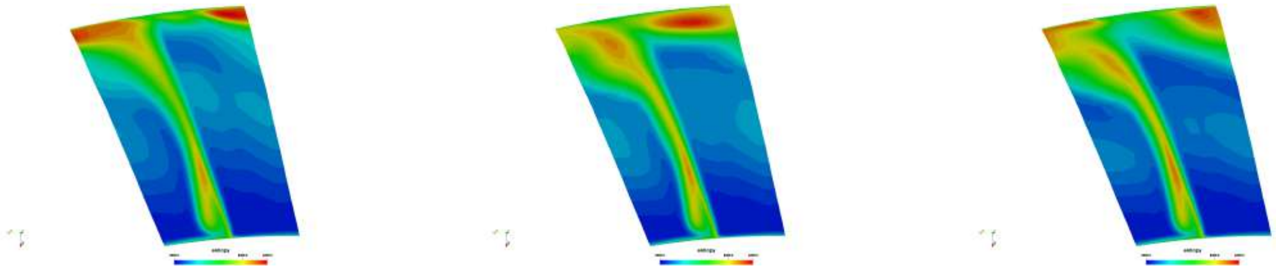

(a) *Baseline* **(b)** *0% Axial Positioning* **(c)** *25% Axial Positioning*

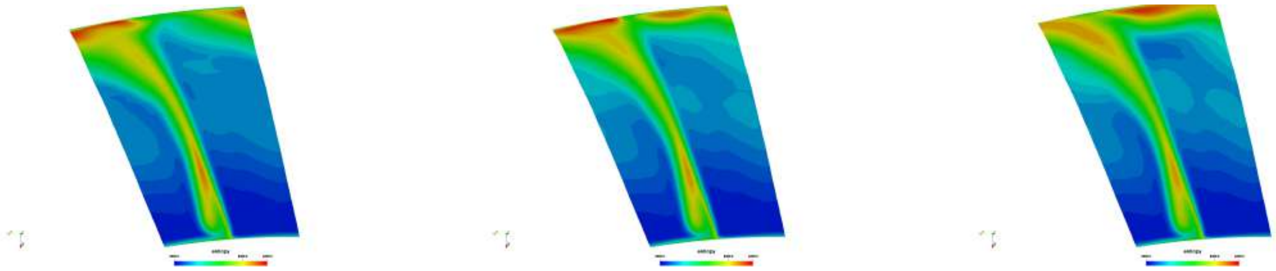

(d) *50% Axial Positioning* **(e)** *75% Axial Positioning* **(f)** *100% Axial Positioning*

Figure 4.18: *Comparison of entropy flow field at 7 cm downstream the rotor's leading edge between the baseline rotor 37 and the casing contoured cases near stall.*

In Figures 4.19 and 4.20 a view of the tip leakage vortex (TLV) of the rotor near peak efficiency and near stall at design speed for all the cases with casing contouring is presented. Similarly to the previous section, a contour of Q-criterion is shown, coloured by Mach number near the tip region.

Comparing Figures 4.20a and 4.20b it can be derived that the hub contouring at 0% chord of the blade near peak efficiency slightly affects the angle of the primary vortex, bringing it closer to the suction side of the blade and the starting location of the secondary tip leakage vortex which is moved upstream. Near stall the structure of the vortex is significantly altered from the baseline two merged vortices that propagate inside the passage to a single vortex that spilled out of the passage. The 25% and 50% cases shown in figures 4.17c and 4.17d near peak efficiency have strong similarities and resemble the vortex structure of the baseline case when operating near stall. In particular, the primary and secondary tip leakage vortex have merged near the leading edge of the blade forming a Y shape that remains inside the passage. In Figures 4.18c and 4.18d these cases are shown near the stall conditions. In these conditions, the vortices have almost broke down for the 25% case and for the 50% are spilled outside of the passage with a high angle relative to the flow. The 75% case is shown in Figures 4.17e and 4.18e near peak efficiency and near stall accordingly. In particular, near peak efficiency the vortex structure is similar to the baseline rotor except for the strength and the starting point of the secondary vortex which is increased and moved upstream respectively. Near stall conditions the similarity with the baseline case is increased, as far as the tip leakage vortex is concerned. Finally, the 100% case shown in Figures 4.17f and 4.18f has similar primary vortex to the baseline near peak efficiency but the secondary vortex has increased strength, whereas near stall the structure is identical to the baseline.

Figures 4.21 and 4.22 show contours of the predicted static pressure of the blade suction surfaces, with the shaded regions indicating areas of zero axial velocity, similarly to the plots shown in the previous section for the hub contouring. The 0% case is shown in Figures 4.32b and 4.33b and the hub perturbation affects the pressure distribution of the blade in both conditions. Specifically, the pressure distribution over the blade has changed for the tip region, with the leading edge near the casing being significantly more loaded and the shock being skewed compared to the baseline rotor as shown by the concentrated pressure contour lines and the rapid change in the pressure field. The root region of the blade is almost unaffected near peak efficiency and the axial velocity shade is moved upstream for the high span region of the blade. following the shock pattern. Near stall conditions, the increased tip loading leads to the tip leakage vortex structure mentioned before that is spilled out of the passage resulting to an increased zero axial velocity bubble. The 25% case shown in Figures 4.10c and 4.11c has similar effects on the flow, but the front part of the blade is less loaded than the 0% case but the zero axial velocity bubble is extends up to the casing of the blade. Similarly to the 0% case, near stall conditions the interaction with the tip leakage vortex leads to an increased zero axial velocity region compared to the baseline case. The 50% case has similar effects, but less

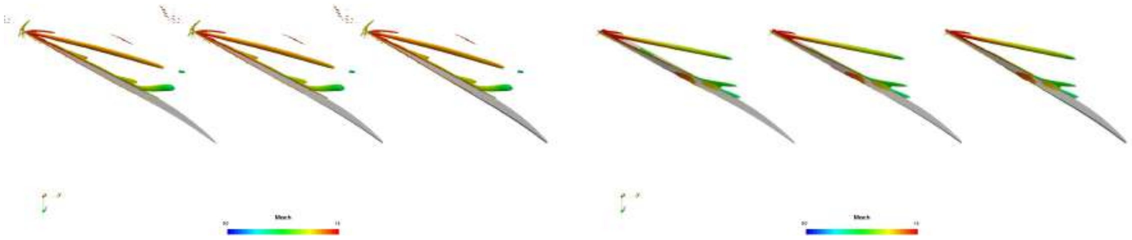

(a) *Baseline* **(b)** *0% Axial Positioning*

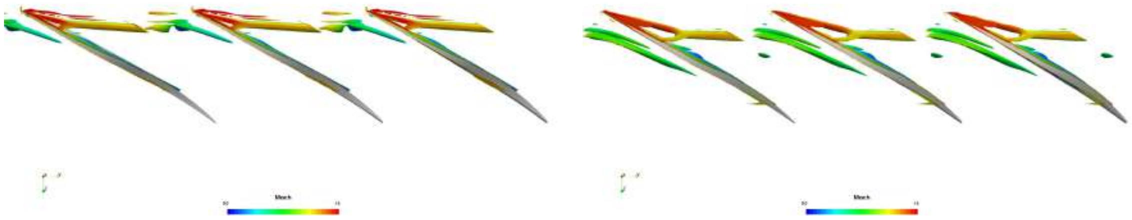

(c) *25% Axial Positioning* **(d)** *50% Axial Positioning*

(e) *75% Axial Positioning* **(f)** *100% Axial Positioning*

Figure 4.19: *Comparison of Q criterion contours colored by mach number between the baseline rotor 37 and the casing contoured cases near peak efficiency.*

severe for both conditions, having decreased loading near the tip region and moving the shock position downstream near the tip region compared to the 0% and 25% cases but still increased loading and upstream position compared with the baseline rotor respectively. Finally, the 75% and 100% have less pronounced effects too, moderately increasing the loading near the tip region and extending the zero axial velocity region up to the casing of the blade, indicating increased separation too.

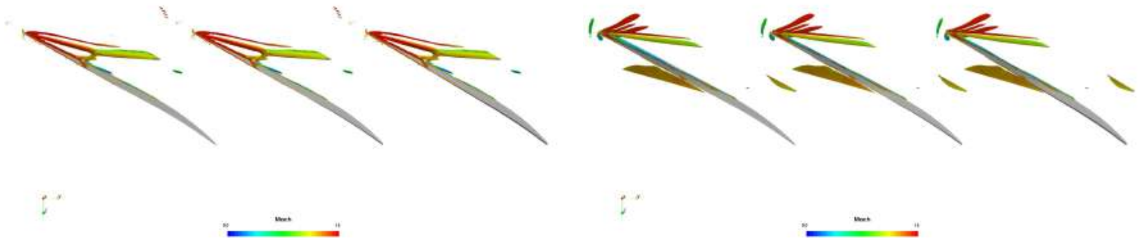

(a) *Baseline* **(b)** *0% Axial Positioning*

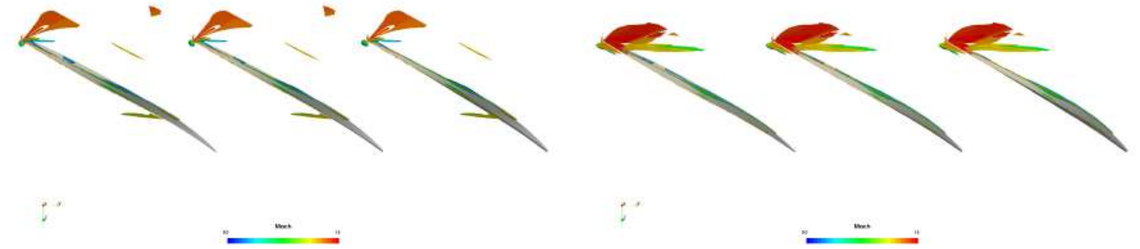

(c) *25% Axial Positioning* **(d)** *50% Axial Positioning*

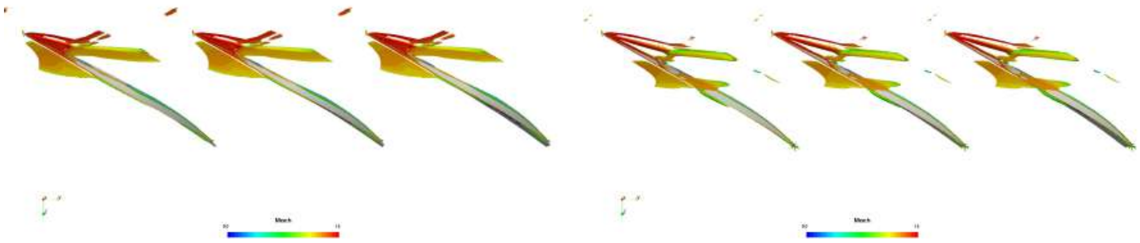

(e) *75% Axial Positioning* **(f)** *100% Axial Positioning*

Figure 4.20: *Comparison of Q criterion contours colored by mach number between the baseline rotor 37 and the casing contoured cases near stall.*

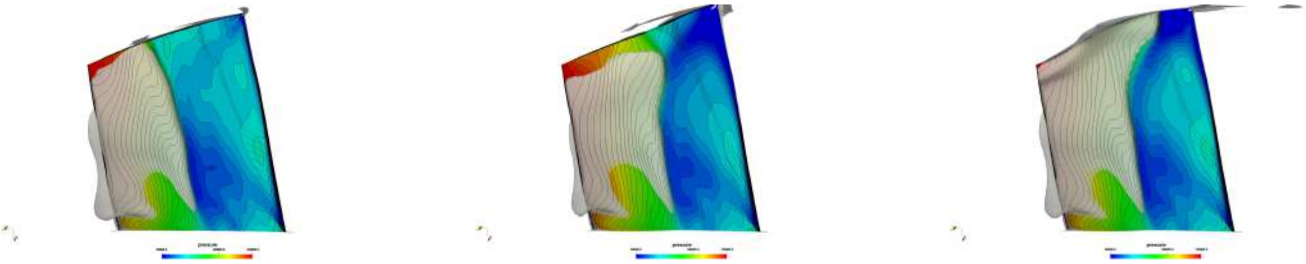

(a) *Baseline* **(b)** *0% Axial Positioning* **(c)** *25% Axial Positioning*

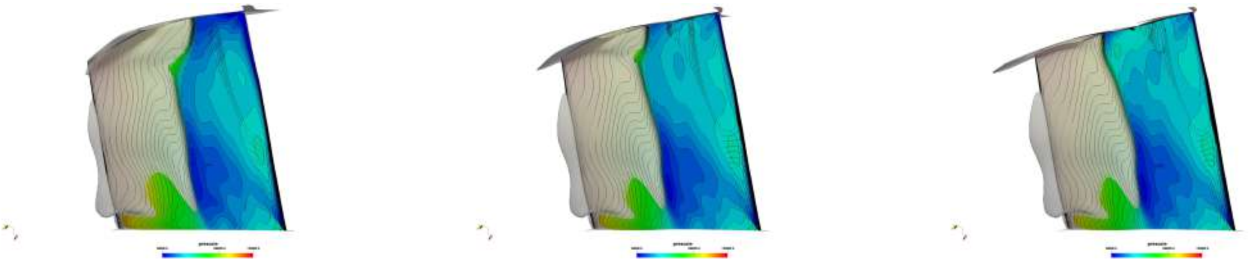

(d) *50% Axial Positioning* **(e)** *75% Axial Positioning* **(f)** *100% Axial Positioning*

Figure 4.21: *Comparison of static pressure contours overlayed with 0 axial velocity contour between the baseline rotor 37 and the casing contoured cases near peak efficiency.*

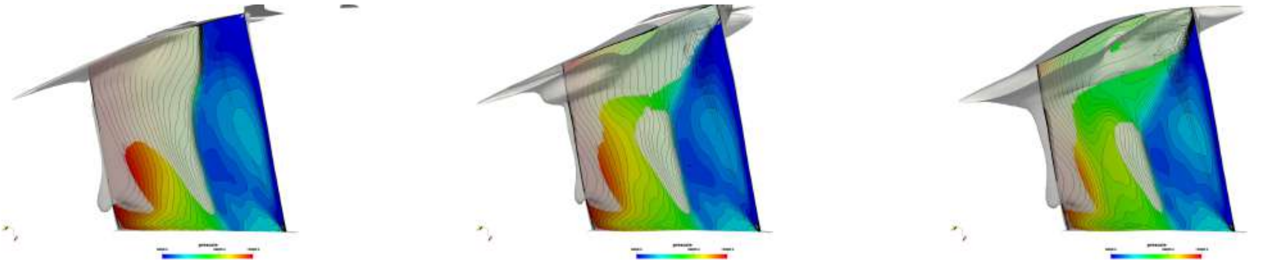

(a) *Baseline* **(b)** *0% Axial Positioning* **(c)** *25% Axial Positioning*

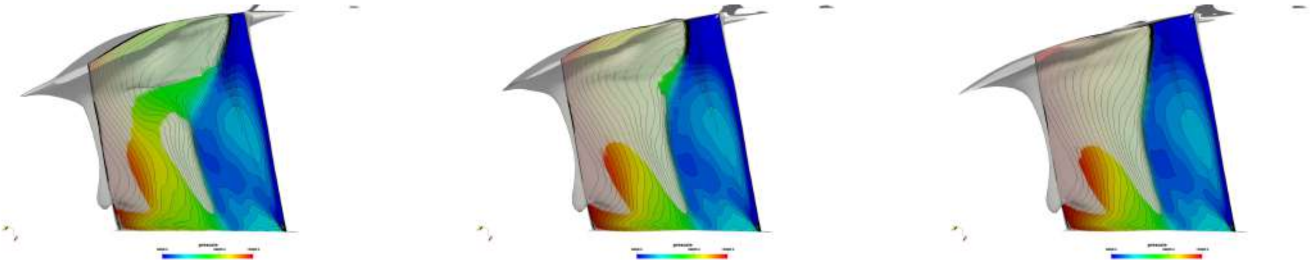

(d) *50% Axial Positioning* **(e)** *75% Axial Positioning* **(f)** *100% Axial Positioning*

Figure 4.22: *Comparison of static pressure contours overlayed with 0 axial velocity contour between the baseline rotor 37 and the casing contoured cases near stall.*

4.3 A combined case of NASA Rotor 37 Endwall Contouring

In this section a case with a combination of hub and casing contouring will be analysed. Figure 4.23 will be utilised in order to find which of the previously investigated cases can offer improvement in performance, operability or both and as a result could potential be investigated in a case simultaneously. Specifically, Figure 4.23 shows the peak total pressure ratio and the efficiency corresponding to that pressure ratio for all the cases at design speed. It is apparent that the 25% cases for both the hub and casing contouring can offer an improvement in efficiency at their peak total pressure ratio compared to the baseline case, with the hub contoured case maintaining the same peak pressure ratio whereas the casing contoured case has a reduced peak pressure ratio. On the other hand the 50% hub case offers an improvement in peak pressure ratio with a reduction in efficiency compared to the baseline case. Moreover Figure 4.23b shows the peak efficiency and the total pressure ratio corresponding to that efficiency for all the cases at design speed. It is evident that the 25% hub case can offer an increase in peak efficiency with a reduction in the pressure ratio compared to the baseline case, while the 50% hub case can offer an improvement in pressure ratio with a reduced peak efficiency. It is worth noting that from the casing contoured cases the 75% case has the highest peak efficiency and compared to the baseline case has an increased pressure ratio but lower efficiency.

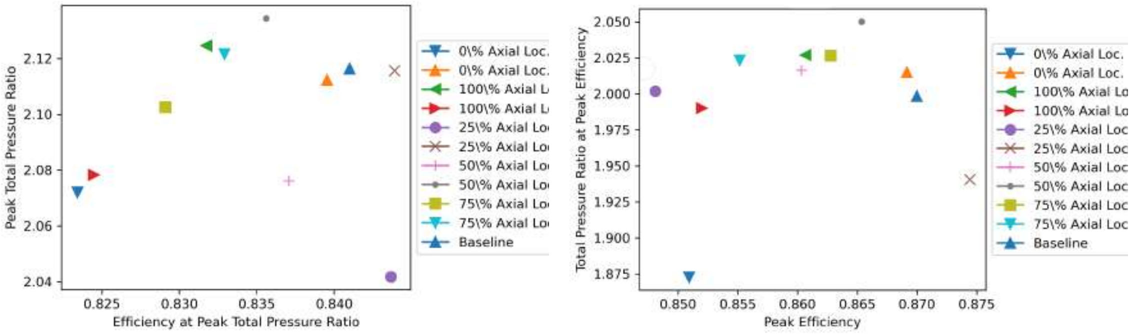

(a) *Combined representation for peak performance at peak total pressure ratio.*

(b) *Combined representation for peak performance at peak efficiency.*

Figure 4.23: *Combined representation of efficiency and pressure ratio for all the investigated geometries with endwall contouring.*

Figure 4.24a shows the average total pressure ratio and the average efficiency for all the cases at design speed. The 25% hub case has improved both, compared to the baseline case, whereas the 50% hub case and the 100% casing case have an improved pressure ratio. It is also worth noting that the 75% casing case has the highest average efficiency from the casing perturbed cases. Figure 4.24a shows the peak total pressure ratio and the peak efficiency for all the cases at design speed.

The 50% and 75% hub cases as well as the 100% have increased peak pressure ratios compared to the baseline, while the 25% case has increased peak efficiency. Finally it is worth noting that the 75% casing case has the highest peak efficiency of the casing cases too.

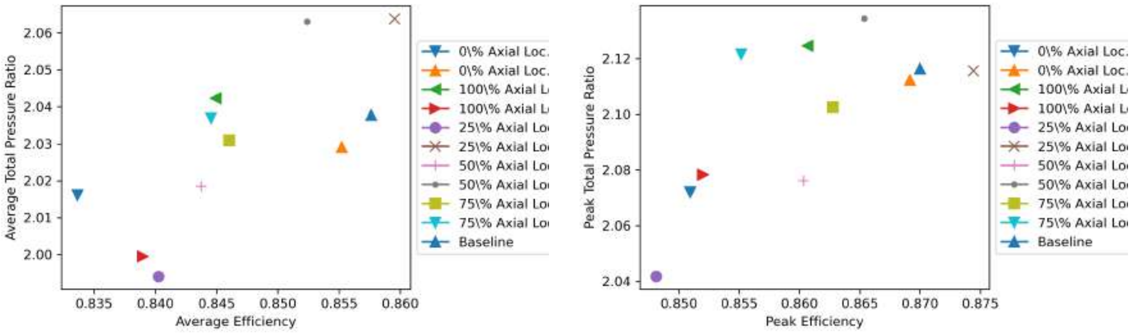

(a) *Combined representation for average performance.*

(b) *Combined representation for peak performance.*

Figure 4.24: *Combined representation of efficiency and pressure ratio for all the investigated geometries with endwall contouring.*

Figure 4.24a shows the choke and stall margin for all the investigated cases at design speed. Compared to the baseline case all the investigated cases have an improvement in choke or stall margin except for the 75% and 100% casing cases. The 25% hub case and 50% casing case have an increase in choke margin but a decrease in stall margin. All the other cases achieve improved choke and stall margins simultaneously. Specifically, the 0% casing case has the highest choke margin overall, with a high stall margin too and the 100% hub case has the highest stall margin, with a high choke margin too.

From the previous analysis, some potential cases for further analysis can be derived. In particular, for the hub perturbed cases the 25% case was the most efficient, the 50% case had the highest pressure ratio, the 75% case had the highest choke margin and the 100% case had the highest stall margin. On the other hand for the casing perturbed cases the 75% case was the most efficient, the 100% case had the highest pressure ratio and the 0% case had the highest choke and stall margin. From the aforementioned cases the 50% hub perturbation and the 75% casing perturbation were chosen as a combination for investigation, aiming to combine the hub case with the highest peak pressure ratio and the casing case with the highest peak efficiency.

In Figure 4.26 the efficiency of the investigated combined case with a contoured hub and casing line is presented, along with the baseline rotor 37 and the cases that have only the hub line or the casing line contoured respectively. The combined case did not have a significant improvement in efficiency compared to the two cases that had a single perturbation.

In Figure 4.27 the pressure ratios of the investigated combined case with a contoured

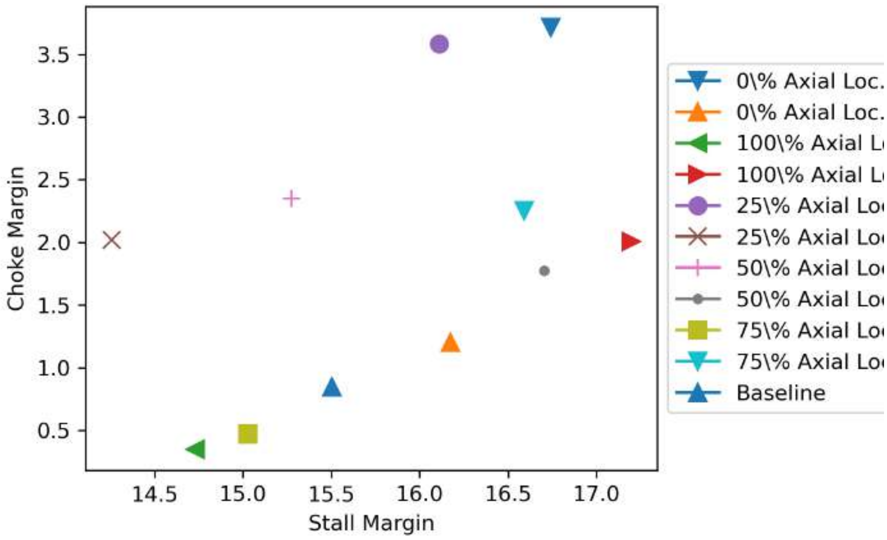

Figure 4.25: *Combined representation of efficiency and pressure ratio for all the investigated geometries with endwall contouring.*

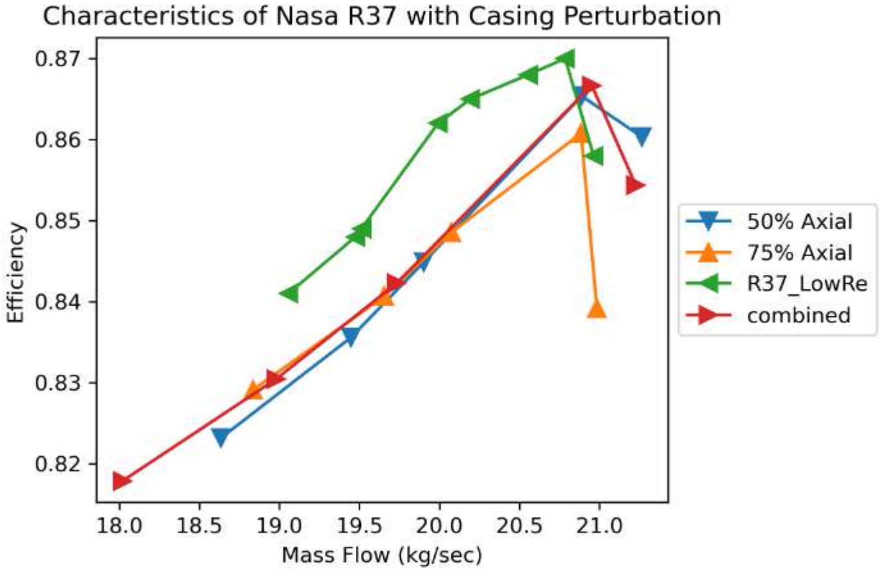

Figure 4.26: *Efficiency characteristics of the rotor 37 baseline, the combined case and the initial two cases at design speed.*

hub and casing line is presented, along with the baseline rotor 37 and the cases that have only the hub line or the casing line contoured respectively. The combined case did not had a significant improvement in pressure ratio compared to the two cases that had a single perturbation and at the same time at stall margin.

The combined case resulted in a lower efficiency compared to the baseline case, as expected, due to the fact that both of the single perturbations that constitute the

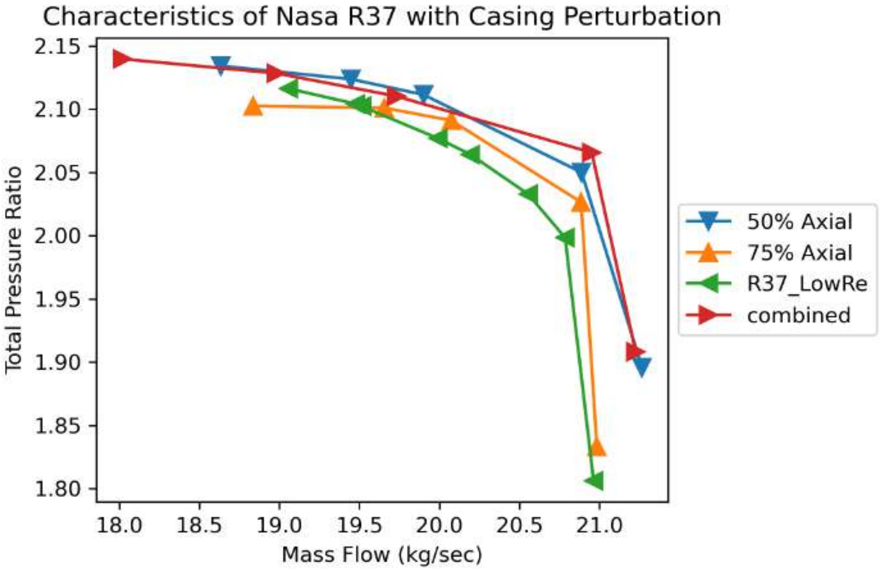

Figure 4.27: *Pressure ratio characteristics of the rotor 37 baseline, the combined case and the initial two cases at design speed.*

investigated combined case had lower efficiency than the baseline. Compared to the single perturbation cases it is worth noting that in comparison to the 75% case the peak and the average efficiency of the combined case is higher. The same is true when compared to the 50% hub case too. As far as the peak pressure ratio is concerned, the combined case can offer a higher pressure ratio at a higher efficiency than both the single perturbation cases, but at a lower efficiency than the baseline. At the same time, the combined case has a higher pressure ratio than all the other cases at their peak efficiencies and higher peak efficiency than the single perturbation cases, but lower than the baseline case. The average pressure ratio is higher than the single perturbation cases and simultaneously at higher average efficiency. Compared to the baseline its average pressure ratio is higher but at a lower average efficiency.

In terms of stall margin, the combined case is superior to all the other cases and has a choke margin similar to the 50% hub case. In Figures 4.28 and 4.29 the circumferential view of the wake of the rotor near peak efficiency and near stall at design speed for the baseline, the single and combined perturbation cases is presented. Similarly to the previous sections, the entropy distribution is shown at 4.5 cm and 10 cm downstream of the rotor's leading-edge As shown the combined case has increased losses near the higher span areas both in the main flow and the wake of the blade, which is also thicker for the combined case but decreased losses near the hub region near peak efficiency. The loss core originating from the tip leakage vortex is thickened leading to increased losses at the higher span region of the blade. The loss reduction near the hub is lower than the loss increase near the tip, leading to a lower peak efficiency than that of the baseline, in accordance with the efficiency characteristics presented previously. Compared to the 50% hub case the combined case has lower main flow losses, while the tip losses are skewed towards the pressure side of the blade. On the other hand, compared to the 75% casing case the losses at the low span regions and at the main flow are reduced. When compared to the single perturbation cases the redistribution of losses caused by the combined geometry case is enough to increase slightly the peak efficiency. Near stall the combined case has increased losses across the whole span in both the wake and main flow regions, leading to a lower efficiency near stall conditions.

(a) *Baseline*

(b) *50% Hub Axial Positioning & 75% Casing Axial Positioning*

Figure 4.28: *Comparison of entropy flow field at 4.5 cm downstream the rotor's leading edge between the baseline rotor 37 and the combined case near peak efficiency.*

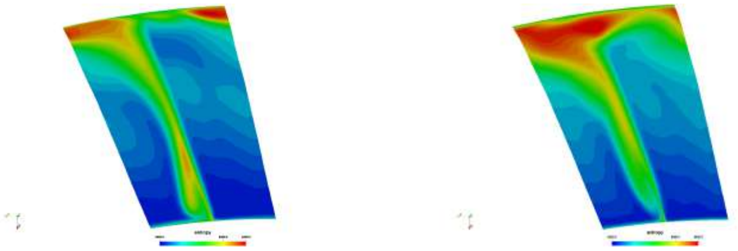

(a) *Baseline*

(b) *50% Hub Axial Positioning & 75% Casing Axial Positioning*

Figure 4.29: *Comparison of entropy flow field at 7 cm downstream the rotor's leading edge between the baseline rotor 37 and the combined case near stall.*

In Figures 4.30 and 4.31 a view of the tip leakage vortex of the rotor near peak efficiency and near stall at the design speed is presented for the baseline and the combined case. Specifically, a contour of Q-criterion is shown, coloured by Mach number, neat the tip region. Compared to the previously shown 50% hub and 75& casing cases, the combined geometry has increased the tip leakage vortex core strength for both the primary and secondary vortex. Near stall, the primary vortex increases in strength but does not merge with the secondary because the secondary vortex has been moved downstream.

Figures 4.32 and 4.33 show contours of the predicted static pressure of the blade suction surfaces, with the grey shaded regions indicating areas of zero axial velocity.

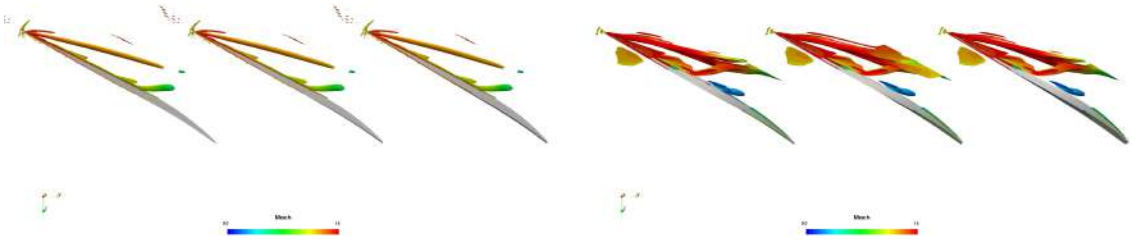

(a) *Baseline* **(b)** *50% Hub Axial Positioning & 75% Casing Axial Positioning*

Figure 4.30: *Comparison of Q criterion contours colored by mach number between the baseline rotor 37 and the combined case near peak efficiency.*

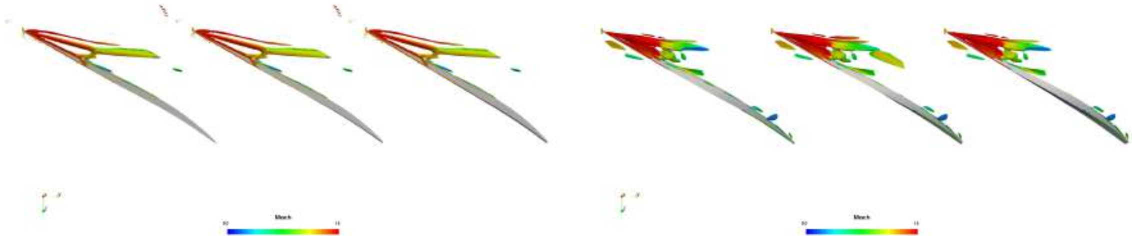

(a) *Baseline* **(b)** *50% Hub Axial Positioning & 75% Casing Axial Positioning*

Figure 4.31: *Comparison of Q criterion contours colored by mach number between the baseline rotor 37 and the casing contoured cases near stall.*

The combined case has a combination of the effects mentioned previously for the single perturbation cases. In particular, the hub loading of the blade is increased, while the shock and the zero axial velocity bubble extend to full span. The tip region is also more loaded near the perturbation and the zero axial velocity bubble is reduced at the lower span regions near the trailing edge while it is increased at the higher span regions near the trailing edge at peak efficiency conditions. Finally, near stall, similarly it has a combination of the effects mentioned in the previous sections.

(a) *Baseline* **(b)** *50% Hub Axial Positioning & 75% Casing Axial Positioning*

Figure 4.32: *Comparison of static pressure contours overlayed with 0 axial velocity contour between the baseline rotor 37 and the combined case near peak efficiency.*

(a) *Baseline* **(b)** *50% Hub Axial Positioning & 75% Casing Axial Positioning*

Figure 4.33: *Comparison of static pressure contours overlayed with 0 axial velocity contour between the baseline rotor 37 and the combined case near stall.*

Chapter 5

Conclusion

5.1 Overview

In this diploma thesis an investigation of the impact of endwall contouring on the performance and operability of the open case of NASA Rotor 37 was carried out. In particular, the axial location of the maximum depth of the endwall profile was studied through a total of ten cases that compared to the baseline NASA Rotor 37 had a single perturbation either on the hub or casing surface, while in the end of the thesis a case with a combination of hub and casing perturbations was presented.

The rotor blading was reconstructed from the original NASA Technical Paper 1337 coordinates [10]. A set of hub surfaces with convex valleys and a set of casing surfaces with concave peaks near the geometry of the blade were generated with the use of B-Splines. Also, a case with a combination of perturbations on the hub and casing surfaces was generated with the same method.

Before evaluating the effect of the altered annulus lines, a mesh for the open case of the NASA Rotor 37 that contained the baseline geometry for the hub and casing was created using PADRAM and simulated at a range of massflows at the design speed using PUMA. In order to validate the results of these simulations, the computed data were compared with experimental measurements and with results from previous CFD simulations of the same case. A mesh of 2.8 millions cells was generated and the Spallart-Allmaras turbulence model without wall functions was used for the CFD simulations. The computed flowfield from PUMA captured both the performance and the flow structures of the rotor blading with sufficient accuracy.

As a result, the same mesh and CFD configurations were used for the endwall contouring investigation. The changes in the annulus line of the rotor affected the main fluid phenomena that take place in the blading passage, that lead to differences in the performance and operability of the rotor. One of the effects of the new endwall profiles was the redistribution of the blade loading and the change of the shockwave position that lead to changes in the wake of the rotor, the horseshoe vortex and the hub corner separation and secondly, the change of tip leakage vortex structure involving changes in its strength and angle relative to the flow and the axial positioning of the secondary tip vortex.

5.2 Conclusions and Proposal for Future Work

By completing the studies in this diploma thesis, the following conclusions are drawn:

- As far as the hub contouring is concerned, the cases that have their maximum depth near the shockwave position inside the blade passage increased the pressure ratio and the efficiency, whereas the cases that have their maximum near the trailing edge increase stall and choke margin. The first increased the loading of the lower span are of the blade near the leading edge, whereas the horseshoe vortex was redirected and the hub corner separation was reduced, while the latter being downstream of the shock did not have a significant impact on the pressure distribution of the blade but relocated the starting point of the secondary tip leakage vortex upstream compared to the baseline.
- As far as the casing contouring is concerned, the cases that have their maximum depth near the trailing edge lead to an increase in the stall and choke margin. The effect of these geometries on the flow was mainly the change of the tip leakage vortex location to an upstream point compared to the baseline, while also there was a moderate increase of the blade loading in the tip region near the leading edge.
- The case with the combination of endwall perturbations near the shockwave lead to an increase of pressure ratio and stall margin, combining positive effects on the flowfield from the single perturbation cases.

5.3 Proposal for Future Work

Based on the results of this investigation the following can be proposed for future work:

- Investigation of the effect of the magnitude of the maximum depth of the endwall perturbations. For instance, a smaller magnitude can be utilised for the cases that the maximum depth of the perturbation was placed near the trailing edge to reduce the increased the hub losses that these cases had.
- Simulation of the full range of speed of the NASA Rotor 37 in order to study the effect of the endwall contouring at lower rotational speeds along with an investigation of different tip clearances and their interaction with the modified tip leakage vortex of the contoured endwalls.
- Inclusion of the stator geometry in order to simulate the full stage of the NASA Rotor 37 geometry and the effects of endwall contouring on the rotor-stator

interaction.

- Investigation of combinations of the cases that were investigated in this thesis and had a positive effect either on the pressure ratio and efficiency or the stall and choke margin of the rotor.

Bibliography

[1] Mathioudakis, K.M.: *Introduction to Aircraft Engines: Jet Engines.* National Technical University of Athens, 2016.

[2] K.D. Papailiou, K.M. Mathioudakis, Kyriakos C. Giannakoglou: *Introduction to Thermal Turbomachines.* National Technical University of Athens, 2000.

[3] Gallimore, S. J.: *Axial flow compressor design†.* Proceedings of the Institution of Mechanical Engineers, Part C: Journal of Mechanical Engineering Science, 213(5):437–449, 1999.

[4] Biollo, R. and Benini, E.: *Recent advances in transonic axial compressor aerodynamics.* Progress in Aerospace Sciences, 56:1–18, 2013, ISSN 0376-0421.

[5] Suder, K.L. and Celestina, M.L.: *Experimental and Computational Investigation of the Tip Clearance Flow in a Transonic Axial Compressor Rotor.* NASA TM–106711, 1994.

[6] Denton, J. D.: *The 1993 IGTI Scholar Lecture: Loss Mechanisms in Turbomachines.* Journal of Turbomachinery, 115(4):621–656, October 1993.

[7] *Three Dimensional Flow in a Linear Compressor Cascade at Design Conditions*, volume Volume 1: Turbomachinery of *Turbo Expo: Power for Land, Sea, and Air*, June 1991.

[8] Halstead, D. E., Wisler, D. C., Okiishi, T. H., Walker, G. J., Hodson, H. P., and Shin, H. W.: *Boundary Layer Development in Axial Compressors and Turbines: Part 1 of 4—Composite Picture.* Journal of Turbomachinery, 119(1):114–127, January 1997.

[9] *A Study of Spike and Modal Stall Phenomena in a Low-Speed Axial Compressor*, volume Volume 1: Aircraft Engine; Marine; Turbomachinery; Microturbines and Small Turbomachinery of *Turbo Expo: Power for Land, Sea, and Air*, June 1997.

[10] Red, L. and Moore, R.D.: *Design and Overall Performance of Four Highly-Loaded, High Speed Inlet Stages for an Advanced, High Pressure Ratio Core Compressor.* NASA TP–1337, 1978.

[11] Reid, L. and Moore, R. D.: *Experimental Study of Low Aspect Ratio Compressor Blading*. Journal of Engineering for Power, 102(4):875–882, October 1980.

[12] Suder, K. L.: *Blockage Development in a Transonic, Axial Compressor Rotor*. Journal of Turbomachinery, 120(3):465–476, July 1998.

[13] I., Kabolis: *Multilevel, multiprocessor aerodynamic optimization algorithms in turbine engines*. PhD thesis, Laboratory Of Thermal Turbomachines, National Technical University Of Athens, Athens, 2009.

[14] X., Troboukis: *Numerical solution of aerodynamic-aeroelasticity problems in graphics card processors*. PhD thesis, Laboratory Of Thermal Turbomachines, National Technical University Of Athens, Athens, 2012.

[15] K., Tsiakas: *Development of shape parameterization techniques, a flow solver and its adjoint, for optimization on GPUs. Turbomachinery and external aerodynamics applications*. PhD thesis, Laboratory Of Thermal Turbomachines, National Technical University Of Athens, Athens, 2019.

[16] Hah, Chunill: *Large eddy simulation of transonic flow field in nasa rotor 37*. January 2009.

[17] Hah, C.: *A Navier-Stokes Analysis of Three-Dimensional Turbulent Flows Inside Turbine Blade Rows at Design and Off-Design Conditions*. Journal of Engineering for Gas Turbines and Power, 106(2):421–429, April 1984.

[18] Dunham, J., Aerospace Research, North Atlantic Treaty Organization. Advisory Group for, Propulsion, Development., and 26, Energetics Panel. Working Group: *CFD Validation for Propulsion System Components*. AGARD AR. AGARD, North Atlantic Treaty Organization, 1998.

[19] Hubler, D.: *Rotor 37 and stator 37 assembly (series: Photographs relating to agency activities, facilities and personnel, 1973 - 2013)*. `https://catalog.archives.gov/id/17468361`.

[20] Hah, C. and Loellbach, J.: *Development of hub corner stall and its influence on the performance of axial compressor blade rows*. Journal of Turbomachinery-transactions of The ASME, 121:67–77, 1999.

[21] Chima, R.V. and Liou, M. S.: *Comparison of the AUSM+ and H-CUSP Schemes for Turbomachinery Applications*. NASA/TM—2003-212457, 2003.

[22] Roe, P.L: *Approximate riemann solvers, parameter vectors, and difference schemes*. Journal of Computational Physics, 43(2):357–372, 1981.

[23] Dossena, V., Perdichizzi, A., and Savini, M.: *The Influence of Endwall Contouring on the Performance of a Turbine Nozzle Guide Vane*. Journal of Turbomachinery, 121(2):200–208, 1999.

[24] *Influence of Endwall Contouring in Axial Gaps on the Flow Field in a Four-Stage Turbine*, volume Volume 1: Aircraft Engine; Marine; Turbomachinery; Microturbines and Small Turbomachinery of *Turbo Expo: Power for Land, Sea, and Air*, May 2000.

[25] Burd, Steven W. and Simon, Terrence W.: *Flow measurements in a nozzle guide vane passage with a low aspect ratio and endwall contouring.* Journal of Turbomachinery, 122(4):659–666, Feb 2000.

[26] *Development and Application of a Multistage Navier-Stokes Flow Solver: Part II — Application to a High Pressure Compressor Design*, volume Volume 1: Turbomachinery of *Turbo Expo: Power for Land, Sea, and Air*, June 1995.

[27] *Design and Development of a Nine Stage Axial Flow Compressor for Industrial Gas Turbines*, volume Volume 1: Turbomachinery of *Turbo Expo: Power for Land, Sea, and Air*, June 1998.

[28] *Influence of Endwall Contouring on the Transonic Flow in a Compressor Blade*, volume Volume 5: Turbo Expo 2002, Parts A and B of *Turbo Expo: Power for Land, Sea, and Air*, June 2002.

[29] Ito, Yoichi, Watanabe, Toshinori, and Himeno, Takehiro: *Effect of endwall contouring on flow instability of transonic compressor.* International Journal of Gas Turbine, Propulsion and Power Systems, 2(1):24–29, 2008.

[30] Biollo, Roberto and Benini, Ernesto: *Recent advances in transonic axial compressor aerodynamics.* Progress in Aerospace Sciences, 56:1–18, 2013, ISSN 0376-0421.

[31] *Rotor Casing Contouring in High Pressure Stages of Heavy Duty Gas Turbine Compressors With Large Tip Clearance Heights*, volume Volume 7: Turbomachinery, Parts A and B of *Turbo Expo: Power for Land, Sea, and Air*, June 2009.

[32] Kröger, G., Voss, C., and Nicke, E.: *Axisymmetric casing optimization for transoniccompressor rotors.* 2010.

[33] *Theory and Application of Axisymmetric Endwall Contouring for Compressors*, volume Volume 7: Turbomachinery, Parts A, B, and C of *Turbo Expo: Power for Land, Sea, and Air*, June 2011.

[34] *Improving 3D Flow Characteristics in a Multistage LP Turbine by Means of Endwall Contouring and Airfoil Design Modification: Part 1 — Design and Experimental Investigation*, volume Volume 5: Turbo Expo 2002, Parts A and B of *Turbo Expo: Power for Land, Sea, and Air*, June 2002.

[35] Brennan, G., Harvey, N. W., Rose, M. G., Fomison, N., and Taylor, M. D.: *Improving the efficiency of the trent 500-hp turbine using nonaxisymmetric end*

walls—part i: Turbine design. Journal of Turbomachinery, 125(3):497–504, Aug 2003.

[36] MJ., Atkins: *Secondary losses and end-wall profiling in a turbine cascade.* I Mech. E C., 255(1):29–42, 1987.

[37] *Improving Turbine Efficiency Using Non-Axisymmetric End Walls: Validation in the Multi-Row Environment and With Low Aspect Ratio Blading*, volume Volume 5: Turbo Expo 2002, Parts A and B of *Turbo Expo: Power for Land, Sea, and Air*, June 2002.

[38] Hartland, J. C., Gregory-Smith, D. G., Harvey, N. W., and Rose, M. G.: *Nonaxisymmetric turbine end wall design: Part ii—experimental validation.* Journal of Turbomachinery, 122(2):286–293, Feb 1999.

[39] Praisner, T., Allen-Bradley, E., Grover, E. A., Knezevici, D., and Sjolander, S.: *Application of nonaxisymmetric endwall contouring to conventional and high-lift turbine airfoils.* Journal of Turbomachinery-transactions of The Asme, 135:061006, 2013.

[40] DC, Knezevici, SA, Sjolander, TJ, Praisner, E, Allen Bradley, and EA, Grover: *Measurements of secondary losses in a turbine cascade with the implementation of 349 nonaxisymmetric endwall contouring.* J Turbomach, 132(2):11013, 2009.

[41] Shaw, J.A. and Weatherill, N.P.: *Automatic topology generation for multiblock grids.* Applied Mathematics and Computation, 52(2):355–388, 1992, ISSN 0096-3003.

[42] JOHN DANNENHOFFER, III: *A new method for creating grid abstractions for complex configurations*.

[43] Löhner, Rainald and Parikh, Paresh: *Generation of three-dimensional unstructured grids by the advancing-front method.* International Journal for Numerical Methods in Fluids, 8(10):1135–1149, 1988.

[44] Baker, Timothy J.: *Prospects and expectations for unstructured methods.* In *Surface Modeling, Grid Generation, and Related Issues in Computational Fluid Dynamic (CFD) Solutions*, pages 273–287, March 1995.

[45] Benek, J., Steger, J., and Dougherty, F.: *A chimera grid scheme.* 2011.

[46] BENEK, J., BUNING, P., and STEGER, J.: *A 3-D chimera grid embedding technique*.

[47] KAO, KAI HSIUNG, LIOU, MENG SING, and CHOW, CHUEN YEN: *Grid adaptation using Chimera composite overlapping meshes*.

[48] Kallinderis, Y., Khawaja, A., and McMorris, H.: *Hybrid prismatic/tetrahedral grid generation for viscous flows around complex geometries.* AIAA Journal, 34(2):291–298, 1996.

[49] Irmisch, S., Walker, D., Bettelini, M., Haselbacher, A., Benz, E., and Kallinderis, Y.: *Efficient use of hybrid grids in modern turbomachinery applications*.

[50] Aftosmis, M, Melton, J, and Berger, M: *Adaptation and surface modeling for Cartesian mesh methods*. `https://arc.aiaa.org/doi/abs/10.2514/6.1995-1725`.

[51] Shahpar, S. and Lapworth, L.: *Padram: Parametric design and rapid meshing system for turbomachinery optimisation.* Volume 6, January 2003.

[52] "Thompson J.F., Weatherill N.P. and B.K.", Soni: *"Handbook of Grid Generation (1st ed.)"*. "CRC Press", "Boca Raton", "1998".

[53] SPALART, P. and ALLMARAS, S.: *A one-equation turbulence model for aerodynamic flows*.

[54] T., Zervogiannis: *Optimization methods in aerodynamics and turbomachinery based on the adjoint technique, hybrid grids and the exact hessian matrix.* PhD thesis, Laboratory Of Thermal Turbomachines, National Technical University Of Athens, Athens, 2011.

[55] A., Varvara: *Aerodynamic analysis and design methods at high and low speed flows, on multiprocessor platforms.* PhD thesis, Laboratory Of Thermal Turbomachines, National Technical University Of Athens, Athens, 2005.

[56] Courant R., Friedrichs K., Lewy H.: *Uber die partiellen differenzengleichungen der mathematischen physik.* 100(1):32–74, 1928.

Appendix A

The GPU-enabled CFD solver

For the flow analysis of the compressor blade the GPU-enabled CFD solver is used, developed by PCOpt/NTUA, also known as the PUMA (Parallel Unstructured Multi-row Adjoint) solver. The PUMA solver has been the focus of already 3 PhD theses ([13], [14], [15]), and was based on an already existing in-house CFD solver running on CPUs. The PUMA solver solves numerically the Navier-Stokes equations using the Finite volume method with vertex centered volumes and storage, providing second order accuracy, for compressible fluid flows. The main advantage of this solver is the fact that it runs on clusters of GPUs, reducing the computational cost to a great extent.

A.1 Governing Equations

The RANS equations are time-averaged equations of motion for turbulent fluid flows, based on the conservation laws of mass (continuity), momentum and energy. Assuming a coordinate system $O(x_1 x_2 x_3)$ which rotates at a constant speed $\omega_m (m = 1, 2, 3)$ and compressible fluid flow, the Navier–Stokes equations are expressed as :

$$R_n^{MF} = \frac{\partial U_n}{\partial t} + \frac{\partial f_{nk}^{inv}}{\partial x_k} - \frac{\partial f_{nk}^{vis}}{\partial x_k} + S_n = 0 \tag{A.1}$$

In A.1, U_n stands for the conservative flow variables namely $U_n = \begin{bmatrix} \rho & \rho v_1^A & \rho v_2^A & \rho v_3^A & \rho E \end{bmatrix}$ with ρ being the fluid density, $v_m^A (m = 1, 2, 3)$ being the velocity components with respect to the absolute/inertial frame of reference and E the energy per unit mass. Taking into aacount that Eq. A.1 can be used for steady state flows, which are going to be numerically solver with the technique of time marching taking advantage of the properties of hyperbolic equations in time and space, t represent pseudo-time. Inviscid fluxes f_{nk}^{inv} , the viscous fluxes f_{nk}^{vis} and the source terms S_n (corresponding to the Coriolis force) are defined as :

$$f_{nk}^{inv} = \begin{bmatrix} \rho v_k^R \\ \rho v_1^A v_k^R + p\delta_{1k} \\ \rho v_2^A v_k^R + p\delta_{2k} \\ \rho v_3^A v_k^R + p\delta_{3k} \\ \rho h_t v_k^R + v_k^F p \end{bmatrix} f_{nk}^{vis} = \begin{bmatrix} 0 \\ \tau_{1k} \\ \tau_{2k} \\ \tau_{3k} \\ v_l^A \tau_{lk} + q_k \end{bmatrix} S_n = \begin{bmatrix} 0 \\ \rho \epsilon_{1lk} \omega_l v_k^A \\ \rho \epsilon_{2lk} \omega_l v_k^A \\ \rho \epsilon_{3lk} \omega_l v_k^A \\ 0 \end{bmatrix} \tag{A.2}$$

where p stands for the static pressure, τ_{km} are components of the viscous stress tensor, h_t is the total enthalpy, q_k are the components of the heat flux, δ_{km} is the Kronecker delta, ω_k are the components of the rotational speed and the symbol $e_m lk$ is teh Levi Civita symbol. In A.1 - A.2 and the rest of the thesis, the Einstein convention is employed according to which summation is indicated by repeated indices in the same term. The relative velocity components v_m^R are linked to the absolute ones v_m^A through the equation $v_m^A = v_m^R + v_m^F$, with $v_m^F = \epsilon_{mlk}\omega_k(x_k - x_k^C)$ being the rotating/non–inertial frame velocity and x_k^C the position vector of the center of rotation. A.2 are supplemented by the definitions described next. First of all, the (k, m) component of the viscous stress tensor τ_{km} for Newtonian fluid that was mentioned above is given by:

$$\tau_{km} = \frac{\mu + \mu_t}{Re_0}\left(\frac{\partial v_k^A}{\partial x_m} + \frac{\partial v_m^A}{\partial x_k} - \frac{2}{3}\delta_{km}\frac{\partial v_l^A}{\partial x_l}\right) \tag{A.3}$$

The k component of the heat flux (q_k) mentioned above is defined as:

$$q_k = \frac{C_p}{Re_0}\left(\frac{\mu}{Pr} + \frac{\mu_t}{Pr_t}\right)\frac{\partial T}{\partial x_k} \tag{A.4}$$

where C_p is the specific heat under constant pressure,μ is the molecular viscosity, μ_t is the turbulent viscosity , Pr is the Prandtl number and Pr_t is the turbulent Prandtl number. Since the fluid is assumed to be a perfect gas, static temperature (T) is related to pressure and density through the equation of state:

$$p = \rho R_g T \tag{A.5}$$

with R_g being the specific gas constant. The specific heat ratio (γ) is :

$$\gamma = \frac{C_p}{C_v} \tag{A.6}$$

where C_v is the specific heat under constant volume. Total or stagnation enthalpy (h_t) is:

$$h_t = E + \frac{p}{\rho} \tag{A.7}$$

and for a perfect gas the total enthalpy is linked to pressure (p), density (ρ) and velocity ($v_l^A, l = 1, ..., 3$) through

$$h_t = \frac{\gamma p}{\rho(\gamma - 1} + \frac{1}{2} v_l^A v_l^A \tag{A.8}$$

The local speed of sound (c) for perfect gases is given as :

$$c = \sqrt{\gamma R_g T} \tag{A.9}$$

The absolute Mach number (M)then is:

$$M = \frac{\sqrt{v_l^A v_l^A}}{c} \tag{A.10}$$

Total or stagnation temperature (T_t) is:

$$T_t = T + \frac{v_l^A v_l^A}{2C_p} \tag{A.11}$$

Total or stagnation pressure for perfect gases (p_t) is given by:

$$p_t = p(1 + \frac{\gamma - 1}{2} M^2)^{(\frac{\gamma}{\gamma - 1})} \tag{A.12}$$

A.2 The Spalart-Allmaras (S-A) Turbulence Model

Turbulent viscosity μ_t is computed be employing the one-equation Spalart-Allmaras turbulence model [53]. According to this model, an additional PDE is solved for the turbulence field $\tilde{\nu}$, namely

$$\begin{aligned} R^{SA} = \frac{\partial(\rho\tilde{\nu})}{\partial t} + \frac{\partial(\rho\tilde{\nu}v_k^R)}{\partial x_k} - \frac{\rho}{Re_0\sigma}\{\frac{\partial[\nu+\tilde{\nu}\frac{\partial\tilde{\nu}}{\partial x_k}]}{\partial x_k} + c_{b2}\frac{\partial\tilde{\nu}}{\partial x_k}\frac{\partial\tilde{\nu}}{\partial x_k}\} \\ -\rho c_{b1}(1-f_{t2})\tilde{S}\tilde{\nu} + \frac{\rho}{Re_0}(c_{w1}f_w - \frac{c_{b1}}{\kappa^2}f_{t2})(\frac{\tilde{\nu}}{\Delta})^2 \end{aligned} \tag{A.13}$$

where Δ stands for the distance of each point within the flow domain from the closest wall boundary. Solving A.13, μ_t is computed from $\tilde{\nu}$ by $\mu_t = \rho\tilde{\nu}f_{v1}$. A.13 is supplemented by the following relations and constants [53]:

$$\begin{aligned} X = \frac{\tilde{\nu}}{\nu}, f_{v_1} = \frac{X^3}{X^3 + c_{v_1}^3}, S = \sqrt{2\epsilon_{klm}\epsilon_{kqr}\frac{\partial v_m^A}{\partial x_l}\frac{\partial u_r^A}{\partial x_q}}, \\ \tilde{S} = S + \frac{\tilde{\nu}}{\kappa^2\Delta^2}, f_w = g(\frac{1+c_{w_3}^6}{g^6 + c_{w_3}^6}), g = r + c_{w_2}(r^6 - r), \\ r = min[\frac{\tilde{\nu}}{Re_0\tilde{S}\kappa^2\Delta^2}, 10], \tilde{\mu} = \rho\tilde{\nu}, f_{t_2} = c_{t_3}e^{-c_{t_4}X^2}, \\ \sigma = \frac{2}{3}, c_{b_1} = 0.1355, c_{b_2} = 0.622, \kappa = 0.41, c_{w_1} = \frac{c_{b1}}{\kappa^2} + \frac{1+c_{b2}}{\sigma}, \\ c_{w_2} = 0.3, c_{w_3} = 2, c_{v_1} = 7.1, c_{t_3} = 1.2, c_{t_4} = 0.5 \end{aligned} \tag{A.14}$$

A.3 Boundary Conditions

In order to fully define the flow problem, A.1 and A.13 must be accompanied by a set of appropriate boundary conditions. These conditions vary, depending on the type of each physical boundary and whether they are strongly or weakly imposed. Along pairs of periodic boundaries, appropriate periodic conditions are imposed. For linear cascades, two points are assumed to be periodically paired if they have two of their coordinates equal and differ on the third by the cascade pitch. In such cases all flow variables (scalar and vector ones) must be equal between periodically paired points. In case of peripheral rows, two points are periodically paired if their projections on the meridional plane coincide and their circumferential position differs by the blade row pitch. Between paired points all scalar quantities are the same, while every vector and tensor quantity (e.g. velocity or spatial derivatives) is rotated by the row pitch. Wall, inlet and outlet boundaries are analysed separately in the following subsections. Farfield boundaries are treated as a combination of inlet and outlet boundary, depending on the local velocity field. If flow enters the domain the boundary is locally treated as inlet, otherwise it is treated as outlet.

A.3.1 Wall Boundary Conditions

For slip walls, the no–penetration condition applies, namely the normal component of the relative to the wall velocity is set to zero. Let the velocity of the wall boundary be denoted by $v_k^W, (k = 1, 2, 3)$ (i.e. $v_k^W = 0$ for stationary walls and nonzero otherwise), then the no–penetration condition is expressed as

$$v_k^A n_k = v_k^W n_k \tag{A.15}$$

For no–slip wall boundaries, the absolute velocity is set equal to the wall boundary velocity (A.16). In addition, for the computations carried out for this thesis the turbulence variable $\tilde{\nu}$ was set to zero and the turbulent boundary layer was resolved down to the wall (Low Reynolds approach, A.17).

$$v_k^A = v_k^W \tag{A.16}$$

$$\tilde{\nu} = 0 \tag{A.17}$$

Considering the thermal conditions for the wall boundaries, depending on the case, these were set as adiabatic, which can respectively be written as

$$q_k n_k = 0 \tag{A.18}$$

A.3.2 Inlet Boundary Conditions

In the case of NASA Rotor 37 the axial velocity at the inlet is supersonic whereas in the outlet is subsonic and the limitation of a single angle of attack applies, that is to say that the inlet angle of attack of the flow is determined unambiguously by the blading and the Mach number, while the boundary conditions are imposed as discussed above. Moreover, the total pressure (p_t^{IN}), total temperature (T_t^{IN}), and inlet absolute velocity direction are specified. The inlet velocity direction is given in terms of two angles, namely θ_1^{IN} and θ_2^{IN}. Thus, for the inlet boundaries, four quantities are specified and a fifth one has to be extrapolated from the flow domain. In this thesis the local Mach number was chosen to be extrapolate. Then, Eqs.

A.10 - A.12 are used to compute all the necessary flow quantities. In cases where the velocity normal to the boundary is supersonic both at the inlet and outlet, then the static pressure p^{out} is given at the inlet and respectively at the outlet the static pressure is extrapolated from the flow domain, $p^{out} = p^{P}$.

Concerning turbulence, the inlet turbulence level is prescribed either by setting the inlet turbulence variable $\tilde{\nu}^{IN}$ or by setting the viscosity ratio $(\frac{\nu_t}{\nu})^{IN}$.

A.3.3 Outlet Boundary Conditions

To maintain a well–posed boundary value problem, a single flow quantity is specified for the flow conditions. The quantity set is the outlet mean static pressure. Since only the value of an integral quantity over the whole outlet boundary is set, values for pressure and normal to the outlet velocity, respectively, are computed iteratively by uniformly correcting the ones extrapolated from the fluid domain, so as to achieve the prescribed integral quantity. In particular, the outlet static pressure is specified at the hub radius and, then, the radial distribution of static pressure from hub to tip/casing is computed by solving the radial equilibrium equation

$$\frac{\partial p}{\partial r} = \rho \frac{(v_\theta^A)^2}{r} \tag{A.19}$$

where r is the radial position and v_θ^A the peripheral velocity component , given by

$$(v_\theta^A) = v_\theta + \omega_1 r \tag{A.20}$$

The remaining four flow quantities are extrapolated from the fluid domain. For the turbulence model, the outlet is assumed to be convective and a zero Neumann boundary condition is applied ($\tilde{\nu}$ is extrapolated from the fluid domain).

A.4 Discretisation of the Governing Equations

For the discretisation of Eqs. A.1 and A.13 the vertex-centered variant of the finite volume technique is used on meshes consisting of tetrahedra, pyramids, prisms and hexahedra. A finite volume cell is formed around each mesh node P by connecting the edges midpoints, face centers and element barycenters of the edges,faces and elements attached to this node, respectively. An example of the finite volume formed around node P is shown in A.1 .

The finite volume method includes the integration of of Eqs. A.1 and A.13 for the volume described previously. In the case of 3D flows, the integration of Eq. A.1 for

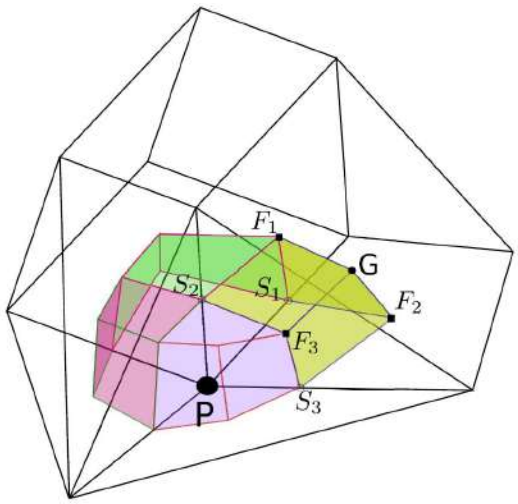

Figure A.1: *A vertex–centered finite volume formed around node P [54]*

the finete volume of node P leads to

$$\int_{V_P} \frac{\partial U_n}{\partial t}\, dV + \int_{V_P} \frac{\partial f_{nk}^{inv}}{\partial x_k}\, dV - \int_{V_P} \frac{\partial f_{nk}^{vis}}{\partial x_k}\, dV + \int_{V_P} S_n\, dV = 0 \tag{A.21}$$

and by applying the Green-Gauss theorem to the integral given above and assuming that the source value on a finite volume S_n^P remains constant within the finite volume

$$\int_{V_P} \frac{\partial U_n}{\partial t}\, dV + \int_{\partial V_P} f_{nk}^{inv} \hat{n_k}\, d(\partial V) - \int_{\partial V_P} f_{nk}^{vis} \hat{n_k}\, d(\partial V) + S_n^P V_P = 0 \tag{A.22}$$

where V^P is the finite volume of node P, ∂V^P is the boundary of the finite volume formed around node P and $\hat{n_k}, (k = 1, 2, 3)$ the corresponding unit normal components. Respectively integrating Eq. A.13 leads to

$$\begin{aligned} \int_{V_P} \frac{\partial(\rho\tilde{\nu})}{\partial t}\, dV + \int_{\partial V_P} \tilde{\mu} v_k^R \hat{n_k}\, d(\partial V) = \\ = \frac{\rho}{Re_0 \sigma} \int_{\partial V_P} [(1 + c_{b2})(\nu\tilde{\nu}) \frac{\tilde{\nu}}{x_k} \hat{n_k}]\, d(\partial V) - \frac{\rho}{Re_0 \sigma} \int_{V_P} [c_{b2}(\nu + \tilde{\nu}) \frac{\partial \frac{\partial \tilde{\nu}}{x_k}}{x_k}]\, dV \\ + int_{V_P}[\rho c_{b1}(1 - f_{t2})\tilde{S}\tilde{\nu} - \frac{\rho}{Re_0}(c_{w1} f_w - \frac{c_{b1}}{\kappa^2} f_{t2})(\frac{\tilde{\nu}}{\Delta})^2]\, dV \end{aligned} \tag{A.23}$$

The pseudo-time step is [55]

$$\Delta_P = \frac{CFLV_P}{\sum_i T_i^{inv} + T_i^{vis}} \tag{A.24}$$

where two terms are included, the inviscous T^{inv} and the viscous T^{vis} . CFL is the Courant-Friedrichs-Lewy number [56], which is selected so as to ensure the fastest possible convergence rate without disturbing the stability of the solution scheme. The inviscous term is equal to

$$T_i^{vis} = (|u_i| + c)V_{Pi} \tag{A.25}$$

where $V_P i$ are the projections of the finite volume of node P in the direction of i. The term in the parenthesis corresponds to the maximum propagation speed of information per direction. The viscous term can be calculated as

$$T_i^{inv} = 2(\mu + \mu_t)\frac{V_P}{\rho \sum_i V_{Pi}} \tag{A.26}$$

A.5 GPU Implementation of the Flow Solver

The different architecture and hardware capabilities of GPUs compared to CPUs raise some issues concerning the discretization and numerical algorithms used for the solution of the flow equations. GPUs are shared memory processors, meaning that all GPU threads which are executed in parallel, access the same RAM. This may lead to thread race conditions which, if not resolved properly, can make the numerical solution process unpredictable. This issue, is more profound in scatter–add algorithms, employed in the computation of the numerical fluxes and the corresponding numerical flux Jacobians. In addition, the amount of cache memory of GPUs (even the latest ones) is still limited compared to CPUs, demanding a more delicate memory handling, so as to minimize the overall memory latency. In this section, some of the GPU–specific techniques, developed in the scope of the PhD Thesis of X. Trompoukis [14] and, also, used herein, are revisited. The employment of these techniques results in a GPU variant of the flow solver which can be up to 45 times faster compared to the CPU variant of the same flow solver. At this point, it must be noted that the speedup figures may vary, depending on the actual GPU and CPU software used for the comparison.

The GPU solver uses the delta-formulation for solving eqs. A.1 and A.13 in their discretised form. In fact, the unknown variable is the update (ΔU_n) in the flow variables from one pseudo-time iteration (κ) to the next ($\kappa + 1$) as presented here.

$$\begin{aligned}\frac{\partial R_n}{\partial U_m}\Delta U_m &= -R_n \\ U_n^{k+1} &= U_n^k + \Delta U_n\end{aligned} \tag{A.27}$$

where $\frac{\partial R_n}{\partial U_m}$ is the Jacobian matrix and is referred to as the left hand side (l.h.s.), while R_n is the residuals and is referred to as the right hand side (r.h.s.). To further enhance the PUMA solver's efficiency, the Mixed Precision Arithmetics (MPA) is used [55]. It employs a combination of single and double precision arithmetics for the computations and data storage. Specially, the residuals R_n are computed and stored as double precision numbers, due to the need for high accuracy.On the contrary, the l.h.s. coefficients ($\frac{\partial R_n}{\partial U_m}$) are computed with Double Precision Arithmetics (DPA) but are stored in Single Precision Arithmetics (SPA). The MPA technique, compared to the DPA technique, provides the same accuracy in the results, while reducing the memory requirements and the number of total memory accesses. There is only a slight difference in the convergence rate between the two techniques.

Appendix B

NASA Rotor 37 Coordinates

In the following table the NASA Rotor 37 coordinates are presented as extracted from the NASA Technical Paper 1337 [10].

Blade 1 Coordinates			Blade 2 Coordinates		
x	y	z	x	y	z
0	0,000251	0,1778	0	0,000244	0,18288
0,00254	0,001488	0,1778	0,00254	0,001379	0,18288
0,00508	0,002494	0,1778	0,00508	0,002289	0,18288
0,00762	0,003437	0,1778	0,00762	0,003137	0,18288
0,01016	0,004315	0,1778	0,01016	0,003927	0,18288
0,0127	0,005133	0,1778	0,0127	0,004656	0,18288
0,01524	0,005992	0,1778	0,01524	0,005329	0,18288
0,01778	0,006604	0,1778	0,01778	0,005944	0,18288
0,02032	0,007252	0,1778	0,02032	0,006502	0,18288
0,02286	0,007808	0,1778	0,02286	0,007003	0,18288
0,0254	0,008258	0,1778	0,0254	0,007407	0,18288
0,02794	0,008578	0,1778	0,02794	0,007681	0,18288
0,03048	0,008763	0,1778	0,03048	0,007816	0,18288
0,03302	0,008804	0,1778	0,03302	0,007816	0,18288
0,03556	0,008692	0,1778	0,03556	0,007673	0,18288
0,0381	0,008415	0,1778	0,0381	0,007386	0,18288
0,04064	0,007963	0,1778	0,04064	0,006944	0,18288
0,04318	0,007313	0,1778	0,04318	0,006332	0,18288
0,04572	0,006434	0,1778	0,04572	0,005532	0,18288
0,04826	0,005281	0,1778	0,04826	0,004516	0,18288
0,0508	0,003772	0,1778	0,0508	0,003244	0,18288
0,05334	0,00175	0,1778	0,05334	0,001636	0,18288
0,054656	0,0003	0,1778	0,054935	0,000279	0,18288
0,054656	0,0003	0,1778	0,054935	0,000279	0,18288
0,05334	0,000495	0,1778	0,05334	0,000465	0,18288
0,0508	0,001615	0,1778	0,0508	0,001265	0,18288
0,04826	0,002464	0,1778	0,04826	0,001902	0,18288
0,04572	0,003101	0,1778	0,04572	0,002403	0,18288
0,04318	0,003566	0,1778	0,04318	0,002789	0,18288
0,04064	0,003886	0,1778	0,04064	0,003071	0,18288
0,0381	0,004077	0,1778	0,0381	0,003256	0,18288
0,03556	0,004161	0,1778	0,03556	0,003358	0,18288
0,03302	0,00414	0,1778	0,03302	0,003376	0,18288
0,03048	0,004028	0,1778	0,03048	0,003315	0,18288
0,02794	0,003835	0,1778	0,02794	0,003185	0,18288
0,0254	0,003569	0,1778	0,0254	0,002995	0,18288
0,02286	0,003244	0,1778	0,02286	0,002723	0,18288
0,02032	0,002875	0,1778	0,02032	0,002426	0,18288
0,01778	0,00251	0,1778	0,01778	0,002134	0,18288
0,01524	0,002146	0,1778	0,01524	0,001839	0,18288
0,0127	0,001786	0,1778	0,0127	0,001537	0,18288
0,01016	0,001427	0,1778	0,01016	0,001232	0,18288
0,00762	0,001064	0,1778	0,00762	0,000925	0,18288
0,00508	0,000701	0,1778	0,00508	0,00061	0,18288
0,00254	0,000333	0,1778	0,00254	0,000292	0,18288
0	0,000251	0,1778	0	0,000244	0,18288

Blade 3 Coordinates			Blade 4 Coordinates		
x	y	z	x	y	z
0	0,000231	0,189992	0	0,000218	0,19685
0,00254	0,001227	0,189992	0,00254	0,001087	0,19685
0,00508	0,002004	0,189992	0,00508	0,001742	0,19685
0,00762	0,002725	0,189992	0,00762	0,002352	0,19685
0,01016	0,003396	0,189992	0,01016	0,002918	0,19685
0,0127	0,004013	0,189992	0,0127	0,003439	0,19685
0,01524	0,004577	0,189992	0,01524	0,003917	0,19685
0,01778	0,00509	0,189992	0,017856	0,004346	0,19685
0,02032	0,00555	0,189992	0,02032	0,004732	0,19685
0,02286	0,005956	0,189992	0,02286	0,005077	0,19685
0,0254	0,006302	0,189992	0,0254	0,005377	0,19685
0,02794	0,006546	0,189992	0,02794	0,005596	0,19685
0,03048	0,006662	0,189992	0,03048	0,005712	0,19685
0,03302	0,00665	0,189992	0,03302	0,005718	0,19685
0,03556	0,006513	0,189992	0,03556	0,005608	0,19685
0,0381	0,006248	0,189992	0,0381	0,00538	0,19685
0,04064	0,005847	0,189992	0,04064	0,005034	0,19685
0,04318	0,005306	0,189992	0,04318	0,004567	0,19685
0,04572	0,004615	0,189992	0,04572	0,003975	0,19685
0,04826	0,003762	0,189992	0,04826	0,003249	0,19685
0,0508	0,002728	0,189992	0,0508	0,002383	0,19685
0,05334	0,001488	0,189992	0,05334	0,001364	0,19685
0,055245	0,000257	0,189992	0,055466	0,000239	0,19685
0,055245	0,000257	0,189992	0,055466	0,000239	0,19685
0,05334	0,000386	0,189992	0,05334	0,000318	0,19685
0,0508	0,000919	0,189992	0,0508	0,000701	0,19685
0,04826	0,001364	0,189992	0,04826	0,001029	0,19685
0,04572	0,001732	0,189992	0,04572	0,0013	0,19685
0,04318	0,002024	0,189992	0,04318	0,001519	0,19685
0,04064	0,002248	0,189992	0,04064	0,001687	0,19685
0,0381	0,002403	0,189992	0,0381	0,001801	0,19685
0,03556	0,002492	0,189992	0,03556	0,001862	0,19685
0,03302	0,002517	0,189992	0,03302	0,001872	0,19685
0,03048	0,002482	0,189992	0,03048	0,001826	0,19685
0,02794	0,002383	0,189992	0,02794	0,001735	0,19685
0,0254	0,002217	0,189992	0,0254	0,0016	0,19685
0,02286	0,002019	0,189992	0,02286	0,001443	0,19685
0,02032	0,001811	0,189992	0,02032	0,001288	0,19685
0,01778	0,001595	0,189992	0,017856	0,00113	0,19685
0,01524	0,001377	0,189992	0,01524	0,00097	0,19685
0,0127	0,001153	0,189992	0,0127	0,00081	0,19685
0,01016	0,000927	0,189992	0,01016	0,000648	0,19685
0,00762	0,000696	0,189992	0,00762	0,000485	0,19685
0,00508	0,00046	0,189992	0,00508	0,000323	0,19685
0,00254	0,000221	0,189992	0,00254	0,000155	0,19685
0	0,000231	0,189992	0	0,000218	0,19685

Blade 5 Coordinates			Blade 6 Coordinates		
x	y	z	x	y	z
0	0,000208	0,2032	0	0,000198	0,20955
0,00254	0,000986	0,2032	0,00254	0,000881	0,20955
0,00508	0,001557	0,2032	0,00508	0,001372	0,20955
0,00762	0,002088	0,2032	0,00762	0,001834	0,20955
0,01016	0,002581	0,2032	0,01016	0,002263	0,20955
0,0127	0,003033	0,2032	0,0127	0,002662	0,20955
0,01524	0,003447	0,2032	0,01524	0,003028	0,20955
0,01778	0,00382	0,2032	0,01778	0,003363	0,20955
0,02032	0,004158	0,2032	0,02032	0,003668	0,20955
0,02286	0,004453	0,2032	0,02286	0,003952	0,20955
0,0254	0,004704	0,2032	0,0254	0,004214	0,20955
0,02794	0,004912	0,2032	0,02794	0,004402	0,20955
0,03048	0,005014	0,2032	0,03048	0,004511	0,20955
0,03302	0,005009	0,2032	0,03302	0,004534	0,20955
0,03556	0,004902	0,2032	0,03556	0,004458	0,20955
0,0381	0,004699	0,2032	0,0381	0,00428	0,20955
0,04064	0,004392	0,2032	0,04064	0,004006	0,20955
0,04318	0,00398	0,2032	0,04318	0,003635	0,20955
0,04572	0,003462	0,2032	0,04572	0,003165	0,20955
0,04826	0,002835	0,2032	0,04826	0,002593	0,20955
0,0508	0,002093	0,2032	0,0508	0,00192	0,20955
0,05334	0,001234	0,2032	0,05334	0,00114	0,20955
0,055593	0,000221	0,2032	0,055613	0,000206	0,20955
0,055593	0,000221	0,2032	0,055613	0,000206	0,20955
0,05334	0,000249	0,2032	0,05334	0,000211	0,20955
0,0508	0,000528	0,2032	0,0508	0,000445	0,20955
0,04826	0,00077	0,2032	0,04826	0,00065	0,20955
0,04572	0,000973	0,2032	0,04572	0,000823	0,20955
0,04318	0,00114	0,2032	0,04318	0,000963	0,20955
0,04064	0,00127	0,2032	0,04064	0,001074	0,20955
0,0381	0,001359	0,2032	0,0381	0,001153	0,20955
0,03556	0,001407	0,2032	0,03556	0,001199	0,20955
0,03302	0,001422	0,2032	0,03302	0,001201	0,20955
0,03048	0,001402	0,2032	0,03048	0,001163	0,20955
0,02794	0,001331	0,2032	0,02794	0,001115	0,20955
0,0254	0,001219	0,2032	0,0254	0,001016	0,20955
0,02286	0,001113	0,2032	0,02286	0,000925	0,20955
0,02032	0,001001	0,2032	0,02032	0,000833	0,20955
0,01778	0,000884	0,2032	0,01778	0,000734	0,20955
0,01524	0,000765	0,2032	0,01524	0,000632	0,20955
0,0127	0,000645	0,2032	0,0127	0,000533	0,20955
0,01016	0,000523	0,2032	0,01016	0,000429	0,20955
0,00762	0,000399	0,2032	0,00762	0,000325	0,20955
0,00508	0,000267	0,2032	0,00508	0,000216	0,20955
0,00254	0,000132	0,2032	0,00254	0,000107	0,20955
0	0,000208	0,2032	0	0,000198	0,20955

Blade 7 Coordinates			Blade 8 Coordinates		
x	y	z	x	y	z
0	0,000188	0,2159	0	0,000178	0,22225
0,00254	0,000775	0,2159	0,00254	0,000691	0,22225
0,00508	0,001181	0,2159	0,00508	0,001029	0,22225
0,00762	0,001562	0,2159	0,00762	0,001349	0,22225
0,01016	0,00192	0,2159	0,01016	0,001648	0,22225
0,0127	0,002256	0,2159	0,0127	0,001928	0,22225
0,01524	0,002565	0,2159	0,01524	0,002187	0,22225
0,01778	0,002852	0,2159	0,01778	0,002428	0,22225
0,02032	0,003117	0,2159	0,02032	0,002649	0,22225
0,02286	0,003363	0,2159	0,02286	0,002855	0,22225
0,0254	0,003597	0,2159	0,0254	0,00304	0,22225
0,02794	0,003772	0,2159	0,02794	0,003211	0,22225
0,03048	0,003907	0,2159	0,03048	0,003358	0,22225
0,03302	0,003952	0,2159	0,03302	0,003426	0,22225
0,03556	0,003904	0,2159	0,03556	0,003409	0,22225
0,0381	0,003764	0,2159	0,0381	0,003305	0,22225
0,04064	0,003533	0,2159	0,04064	0,003117	0,22225
0,04318	0,003211	0,2159	0,04318	0,002842	0,22225
0,04572	0,002799	0,2159	0,04572	0,002487	0,22225
0,04826	0,002299	0,2159	0,04826	0,002045	0,22225
0,0508	0,001704	0,2159	0,0508	0,001524	0,22225
0,05334	0,001021	0,2159	0,05334	0,000919	0,22225
0,055623	0,000191	0,2159	0,055626	0,000175	0,22225
0,055623	0,000191	0,2159	0,055626	0,000175	0,22225
0,05334	0,000165	0,2159	0,05334	0,000127	0,22225
0,0508	0,000343	0,2159	0,0508	0,000262	0,22225
0,04826	0,0005	0,2159	0,04826	0,000378	0,22225
0,04572	0,000635	0,2159	0,04572	0,000475	0,22225
0,04318	0,000742	0,2159	0,04318	0,000551	0,22225
0,04064	0,00082	0,2159	0,04064	0,000607	0,22225
0,0381	0,000874	0,2159	0,0381	0,000638	0,22225
0,03556	0,000894	0,2159	0,03556	0,000648	0,22225
0,03302	0,000886	0,2159	0,03302	0,00063	0,22225
0,03048	0,000846	0,2159	0,03048	0,000584	0,22225
0,02794	0,000772	0,2159	0,02794	0,000521	0,22225
0,0254	0,000688	0,2159	0,0254	0,00046	0,22225
0,02286	0,000607	0,2159	0,02286	0,000401	0,22225
0,02032	0,000531	0,2159	0,02032	0,000348	0,22225
0,01778	0,000455	0,2159	0,01778	0,000297	0,22225
0,01524	0,000384	0,2159	0,01524	0,000249	0,22225
0,0127	0,000315	0,2159	0,0127	0,000206	0,22225
0,01016	0,000249	0,2159	0,01016	0,000163	0,22225
0,00762	0,000183	0,2159	0,00762	0,000119	0,22225
0,00508	0,000119	0,2159	0,00508	7,87E-05	0,22225
0,00254	5,59E-05	0,2159	0,00254	3,81E-05	0,22225
0	0,000188	0,2159	0	0,000178	0,22225

Blade 9 Coordinates			Blade 10 Coordinates		
x	y	z	x	y	z
0	0,000165	0,2286	0	0,000155	0,23495
0,00254	0,000602	0,2286	0,00254	0,000531	0,23495
0,00508	0,000876	0,2286	0,00508	0,000754	0,23495
0,00762	0,001135	0,2286	0,00762	0,000965	0,23495
0,01016	0,001377	0,2286	0,01016	0,001163	0,23495
0,0127	0,001603	0,2286	0,0127	0,001351	0,23495
0,01524	0,001816	0,2286	0,01524	0,001527	0,23495
0,01778	0,002014	0,2286	0,01778	0,001689	0,23495
0,02032	0,0022	0,2286	0,02032	0,001844	0,23495
0,02286	0,002372	0,2286	0,02286	0,001989	0,23495
0,0254	0,002532	0,2286	0,0254	0,002123	0,23495
0,02794	0,002682	0,2286	0,02794	0,00225	0,23495
0,03048	0,002822	0,2286	0,03048	0,00238	0,23495
0,03302	0,002918	0,2286	0,03302	0,002482	0,23495
0,03556	0,002934	0,2286	0,03556	0,00254	0,23495
0,0381	0,00287	0,2286	0,0381	0,00252	0,23495
0,04064	0,002725	0,2286	0,04064	0,002423	0,23495
0,04318	0,002504	0,2286	0,04318	0,002248	0,23495
0,04572	0,002207	0,2286	0,04572	0,001996	0,23495
0,04826	0,001834	0,2286	0,04826	0,001666	0,23495
0,0508	0,001384	0,2286	0,0508	0,00126	0,23495
0,05334	0,000861	0,2286	0,05334	0,000772	0,23495
0,055814	0,000157	0,2286	0,055644	0,000142	0,23495
0,055814	0,000157	0,2286	0,055644	0,000142	0,23495
0,05334	0,000119	0,2286	0,05334	0,000114	0,23495
0,0508	0,000229	0,2286	0,0508	0,000221	0,23495
0,04826	0,00032	0,2286	0,04826	0,000305	0,23495
0,04572	0,000389	0,2286	0,04572	0,000358	0,23495
0,04318	0,000437	0,2286	0,04318	0,000386	0,23495
0,04064	0,000462	0,2286	0,04064	0,000389	0,23495
0,0381	0,000462	0,2286	0,0381	0,000363	0,23495
0,03556	0,000439	0,2286	0,03556	0,000312	0,23495
0,03302	0,000391	0,2286	0,03302	0,000229	0,23495
0,03048	0,000318	0,2286	0,03048	0,000137	0,23495
0,02794	0,000244	0,2286	0,02794	6,1E-05	0,23495
0,0254	0,00018	0,2286	0,0254	-2,5E-06	0,23495
0,02286	0,00013	0,2286	0,02286	-5,3E-05	0,23495
0,02032	8,64E-05	0,2286	0,02032	-9,1E-05	0,23495
0,01778	5,33E-05	0,2286	0,01778	-0,00011	0,23495
0,01524	2,79E-05	0,2286	0,01524	-0,00013	0,23495
0,0127	1,02E-05	0,2286	0,0127	-0,00013	0,23495
0,01016	-2,5E-06	0,2286	0,01016	-0,00012	0,23495
0,00762	-1E-05	0,2286	0,00762	-0,0001	0,23495
0,00508	-1,3E-05	0,2286	0,00508	-7,6E-05	0,23495
0,00254	-7,6E-06	0,2286	0,00254	-4,1E-05	0,23495
0	0,000165	0,2286	0	0,000155	0,23495

Blade 11 Coordinates			Blade 12 Coordinates		
x	y	z	x	y	z
0	0,00014	0,244094	0	0,000132	0,252298
0,00254	0,000424	0,244094	0,00254	0,000272	0,252298
0,00508	0,000569	0,244094	0,00508	0,000274	0,252298
0,00762	0,000704	0,244094	0,00762	0,000272	0,252298
0,01016	0,000828	0,244094	0,01016	0,000264	0,252298
0,0127	0,000945	0,244094	0,0127	0,000254	0,252298
0,01524	0,001052	0,244094	0,01524	0,000244	0,252298
0,01778	0,001151	0,244094	0,01778	0,000236	0,252298
0,02032	0,001242	0,244094	0,02032	0,000234	0,252298
0,02286	0,001328	0,244094	0,02286	0,000236	0,252298
0,0254	0,00141	0,244094	0,0254	0,000249	0,252298
0,02794	0,001486	0,244094	0,02794	0,000284	0,252298
0,03048	0,001562	0,244094	0,03048	0,000358	0,252298
0,03302	0,001636	0,244094	0,03302	0,000445	0,252298
0,03556	0,001722	0,244094	0,03556	0,000526	0,252298
0,0381	0,001788	0,244094	0,0381	0,000592	0,252298
0,04064	0,001791	0,244094	0,04064	0,000655	0,252298
0,04318	0,001709	0,244094	0,04318	0,000699	0,252298
0,04572	0,001547	0,244094	0,04572	0,000688	0,252298
0,04826	0,001311	0,244094	0,04826	0,00061	0,252298
0,0508	0,000996	0,244094	0,0508	0,000488	0,252298
0,05334	0,000605	0,244094	0,05334	0,00034	0,252298
0,055474	0,000119	0,244094	0,05588	0,000152	0,252298
0,055474	0,000119	0,244094	0,055931	9,14E-05	0,252298
0,05334	4,32E-05	0,244094	0,055931	9,14E-05	0,252298
0,0508	8,13E-05	0,244094	0,05588	1,02E-05	0,252298
0,04826	0,000109	0,244094	0,05334	-0,00017	0,252298
0,04572	0,000117	0,244094	0,0508	-0,00031	0,252298
0,04318	7,62E-05	0,244094	0,04826	-0,00042	0,252298
0,04064	1,52E-05	0,244094	0,04572	-0,00053	0,252298
0,0381	7,62E-06	0,244094	0,04318	-0,00062	0,252298
0,03556	-0,00019	0,244094	0,04064	-0,00073	0,252298
0,03302	-0,00019	0,244094	0,0381	-0,00085	0,252298
0,03048	-0,00024	0,244094	0,03556	-0,00091	0,252298
0,02794	-0,00031	0,244094	0,03302	-0,00096	0,252298
0,0254	-0,00036	0,244094	0,03048	-0,00102	0,252298
0,02286	-0,00036	0,244094	0,02794	-0,00106	0,252298
0,02032	-0,00036	0,244094	0,0254	-0,00106	0,252298
0,01778	-0,00036	0,244094	0,02286	-0,00103	0,252298
0,01524	-0,00034	0,244094	0,02032	-0,00097	0,252298
0,0127	-0,0003	0,244094	0,01778	-0,0009	0,252298
0,01016	-0,00026	0,244094	0,01524	-0,00081	0,252298
0,00762	-0,00021	0,244094	0,0127	-0,0007	0,252298
0,00508	-0,00015	0,244094	0,01016	-0,00058	0,252298
0,00254	-7,6E-05	0,244094	0,00762	-0,00045	0,252298
0	0,00014	0,244094	0,00508	-0,0003	0,252298
			0,00254	0,000152	0,252298
			0	0,000132	0,252298

Εθνικό Μετσόβιο Πολυτεχνείο
Σχολή Μηχανολόγων Μηχανικών
Τομέας Ρευστών
Μονάδα Παράλληλης Υπολογιστικής Ρευστοδυναμικής & Βελτιστοποίησης

Διαμόρφωση των Κελυφών της Περιστρεφόμενης Πτερύγωσης NASA Rotor 37, με χρήση του λογισμικού PUMA

Διπλωματική Εργασία

Κοτσαρίνης Κωνσταντίνος

Επιβλέπων: Κυριάκος Χ. Γιαννάκογλου, Καθηγητής ΕΜΠ

Βιομηχανικός Επιβλέπων: Αναστάσιος Κοβάνης, Αεροδυναμιστής, Rolls-Royce plc.

Αθήνα, 2021

Εκτενής Περίληψη στα Ελληνικά

Εισαγωγή

Σε αυτήν τη διπλωματική εργασία μελετήθηκε η ροή στη γεωμετρία του δρομέα 37 (NASA Rotor 37) αλλά και η επίδραση που έχει στην επίδοσή της (συντελεστή απόδοσης, λόγο πίεσης) και στη λειτουργικότητά της (περιθώριο αποκόλλησης, περιθώριο στραγγαλισμού) η δημιουργία αυλακώσεων στα κελύφη ποδός (hub) και κεφαλής (casing). Ο δρομέας 37 αποτελεί μια γεωμετρία με χαμηλό λόγο επιμήκους της πρώτης βαθμίδας ενός οκταβάθμιου συμπιεστή με λόγο πίεσης 20:1. Έχει χρησιμοποιηθεί ευρέως για πολλές αξιολογήσεις κωδίκων υπολογιστικής ρευστοδυναμικής (CFD), καθώς υπάρχουν πολλά διαθέσιμα πειραματικά δεδομένα για τη βαθμίδα αυτή μεμονωμένη. Για την πτερύγωση αυτή, πραγματοποιήθηκε μια παραμετρική διερεύνηση της επίπτωσης της τοποθέτησης αυλακώσεων κατά μήκος του περάσματος της πτερύγωσης. Για την υπολογιστική προσομοίωση της ροής γύρω από τη γεωμετρία αναφοράς της πτερύγωσης αλλά και των αυλακώσεων χρησιμοποιήθηκε ο κώδικας PUMA (Parallel Unstructured Multi-row Adjoint) ο οποίος αναπτύχθηκε στο εργαστήριο Στροβιλομηχανών του ΕΜΠ, αφού πρώτα είχε πραγματοποιηθεί σύγκριση και επαλήθευση των αποτελεσμάτων του επιλύτη, ενώ για την πλεγματοποίηση το λογισμικό PADRAM (Parametric Design and Rapid Meshing).

Μέρος αυτής της διπλωματικής εργασίας πραγματοποιήθηκε στις εγκαταστάσεις της Rolls-Royce plc. στο Derby του Ηνωμένου Βασιλείου.

Παραμετροποίηση και πλεγματοποίηση της πτερύγωσης και σχεδιασμός των αυλακώσεων

Για τη δημιουργία της αρχικής γεωμετρίας αναφοράς του δρομέα 37 χρησιμοποιήθηκαν οι συντεταγμένες που παρέχονται στο NASA Technical Paper 1337. Στην συνέχεια αυτές εισήχθησαν στο λογισμικό PADRAM (Parametric Deisgn and Rapid Meshing), το οποίο έχει αναπτυχθεί από την Rolls-Royce plc, για την γένεση του πλέγματος. Στο Σχήμα 1β′ φαίνοται οι διδιάστατες αεροτομές της πτερύγωσης και στο Σχήμα 1α′ φαίνονται κάποια χαρακτηριστικά του πλέγματος της γεωμετρίας αναφοράς του ρότορα 37. Συγκεκριμένα στο πλέγμα, το οποίο χρησιμοποιήθηκε για όλες τις προσομοιώσεις υπολογιστικής ρευστοδυναμικής, χρησιμοποιήθηκαν 24 στρώματα πλεγματοποίησης τύπου O (O-mesh layers), ενώ οι γωνιακοί κόμβοι στην ακμή πρόσπτωσης και εκφυγής τοποθετήθηκαν κατάλληλα με στόχο η στρεβλότητα του πλέγματος να παραμείνει σε επιθυμητά επίπεδα. Για την περιοχή του περάσματος μεταξύ δύο διαδοχικών πτερυγίων χρησιμοποιήθηκαν 80 κόμβοι, ενώ στην ακτινική διεύθυνση τοποθετήθηκαν 120 κόμβοι και το διάκενο μεταξύ του ελεύθερου ακροπτερυγίου και του κελύφους κεφαλής (casing) τέθηκε ίσο με 0.4 mm, ίσο με το δοθέν κατά τις πειραματικές μετρήσεις στη βιβλιογραφία. Έτσι δημιουργήθηκε ένα πλέγμα με ύψος πρώτου κελιού ίσο με $1*10^{-6}mm$ και $y+$ μικρότερο από 1 σε όλη την επιφάνεια του πτερυγίου, αφαιρώντας έτσι την ανάγκη για συναρτήσεις τοίχου.

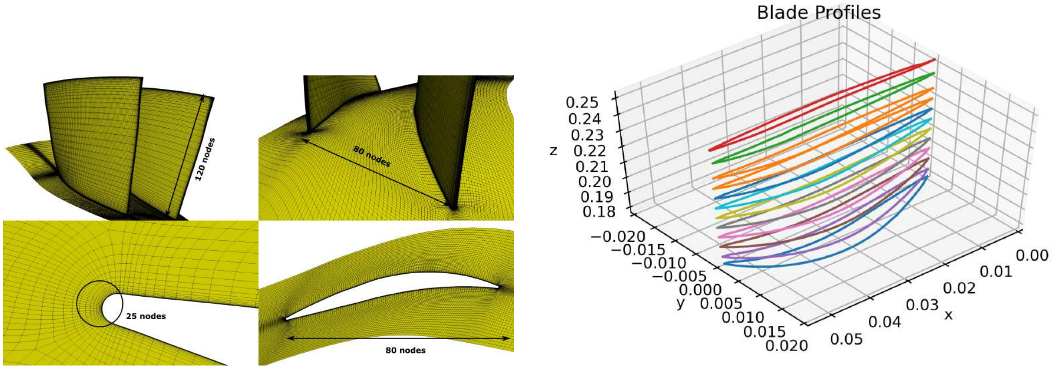

(α′) *Λεπτομέρειες του πλέγματος του δρομέα 37.*

(β′) *Τομές της πτερύγωσης καθ'ύψος.*

Σχήμα 1: *Παραμετροποίηση και πλέγμα της πτερύγωσης.*

Στόχος της διπλωματικής εργασίας είναι η διερεύνηση της επίδρασης αξονοσυμμετρικών αυλακώσεων πάνω στις επιφάνειες του hub και του casing που περιβάλλει τον δρομέα. Πιο συγκεκριμένα δημιουργήθηκαν 5 πανομοιότυπες γεωμετρίες αυλακώσεων για την κάθε περίπτωση, με μόνη διαφορά την αξονική τοποθέτηση του μέγιστου βάθους της αυλάκωσης, όπως φαίνεται στο Σχήμα 3. Για τη δημιουργία των αυλακώσεων χρησιμοποιήθηκαν οι καμπύλες B-Splines που φαίνονται στο Σχήμα 2, οι οποίες για την δημιουργία των αυλακώσεων του δρομέα ¨αφαιρέθηκαν’ ακτινικά από τη γενέτειρα που εκ περιστροφής της προκύπτει η τριδιάστατη επιφάνεια του κελύφους ποδός (hub), ενώ για την περίπτωση του κελύφους της κεφαλής (casing) προστέθηκαν στη γενέτειρά της. Η διερεύνηση εστίασε στην επίδραση της αξονικής θέσης του μέγιστου βάθους των αυλακώσεων, επομένως ολες οι αυλακώσεις επιλέχθηκαν να έχουν μέγιστο βάθος ίσο με 5% του εκπετάσματος του πτερυγίου, με στόχο να πειροριστούν σημαντικές επιταχύνσεις της ροής που θα μπορούσαν να οδηγήσουν σε τοπικές αποκολλήσεις. Η ονοματολογία που ακολουθείται σε αυτή την εργασία αφορά την αξονική θέση του μέγιστου βάθους της αυλάκωσης, η οποία δίνεται ως ποσοστό της χορδής του πτερυγίου - στο 0% το μέγιστο βρίσκεται στην ακμή πρόσπτωσης ενώ στο 100% στην ακμή εκφυγής του πτερυγίου.

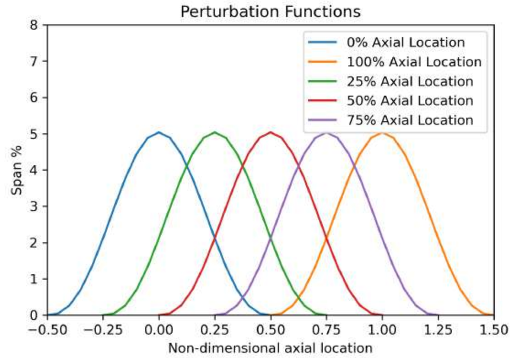

Σχήμα 2: *Συναρτήσεις επίδρασης στη μορφή της γεωμετρίας του δρομέα 37.*

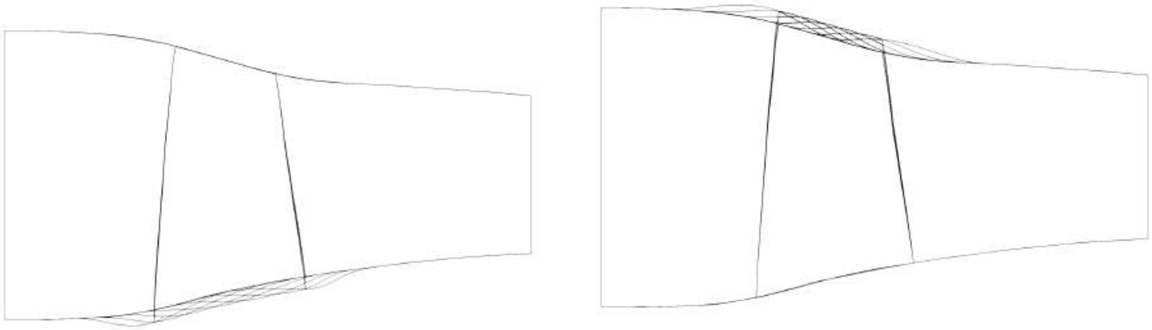

(α′) *Περιβάλλουσα των νέων γεωμετριών του κελύφους ποδός (hub).*

(β′) *Περιβάλλουσα των νέων γεωμετριών του κελύφους της κεφαλής (casing).*

Σχήμα 3: *Περιβάλουσες των διαμορφωμένων κελυφών ποδός (hub) και κεφαλής (casing).*

Πιστοποίηση των αποτελεσμάτων του κώδικα PUMA

Πριν πραγματοποιηθεί η διερεύνηση της επίδρασης των αυλακώσεων πραγματοποιήθηκε σύγκριση και πιστοποίηση των αποτελεσμάτων του επιλύτη PUMA, κάνοντας χρήση του μοντέλου τύρβης Spalart-Allmaras με ολοκλήρωση μέχρι τον τοίχο. Στο Σχήμα 4 παρουσιάζονται τα αποτελέσματα του κώδικα PUMA ταυτόχρονα με πειραματικά αποτελέσματα διαθέσιμα στη βιβλιογραφία αλλά και αποτελέσματα του κώδικα H3D που αναπτύχθηκε στην NASA. Όπως φαίνεται και στα διαγράμματα των χαρακτηριστικών του λόγου πίεσης, θερμοκρασίας αλλά και του συντελεστή απόδοσης ο κώδικας PUMA υπολογίζει με ικανοποιητική ακρίβεια την επίδοση του δρομέα 37 στις διάφορες συνθήκες παροχής. Για την ακρίβεια η παροχή μάζας κατα τον στραγγαλισμό του συμπιεστή υπολογίστηκε ίση με $20.94kg/s$ ενώ η πειραματική μέτρηση ισούται με $20.93kg/s$. Στις συνθήκες στραγγαλισμού η παροχή μάζας που υπολογίστηκε έχει αμελητέα διαφορά με τα πειραματικά αποτελέσματα, ο λόγος πίεσης είχε διαφορά 7.5%, ο συντελεστής απόδοσης είχε διαφορά 3.5%, ενώ ο λόγος θερμοκρασίας είχε διαφορά 3.5%. Αντίστοιχα, κοντά στις συνθήκες αποκόλλησης οι διαφορές των ποσοτήτων που υπολογίστηκαν και των πειραματικών ήταν 2% στην παροχή μάζας και 1% στον συντελεστή απόδοσης, τον λόγο πίεσης και τον λόγο θερμοκρασίας.

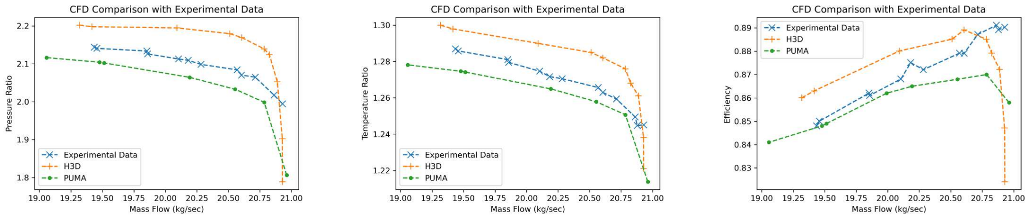

(α′) *Χαρακτηριστική του λόγου πίεσης στις ονομαστικές στροφές.*

(β′) *Χαρακτηριστική του λόγου θερμοκρασίας στις ονομαστικές στροφές.*

(γ′) *Χαρακτηριστική του συντελεστή απόδοσης στις ονομαστικές στροφές.*

Σχήμα 4: *Σύγκριση πειραματικών μετρήσεων με τα υπολογιστικά αποτελέσματα του PUMA.*

Αυλακώσεις στα κελύφη ποδός του NASA Rotor 37

Στη συνέχεια παρουσιάζεται η ανάλυση των αποτελεσμάτων που προέκυψαν για την γεωμετρία του δρομέα 37 με αυλακώσεις στην επιφάνεια του κελύφους ποδός (hub). Στο Σχήμα 5 παρουσιάζονται οι χαρακτηριστικές όλων των περιπτώσεων υπο διερεύνηση σε αντιπαράθεση με την γεωμετρία αναφοράς. Αρχικά, από αυτήν τη διερεύνηση φάνηκε ότι κατά τη μετακίνηση του μέγιστου βάθους των αυλακώσεων προς την ακμή εκφυγής του πτερυγίου προκύπτει μείωση της επίδοσης του ρότορα, τόσο στον λόγο πίεσης όσο και στον συντελεστή απόδοσης. Αντιθέτως η τοποθέτηση του μέγιστου βάθους κοντά στην θέση που βρίσκεται το κύμα κρούσης μεταξύ του περάσματος στο 25% - 50% της χορδής προκάλεσε αύξηση του λόγου πίεσης και του συντελεστή απόδοσης. Από την άλλη πλευρά κατα τη μετακίνηση του μεγίστου προς την ακμή εκφυγής του πτερυγίου προκάλεσε αύξηση του περιθωρίου αποκόλλησης και στραγγαλισμού, ενώ η τοποθέτηση του κοντά στο κύμα κρούσης στο 25% της χορδής δημιούργησε πτώση στο περιθώριο αποκόλλησης.

Στα Σχήματα 9 και 10 παρουσιάζονται οι κατανομές πίεσης στην πλευρά υποπίεσης του ρότορα καθώς και οι ισοεπιφάνειες μηδενικής αξονικής ταχύτητας. Παρατηρείται ότι οι αυλακώσεις με μέγιστο βάθος κόντα στο κύμα κρούσης αυξάνουν τη φόρτιση του πτερυγίου κοντά στον πόδα του και ταυτόχρονα μειώνουν την αποκόλληση στην ακμή εκφυγής, γεγονός που συνάδει με την αύξηση της επίδοσης, ενώ οι αυλακώσεις κοντά στην ακμή εκφυγής μειώνουν τη φόρτιση της πτερύγωσης γεγονός που συνάδει με τα προηγούμενα συμπεράσματα.

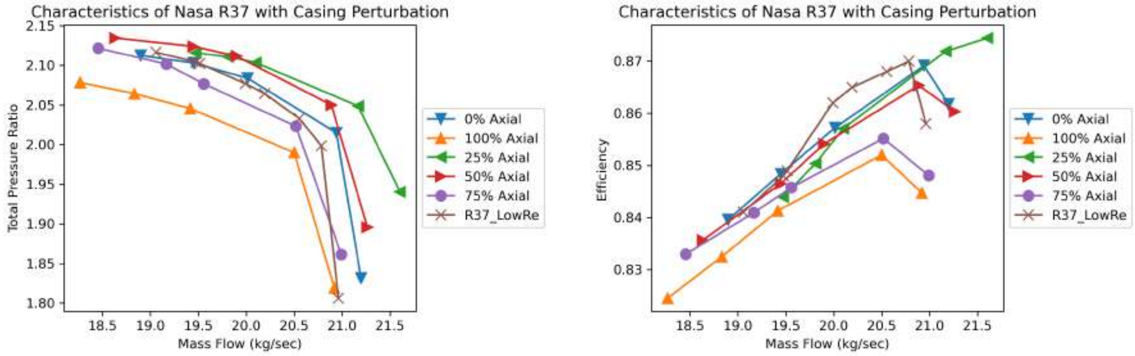

(α′) *Λόγος πίεσης* (β′) *Συντελεστής απόδοσης*

Σχήμα 5: *Σύγκριση χαρακτηριστικών της επίδοσης της γεωμετρίας αναφοράς και των νέων γεωμετριών του κελύφους ποδός της πτερύγωσης στις ονομαστικές στροφές.*

Αυλακώσεις στα κελύφη κεφαλής του NASA Rotor 37

Στη συνέχεια παρουσιάζεται η ανάλυση των αποτελεσμάτων που προέκυψαν για την γεωμετρία του δρομέα 37 με αυλακώσεις στην επιφάνεια του κελύφους κεφαλής (casing). Στο Σχήμα 8 παρουσιάζονται οι χαρακτηριστικές όλων των περιπτώσεων υπο διερεύνηση σε αντιπαράθεση με την γεωμετρία αναφοράς του δρομέα 37. Αρχικά από αυτή τη διερεύνηση φάνηκε ότι κατά την μετακίνηση του μέγιστου βάθους των αυλακώσεων προς την ακμή πρόσπτωσης του πτερυγίου προκύπτει μείωση της επίδοσης του ρότορα, τόσο στον λόγο πίεσης όσο και στον συντελεστή απόδοσης. Από την άλλη πλευρά κατα τη μετακίνηση του μεγίστου προς την ακμή εκφυγής του πτερυγίου προκάλεσε αύξηση του περιθωρίου περιστροφικής αποκόλλησης και στραγγαλισμού.

Στα Σχήματα 9 και 10 παρουσιάζονται οι κατανομές πίεσης στην πλευρά υποπίεσης του ρότορα καθώς και οι ισοεπιφάνειες μηδενικής αξονικής ταχύτητας. Παρατηρείται ότι οι αυλακώσεις με μέγιστο βάθος κόντα στην ακμή πρόσπτωσης αυξάνουν την φόρτιση του πτερυγίου κοντά στην περιοχή του ακροπτερυγίου και, ταυτόχρονα, αυξάνουν τη

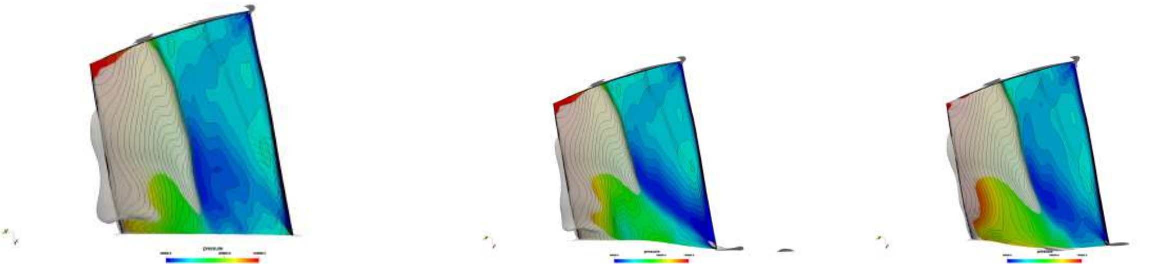

(α΄) *Γεωμετρία Αναφοράς* (β΄) *0% Axial Positioning* (γ΄) *25% Axial Positioning*

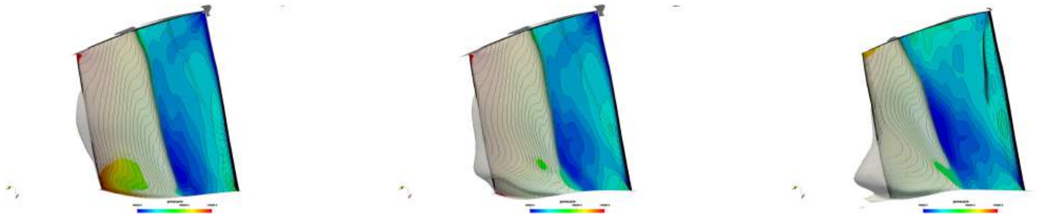

(δ΄) *50% Axial Positioning* (ε΄) *75% Axial Positioning* (ϛ΄) *100% Axial Positioning*

Σχήμα 6: *Σύγκριση της κατανομής πίεσης στην επιφάνεια υποπίεσης της πτερύγωσης καθώς και των ισοεπιφανειών μηδενικής αξονικής ταχύτητας μεταξύ της γεωμετρίας αναφοράς καθώς και των νέων γεωμετριών του κελύφους ποδός της πτερύγωσης κοντά στις συνθήκες μέγιστου συντελεστή απόδοσης.*

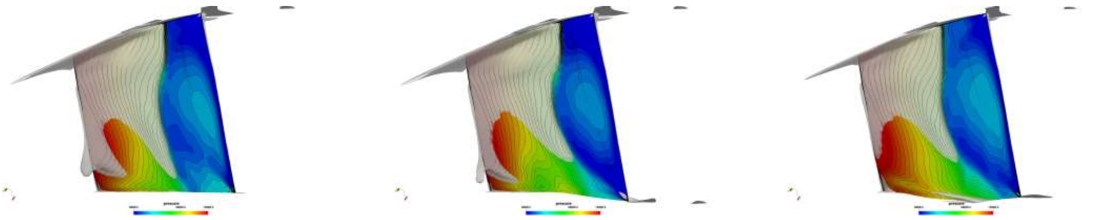

(α΄) *Γεωμετρία Αναφοράς* (β΄) *0% Axial Positioning* (γ΄) *25% Axial Positioning*

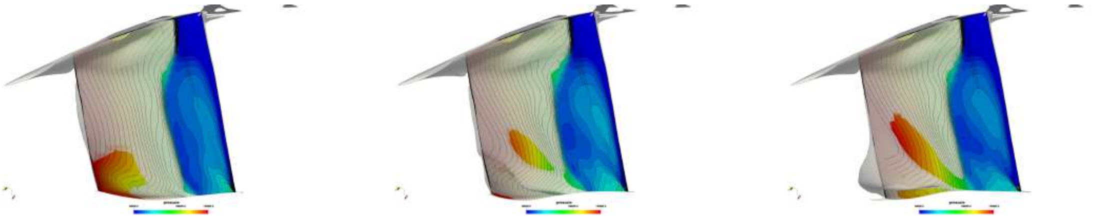

(δ΄) *50% Axial Positioning* (ε΄) *75% Axial Positioning* (ϛ΄) *100% Axial Positioning*

Σχήμα 7: *Σύγκριση της κατανομής πίεσης στην επιφάνεια υποπίεσης της πτερύγωσης καθώς και των ισοεπιφανειών μηδενικής αξονικής ταχύτητας μεταξύ της γεωμετρίας αναφοράς καθώς και των νέων γεωμετριών του κελύφους ποδός της πτερύγωσης κοντά στις συνθήκες περιστροφικής αποκόλλησης.*

φυσαλίδα μηδενικής αξονικής ταχύτητας κοντά σε αυτήν την περιοχή σε συνθήκες υψηλής παροχής, ενώ οι αυλακώσεις κοντά στην ακμή εκφυγής αυξάνουν τη φόρτιση της πτερύγωσης στην περιοχή του ακροπτερυγίου σε συνθήκες χαμηλής παροχής γεγονός που συνάδει με τα προηγούμενα συμπεράσματα.

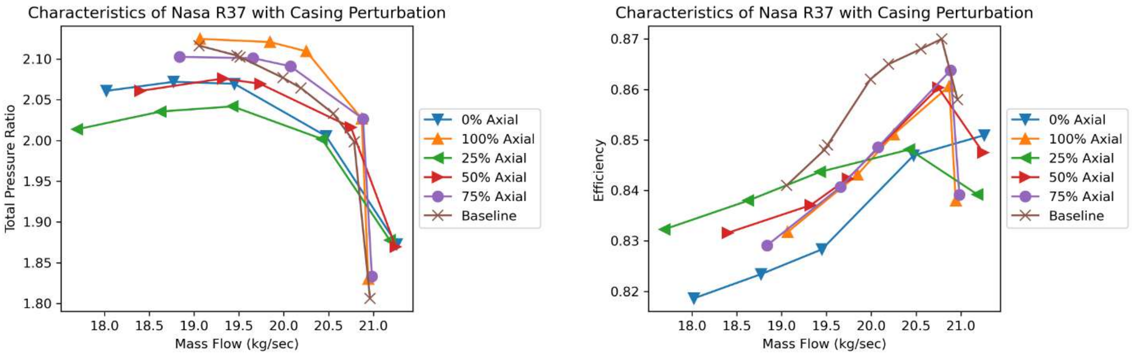

(α΄) *Λόγος πίεσης* (β΄) *Συντελεστής απόδοσης*

Σχήμα 8: *Σύγκριση χαρακτηριστικών της επίδοσης της γεωμετρίας αναφοράς και των νέων γεωμετριών του κελύφους κεφαλής της πτερύγωσης.*

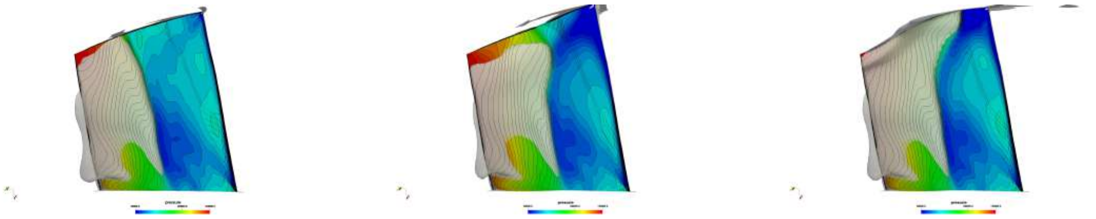

(α΄) *Γεωμετρία Αναφοράς* (β΄) *0% Axial Positioning* (γ΄) *25% Axial Positioning*

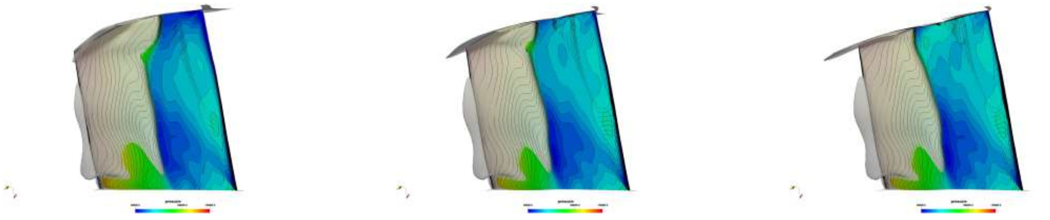

(δ΄) *50% Axial Positioning* (ε΄) *75% Axial Positioning* (ϛ΄) *100% Axial Positioning*

Σχήμα 9: *Σύγκριση της κατανομής πίεσης στην επιφάνεια υποπίεσης της πτερύγωσης καθώς και των ισοεπιφανειών μηδενικής αξονικής ταχύτητας μεταξύ της γεωμετρίας αναφοράς καθώς και των νέων γεωμετριών του κελύφους της κεφαλής της πτερύγωσης κοντά στις συνθήκες μέγιστου συντελεστή απόδοσης.*

Συνδιαστική αυλάκωση στο κέλυφος ποδός και κεφαλής

Στη συνέχεια παρουσιάζεται η ανάλυση των αποτελεσμάτων που προέκυψαν για την γεωμετρία του δρομέα 37 με αυλακώση ταυτόχρονα στην επιφάνεια του κελύφους ποδός

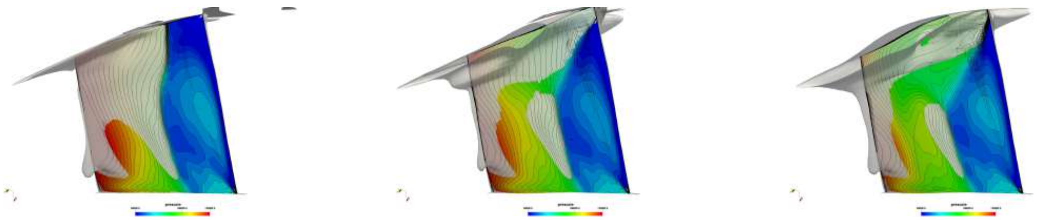

(α′) *Γεωμετρία Αναφοράς* (β′) *0% Axial Positioning* (γ′) *25% Axial Positioning*

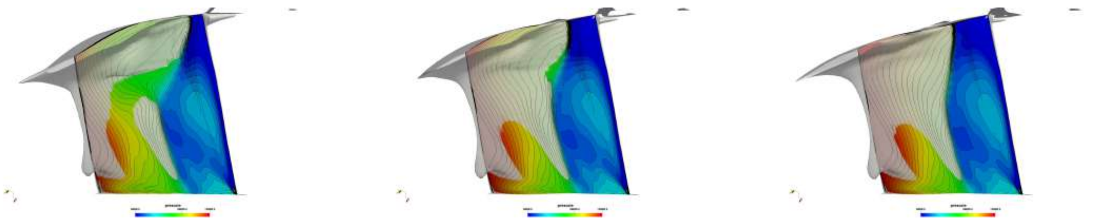

(δ′) *50% Axial Positioning* (ε′) *75% Axial Positioning* (ϛ′) *100% Axial Positioning*

Σχήμα 10: *Σύγκριση της κατανομής πίεσης στην επιφάνεια υποπίεσης της πτερύγωσης καθώς και των ισοεπιφανειών μηδενικής αξονικής ταχύτητας μεταξύ της γεωμετρίας αναφοράς καθώς και των νεών γεωμετριών του κελύφους κεφαλής της πτερύγωσης κοντά στις συνθήκες περιστροφικής αποκόλλησης.*

και του κελύφους κεφαλής. Στο Σχήμα 11 παρουσιάζονται οι χαρακτηριστικές της γεωμετρίας με τον συνδυασμό των αυλακώσεων καθώς και των γεωμετριών με μία μόνο αυλάκωση είτε στο κέλυφος ποδός είτε στο κέλυφος κεφαλής σε αντιπαράθεση με την γεωμετρία αναφοράς. Φαίνεται ότι ο συνδυασμός δύο αυλακώσεων οδήγησε σε αυξημένο λόγο πίεσης αλλά και αυξημένο περιθώριο αποκόλλησης.

Επιπλέον στο Σχήμα 12 παρουσιάζονται συνολικά οι επιδόσεις καθώς και τα περιθώρια λειτουργικότητας όλων των περιπτώσεων που διερευνήθηκαν, το οποίο επιβεβαιώνει τα μέχρι τώρα συμπεράσματα.

Συμπεράσματα

Συνοψίζοντας, στη διπλωματική εργασία έγινε διερεύνηση της επίδρασης της αξονικής θέσης του μέγιστου βάθους αξονοσυμετρικών αυλακώσεων στη γεωμετρία του NASA Rotor 37. Για τη διερεύνηση αυτή δημιουργήθηκε πλέγμα μέσω του λογισμικού PADRAM, ενώ ο υπολογισμός του πεδίου ροής για κάθε αυλάκωση έγινε με τον κώδικα PUMA, αφού πιστοποιήθηκε ότι τα αποτελέσματά του έχουν ικανοποιητική ακρίβεια μετά από σύγκριση με πειραματικά δεδομένα.

Όσον αφορά στην επίδραση των αυλακώσεων πάνω στην επιφάνεια του κελύφους ποδός, παρατηρήθηκε ότι οι αυλακώσεις με μέγιστο βάθος κοντά στο κύμα κρόυσης αυξάνουν τον λόγο πίεσης ή/και τον συντελεστή απόδοσης, ενώ οι αυλακώσεις κοντά στην ακμή εκφυγής αυξάνουν τα περιθώρια αποκόλλησης και στραγγαλισμού. Όσον

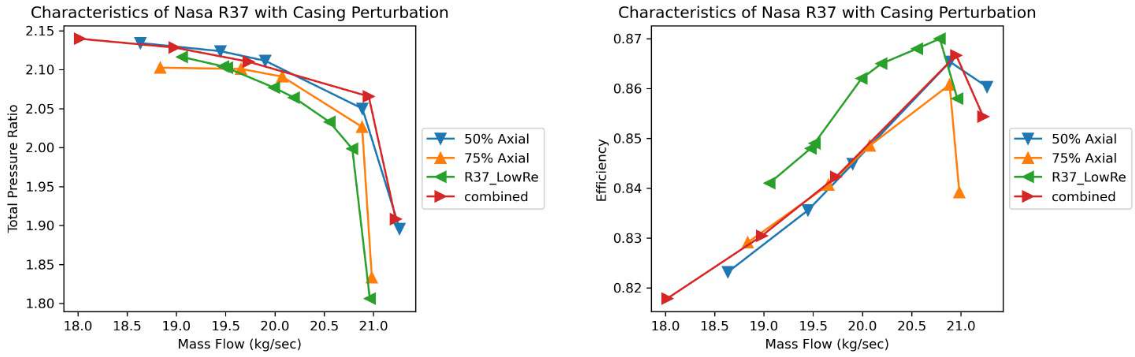

(α′) *Λόγος πίεσης* (β′) *Συντελεστής απόδοσης*

Σχήμα 11: *Σύγκριση χαρακτηριστικών της επίδοσης της γεωμετρίας αναφοράς καθώς και της συνδυαστικής αλλαγής της γεωμετρίας των τοιχωμάτων της πτερύγωσης στις ονομαστικές στροφές.*

αφορά στην επίδραση των αυλακώσεων πάνω στην επιφάνεια του κελύφους κεφαλής, παρατηρήθηκε ότι οι αυλακώσεις με μέγιστο βάθος κοντά στην ακμή εκφυγής αυξάνουν τα περιθώρια αποκόλλησης και στραγγαλισμού. Τέλος, η ταυτόχρονη χρήση αυλακώσεων κοντά στο κύμα κρούσης οδήγησε σε αύξηση του λόγου πίεσης αλλά και του περιθωρίου αποκόλλησης.

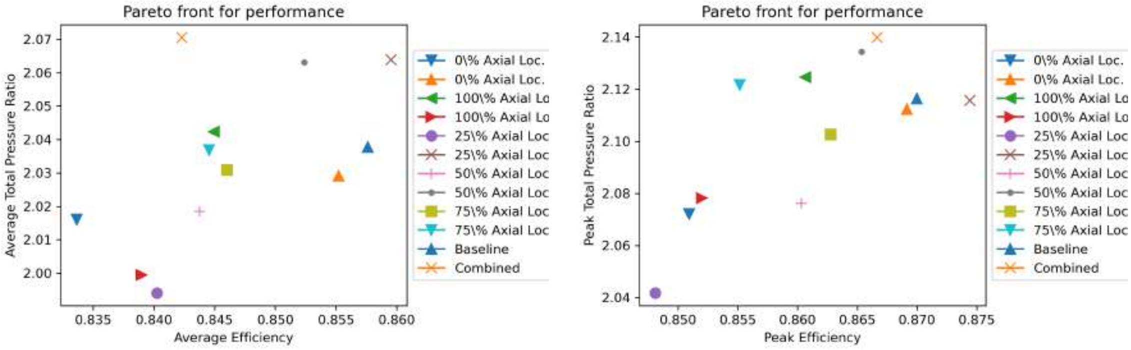

(α′) *Συνδυαστική απεικόνιση του μέσου λόγου πίεσης και συντελεστή απόδοσης.*

(β′) *Συνδυαστική απεικόνιση του μέγιστου λόγου πίεσης και συντελεστή απόδοσης.*

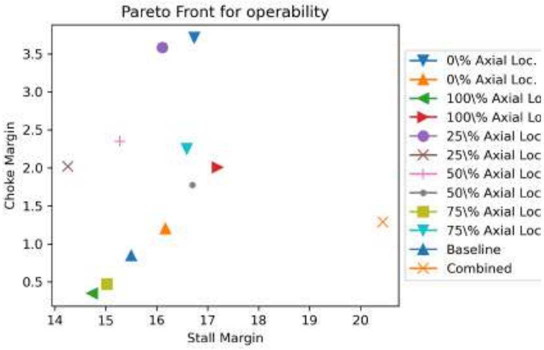

(γ′) *Συνδυαστική απεικόνιση του περιθωρίου αποκόλλησης και στραγγαλισμού.*

Σχήμα 12: *Σύγκριση επιδόσεων και λειτουργικότητας όλων των γεωμετριών που διερευνήθηκαν.*

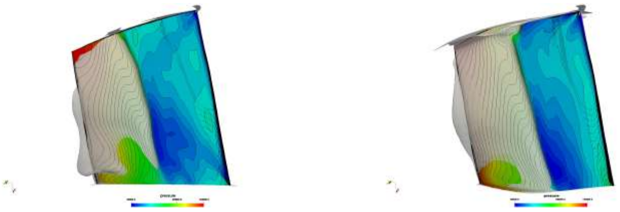

(α′) *Γεωμετρία Αναφοράς* (β′) *Συνδιαστική αλλαγή γεωμετρίας τοιχωμάτων*

(γ′) *Γεωμετρία Αναφοράς* (δ′) *Συνδιαστική αλλαγή γεωμετρίας τοιχωμάτων*

Σχήμα 13: *Σύγκριση της κατανομής πίεσης στην επιφάνεια υποπίεσης της πτερύγωσης καθώς και των ισοεπιφανειών μηδενικής αξονικής ταχύτητας μεταξύ της γεωμετρίας αναφοράς καθώς και της συνδιαστικής αλλαγής της γεωμετρίας των τοιχωμάτων της πτερύγωσης κοντά στις συνθήκες μέγιστου συντελεστή απόδοσης (α),(β) και κοντά σε συνθήκες αποκόλλησης (γ), (δ).*